EXAMINING THE IMPACT OF WILDFIRE SMOKE AEROSOL ON CLOUDS, PRECIPITATIION, AND RADIATIVE FLUXES IN NORTHERN AMERICA AND RUSSIA USING A FULLY COUPLED MESO-SCALE MODEL WRF-CHEM-SMOKE AND SATELLITE DATA

A Dissertation
Presented to
The Academic Faculty

By

Zheng Lu

In Partial Fulfillment
of the Requirements for the Degree
Doctor of Philosophy in the
School of Earth and Atmospheric Sciences

Georgia Institute of Technology
August 2014

EXAMINING THE IMPACT OF WILDFIRE SMOKE AEROSOL ON CLOUDS, PRECIPITATIION, AND RADIATIVE FLUXES IN NORTHERN AMERICA AND RUSSIA USING A FULLY COUPLED MESO-SCALE MODEL WRF-CHEM-SMOKE AND SATELLITE DATA

Approved by:

Dr. Irina N. Sokolik, Advisor
School of Earth and Atmospheric Sciences
Georgia Institute of Technology

Dr. Judith A. Curry
School of Earth and Atmospheric sciences
Georgia Institute of Technology

Dr. Athanasios Nenes
School of Chemical and Biomolecular Engineering and School of Earth and Atmospheric Sciences
Georgia Institute of Technology

Dr. Viatcheslav Tatarskii
School of Earth and Atmospheric Sciences
Georgia Institute of Technology

Dr. Rodney Weber
School of Earth and Atmospheric Sciences
Georgia Institute of Technology

Date Approved: June 24, 2014

“Nature uses only the longest threads to weave her patterns, so each small piece of her fabric reveals the organization of the entire tapestry.”

— Richard P. Feynman

Acknowledgements

First, my deepest gratitude is to my advisor, Dr. Irina Sokolik, for her long-term support, professional guidance, and belief in my abilities. My thanks also go to Dr. Judith Curry, Dr. Athanasios Nenes, Dr. Viatcheslav Tatarskii, and Dr. Rodney Weber for agreeing to be my thesis committee members despite their extremely busy schedules. I would also like to acknowledge all the members and alumni of Dr. Sokolik's group, especially Anton Darmenov, Kremena Darmenova, Xin Xi, Hyung-Jin Choi, Prashant Kumar, Erica Alston, Cindy Young, and Henian Zhang for their assistance and support. Finally, I am grateful to my family, especially my parents and my wife, Jiaxing Liu. Without their love and support, I would not have finished this thesis.

TABLE OF CONTENTS

LIST OF TABLES

Page

LIST OF FIGURES

Page

LIST OF ABBREVIATIONS

AeroCom	Aerosol Comparisons between Observations and Models
AOD	Aerosol Optical Depth
AVHRR	Advanced Very High Resolution Radiometer
BC	Black Carbon
CALIOP	Cloud-Aerosol with Orthogonal Polarization
CALIPSO	Cloud-Aerosol Lidar and Infrared Pathfinder Satellite Observations
CAM	Community Atmosphere Model
CCN	Cloud Condensation Nuclei
DARE	Direct Aerosol Radiative Effect
DOB	Date of Burn
FRP	Fire Radiative Power
GCM	General Circulation Model
GOES	Geostationary Operational Environmental Satellite
IN	Ice Nuclei
IPCC	Intergovernmental Panel on Climate Change
LW	Longwave
MODIS	Moderate Resolution Imaging Spectroradiometer
MISR	Multi-angle Imaging Spectroradiometer
NASA	National Aeronautics and Space Administration
NCEP	National Center for Environment Prediction
OC	Organic Carbon
OM	Organic Matter

PM2.5	Particulate Matter of an aerodynamic diameter < 2.5 μm
RAMS	Regional Atmospheric Modeling System
RH	Relative Humidity
SFC	Surface
SSA	Single Scattering Albedo
SW	Shortwave
TOA	Top of the Atmosphere
TPM	Total Particulate Matter
WRF-Chem	Weather Research Forecasting model coupled with Chemistry

LIST OF SYMBOLS

a	Burned Area
α	Available Biomass Fuel
b_{ext}	Mass extinction Coefficient
β	Combustion Factor
EF	Emission Factor
g	Asymmetry parameter
λ	Wavelength
σ	Standard Deviation of Aerosol Size Distribution
Q_e	Extinction Efficiency
Q_s	Scattering Efficiency
ω_0	Single Scattering Albedo
T_4	Brightness Temperature at 4μm
$SW_{TOA}\uparrow$	Upward Shortwave Radiative Fluxes at TOA
$SW_{SFC}\downarrow$	Downward Shortwave Radiative Fluxes at the Surface
RF_{ari}	Radiative Forcing due to Aerosol-Radiation Interaction
RF_{aci}	Radiative Forcing due to Aerosol-Cloud Interaction

SUMMARY

The boreal forest covers a vast region of 1.2 billion hectares, spanning North America and Russia. Wildfires frequently occur in the boreal forest. Smoke emitted from wildfires can scatter and absorb radiative fluxes, exerting direct aerosol effects on the radiative energy budget. Smoke can also alter the abundance and properties of clouds, which further affects the radiative energy budget and precipitation processes. In this thesis, we develop a fully coupled meso-scale WRF-Chem-SMOKE model, and investigate to what extent and how smoke released from boreal wildfires affects local cloud properties, precipitation, and radiative fluxes using WRF-Chem-SMOKE in conjunction with remote sensing data.

In WRF-Chem-SMOKE, smoke aerosol is treated as an internal mixture of OM, BC, and residual particulate matter in the MOSAIC aerosol scheme. Smoke particles can function as SW absorbers, CCN, and IN; therefore, smoke-radiation and smoke-cloud interactions can be explicitly simulated in the model. We add two major new capabilities in WRF-Chem-SMOKE. Firstly, we construct three original smoke emission models/datasets, which are based on the burned area (BA) technique with the WF_ABBA or the MCD45A1 products, or the fire radiative power (PRF) technique with the MCD14ML product. In order to maximize the benefits of each product, we also develop an algorithm that integrates the three original smoke emissions. Secondly, we improve the representation of smoke-cloud interactions in the model by 1) incorporating the smoke-property-dependent ice nucleation scheme, the Phillips scheme, into the Morrison two-moment scheme and 2) replacing the fixed riming collection efficiency with the size-dependent riming collection efficiency.

By studying the 2007 central and eastern Canada wildfire case, we find that estimated smoke emissions based on the WF_ABBA product need to be multiplied by a factor of ten to match the MODIS AOD. We compare the spatiotemporal distributions of three original smoke emission datasets in several major fire clusters. The manner in which the three datasets differ from each other varies from one fire cluster to another, and the manner is directly related to the fire characteristics, such as burning phase and fire spreading rate. The smoke AOD fields modeled by the different cases with different datasets incorporated are compared against the MODIS AOD observations. The results show that the differences in smoke emission datasets, even in one fire cluster, could lead to significant discrepancies in modeled AODs. The statistical analyses show that no modeling case always yields the best performance through the simulation period; however, the modeling case with the integrated smoke emission dataset produces the highest three-day total Taylor skill scores.

Modeling experiments with one, five and ten times the original WF_ABBA smoke emissions reveal that low smoke load favors the collision-coalescence process at a certain stage, leading to either positive or negative changes in cloud water path (CWP) relative to smoke-free conditions. For high smoke emissions, changes in CWP are positive, as large as 0.5 kg/m^2. A domain-integrated increase in CWP is proportional to smoke loading. While domain-integrated changes in RWP are negative, those in SWP go from negative to positive under a high smoke load. Higher smoke loadings suppress precipitation initially, because of smoke-induced reduction of the collision-coalescence and riming processes, but ultimately cause an invigoration of precipitation. We find that precipitation is highly sensitive to 3D smoke fields.

The 2002 central Siberia wildfire season can be characterized by two fire regimes (FR1 and FR2). During FR1, a small amount of smoke was emitted and swirled in a relatively strong frontal system (FS1). During FR2, a large amount of smoke was firstly emitted because of a blocking high pressure system, then depleted by a relatively weak frontal system (FS2). We find that high CDNC but low IN number concentrations are activated from smoke in the upper portion of FS1. Modeled RWC and SWC are strongly reduced by about 25~50% in the region with high CDNC. The cloud cells acquire a longer lifetime and form more SWC further downwind. In contrast, both CDNC and IN number concentrations are high in FS2. RWC is reduced because of high CDNC, however, high IN number concentrations increase SWC by 4%. Due to the competing effects of CDNC and IN, the effect of smoke on cloud lifetime is very small. Consequently, the smoke-induced changes in cloudiness exhibit a dipole feature.

After the smoke particles are nearly consumed, the large-scale dynamics of FS1 are altered. The onset of precipitation is delayed by one day and the area-averaged daily precipitation is significantly affected (-2.04 mm/day on 11 August and +1.32 mm/day on 12 August). In FS2, however, the large-scale dynamics are barely affected. Therefore, the onset of precipitation is not delayed but the spatial distribution of precipitation is significantly affected (a dipole feature). The area-averaged daily precipitation is slightly reduced by smoke (-0.42 mm/day on 24 August).

By comparing $SW_{TOA}\uparrow$ (upward shortwave flux at TOA) modeled by the SMOKE and smoke-free cases against the NASA SRB dataset, we find that the inclusion of the radiative and microphysical properties of smoke in meso-scale modeling can improve the simulation of radiation fields. During FR1, the direct aerosol effect of smoke causes a

slight cooling effect at TOA (~ -1 W/m^2, instantaneous radiative flux at 0600UTC). The cloud water at the forward edge of the lower portion of FS1 is quickly depleted due to relatively high IN number concentrations, leading to a considerable warming effect at TOA. The area-averaged total aerosol radiative effect remains positive (~3 W/m^2) during FR1. During the early stage of FR2, a large amount of smoke causes a long-lasting cooling effect at TOA (~ -7 W/m^2). In the clouds around the edge of the high pressure, CDNC change from low to high. Low CDNC promote the rain formation and cause the cloud layers to become optically thinner, while higher CDNC lead to smaller cloud droplets and higher cloud albedo. Therefore, the indirect aerosol effect of smoke goes from a warming effect to a cooling effect, and the area-averaged total aerosol radiative effect goes from near zero to large negative values (~ -10 W/m^2).

CHAPTER 1

INTRODUCTION

1.1 Background and Motivation

Fire has been used by human to manipulate the environment for nearly million years; however, only during the last few decades have global vegetation fires been systematically studied and monitored [*Bowman, et al*., 2009]. Vegetation fire represents an important source of trace gases and aerosol particles [*Langmann et al*., 2009]. During the burning process, more than 95% of fire emission is released as trace gases, including important long-lasting green house gases (GHGs) such as CO_2 and CH_4 [*Andreae and Merlet*, 2001; *Langenfelds et al.*, 2002]. Less than 5% of fire emission is released as smoke aerosols, which consist mainly of organic matter (OM) and black carbon (BC) [*Reid et al*., 2005]. The impacts of smoke on climate and meteorology are manifold. Smoke can scatter and absorb radiative fluxes, exerting direct aerosol effects on the radiative energy budget [*Hobbs et al*., 1997; *Randerson et al*., 2006]. Moreover, smoke can alter the abundance and properties of clouds, which further affects the radiative energy budget (indirect aerosol effects) and the precipitation processes [*Rosenfeld*, 1999; *Andreae et al*., 2004; *Koren et al.*, 2004; *Tosca et al*., 2010]. Compared to the relatively well-studied green house effect, the effects of aerosols and clouds contribute great uncertainty in estimating the changes in the regional and global climate and environment [*IPCC AR5*, 2013; *Bond et al*., 2013].

There is a surging interest within the scientific community in examining smoke-radiation-cloud-precipitation interactions in the boreal region. The boreal forest, which

lies roughly between 18°C~13°C mean July isothermal lines or between 45°N~70°N, is a circumpolar vegetation zone that covers a vast area of 1.33 billion hectares, spanning North America (about 1/3 of total area) and North Eurasia (about 2/3 of total area, mainly in Russia) [*Soja et al*., 2007]. A large amount of carbon is stored in needleleaf (e.g. larch, pine, and spruce) and deciduous broadleaf trees (e.g. birch and aspen), understory, and peat/organic soil, which totally constitutes the largest reservoir of terrestrial carbon [*Alexeyev and Birdsey*, 1998]. On average, about 3~5.1 Tg and 0.6~0.9 Tg of smoke aerosols are emitted in Russia and North America every year, respectively [*Reid et al*., 2009; *van der Werf et al*., 2010]. There is evidence that the rapid temperature increase in the boreal region predicted by the climate models could lead to increases in the occurrence of wildfires [*Stock et al*., 1998; *Kloster et al*., 2010]. Meanwhile, both remote sensing observations and modeling studies suggest that the fuel availability in the boreal region increases as this region becomes "warmer and greener" [*Xu et al*., 2013; *Lucht et al*., 2002]. Therefore, smoke emissions in the boreal region will potentially increase in the future.

Despite the growing importance associated with smoke emissions in the boreal region, the impacts of smoke on radiation, clouds, and precipitation in high latitudes are relatively less studied, compared to many past studies that focus on tropical regions, including Indonesia [*Langmann*, 2007; *Graf et al*., 2009; *Tosca et al*., 2010; *Reid et al*., 2013] and the Amazonian region [*Koren et al*., 2004; *Andreae et al*., 2004; *Wu et al*., 2011; *Ten Hoeve et al*., 2012]. In the tropic, the dominant cloud type during the dry season (fire season) is liquid-phase scattered cumulus, which is formed under stable atmospheric condition. In the boreal region, fires are mainly caused by natural factors,

such as dry lightning associated with frontal systems [*Nash and Johnson*, 1996] or persistent high pressure systems that dry the fuels [*Flannigan and Harrington*, 1988]. Consequently, in the boreal region, smoke is able to interact with various cloud types under different meteorological conditions, such as convective mixed-phase clouds associated with frontal systems or stratiform clouds formed around the edge of high pressure systems. The clouds within a frontal system are particularly important, since they usually bring a large amount of precipitation in this region [*Hobbs*, 1978]. The impacts of smoke on radiation, clouds, and precipitation may very likely vary under different fire/cloud regimes in the boreal regions; therefore, the impacts of smoke should be examined in a dynamical/meteorological context [*Levin and Cotton*, 2008].

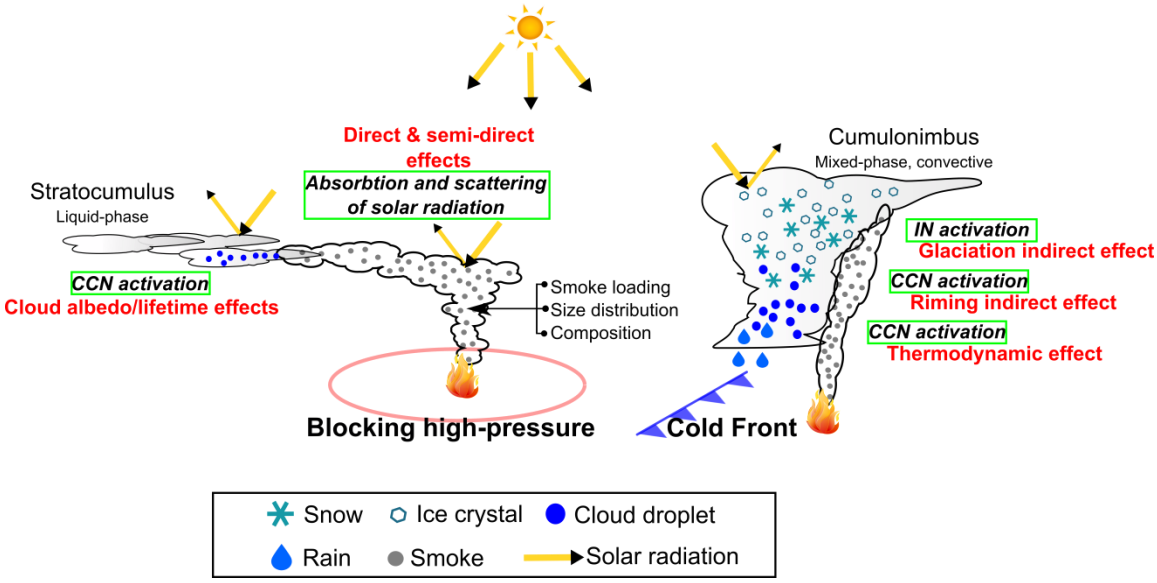

Figure 1.1: Schematic overview of the effects of smoke on radiation, clouds, and precipitation in the boreal region.

Figure 1.1 shows a schematic overview that summarizes the multi-faceted effects of smoke on the radiative energy budget and hydrological cycle in the boreal region. During the burning process, smoke particles are emitted into the atmosphere as an

internal mixture of BC, OM, and other aerosol species (such as sulfates, nitrates, etc.). The BC component of smoke can absorb the solar radiation, while the other components, including OM, can scatter the solar radiation. This effect is called the "direct aerosol effect" of smoke [*Hobbs et al*., 1997]. According to *IPCC AR5* [2013], the global mean radiative forcing due to smoke-radiation interaction is -0.0 (-0.20 to +0.20) W/m^2. *Myhre et al*. [2013] examined the RF_{ari} (radiative forcing due to the direct aerosol effect) of smoke from AeroCom Phase II simulations and found that, in the boreal region, the zonal mean of the RF_{ari} of smoke is a small cooling effect (AeroCom model mean < 0.05W/m^2). However, during an extreme fire event, the local RF_{ari} can be significant. For example, *Péré et al*. [2014] examined the direct radiative effect of the 2010 Russian wildfires and found that, over a large part of Eastern Europe, the smoke significantly reduces the diurnal-averaged solar radiation at the ground by 80-150 W/m^2. In high latitudes, the RF_{ari} of smoke can even vary from a cooling effect to warming effect, depending on the surface albedo [*Stone et al*., 2008].

Absorption of solar radiation by smoke can also heat the atmosphere and further reduce the cloud lifetime by evaporating the cloud droplets or increasing the atmospheric stability (the so called "semi-direct" aerosol effect) [*Ackerman et al*., 2000; *Koren et al*., 2004; *Feingold et al*., 2005]. In *IPCC AR5*, this effect is no longer considered as a single radiative forcing agent, but considered as an adjustment to the RF_{ari}. Many studies on smoke-radiation interaction do not explicitly distinguish direct and semi-direct effects [e.g. *Tosca et al., 2010, Tosca et al., 2013, Ge et al., 2014*]. *Tosca et al*. [2010] run the Community Atmosphere Model (CAM) and find that the direct and semi-direct aerosol effects of smoke reduce the net shortwave radiation at the surface by 19.1W/m^2 during

August-October in Sumatra and Borneo, while the semi-direct aerosol effect of smoke reduces the cloud fraction and precipitation by 7% and 10%, respectively. However, the responses of deep convective clouds to semi-direct effect are not well determined [*IPCC AR5*, 2013].

It has been known for some time that smoke particles originating from biomass burning can act as cloud condensation nuclei (CCN) [*Hobbs and Radke*, 1969]. The activation of CCN directly depends on the properties of smoke such as size distribution and chemical composition [*Petters et al*., 2009a]. For liquid-phase clouds with a given amount of liquid water, smoke-contaminated clouds have a higher cloud droplet number concentration (CDNC), smaller droplet sizes, and higher cloud albedo compared to smoke-free clouds (referred to as the "first indirect effect" or "cloud albedo effect") [*Twomey*, 1974]. Smaller drops may slow down the collision-coalescence rate and delay the onset of precipitation (referred to as the "second indirect effect" or "cloud lifetime effect") [*Albrecht*, 1989]. The impacts of CCN activated from smoke on liquid-phase clouds have been confirmed by several observations and modeling studies [*Rosenfeld*, 1999; *Martins et al*., 2009; *Langmann*, 2007; *Graf et al*., 2009]. However, to what extent the CCN activation from smoke affects the convective mixed-phase cloud remains highly uncertain.

Andreae et al. [2004] and *Rosenfeld et al.* [2008] proposed the mechanism of aerosol (smoke) affecting convective clouds as the following: more CCN activated from aerosol delay the formation of rain, and prolong the cloud lifetime. As a result, more ice-phase hydrometeors are formed at a higher altitude associated with a large amount of latent heat release. Hence, the convective clouds will become more vigorous. This effect

is referred to as the "thermodynamic effect" in *Lohmann and Feitcher* [2005]. However, the strength, or even the sign, of this effect strongly depends on the variety of environmental parameters (such as convective available potential energy, relative humidity, and vertical wind shear) [*Khain et al.*, 2005; *Fan et al*., 2009]. For example, *Seifert and Beheng* [2006] found that aerosols (CCN) have different impacts on single cell and multicell storms. In the case of single cell storms, more aerosols lead to suppression of precipitation and maximum updraft velocity, while in the case of multicell storms, more aerosols promote the formation of more intense secondary convections. *Lee* [2011] simulated meso-scale cloud ensembles (MCEs) using the cloud resolving model (CRM) and found that increasing aerosol loading leads to cloud droplets with smaller sizes, which are much easier to evaporate. The evaporative cooling in the downdraft causes a stronger cool pool and low-level convergence, which in turn generates more secondary clouds and precipitation in a multiple-cloud system. However, the opposite result, weakening of the cool pool due to more aerosols, is also reported in several modeling studies [*Van den Heever and Cotton*, 2007].

More CCN can also affect another important ice-phase microphysical process: riming (snow collecting cloud droplets during fallout). *Borys et al*. [2003] shows that polluted clouds rime less efficiently because smaller cloud droplets are hard to collect. As a result, the formation of snow is suppressed, and the precipitation is also reduced. The importance of this so-called "riming indirect effect" [*Lohmann and Feitcher*, 2005] has been proven both by observation and modeling studies [*Lance et al*., 2011; *Saleeby et al*., 2009]. *Morrison et al*. [2008] conducts a sensitivity test and finds that the size-dependent collection efficiency accounts for about one-fourth to one-half of the differences in the

ice water path and precipitation rate due to aerosol pollution. *Lu and Sokolik* [2013b] found that precipitation has a non-linear response to the amount of smoke, mainly due to the riming indirect effect.

Smoke particles can also function as ice nuclei (IN) [*Hoose and Möhler*, 2012]. For example, field measurements by *Cozic et al*. [2008] demonstrated that combustion aerosols, including smoke, can act as heterogeneous IN in mixed-phase clouds (-28°C~ -5°C). The laboratory and field measurements by *Petters et al.* [2009b] and *Prenni et al.* [2012] also showed IN activations from smoke particles in cold cumulus (-30°C). Using a polarization lidar, *Sassen and Khvorostyanov* [2008] found that smoke can affect cirrus clouds by acting as IN. More ice crystals formed from IN can quickly glaciate supercooled cloud droplets via the Bergeron-Findeisen process, enhance the precipitation, and reduce the cloud lifetime, which is known as the "glaciation indirect effect" [*Lohmann*, 2002]. *Khain et al*. [2008] speculates that primary ice nucleation plays a more important role in frontal clouds (as well as stratocumulus clouds) than in cumulus clouds in the Amazon. However, how smoke IN affect the cloud microphysical properties and precipitation of convective mixed-phase clouds is still largely uncertain. By modeling a convective storm in Florida, v*an den Heever* et al. [2006] found that the case with more IN alone leads to a higher onset temperature for ice crystals and the largest surface rainfall as compared to other cases with high CCN. *Seifert et al*. [2012] found that an increase in the IN concentration results in decreased cloud water path because of higher freezing efficiency, and leads to more snow water path. However, the domain-averaged precipitation is relatively less affected.

In order to unravel the complexity of smoke-cloud interactions, many studies have utilized and developed fully coupled meso-scale models [*Grell et al*., 2011; *Lu and Sokolik,* 2013b]. Compared to climate models (e.g. CAM in *Tosca et al*. [2012]), meso-scale models are much better able to represent the multiple mechanisms (e.g. microphysical and macrophysical buffers) that may absorb or offset some of the aerosol perturbations [*Stevens and Feingold,* 2009; *Lu and Sokolik,* 2013a]. The meso-scale models have brought to light the possibility of simulating the interactions between smoke and synoptic systems (like a cyclone or a frontal system) in the boreal region, since the spatial resolution of meso-scale models (<10 km) is fine enough for resolving the convection, and the domain coverage (> 1000 km) is large enough for modeling the spatial inhomogeneity of smoke plumes and the evolution of the synoptic systems [*IPCC AR5,* 2013]. The meso-scale models are usually performed in conjunction with satellite observations, which provide inputs, especially the time series of smoke emissions, into the models and constrain the modeled smoke and cloud fields. Realistic modeling of the smoke-radiation-cloud-precipitation interaction in the boreal regions faces two major challenges: 1) uncertainties in estimating the smoke emissions [*Langmann et al.*, 2009] and 2) poor representations of smoke-induced changes in cloud microphysical processes (especially ice-phase processes) [*Bond et al*., 2013; *IPCC AR5*, 2013].

The estimation of smoke emissions is usually based on a bottom-up approach and satellite observations of fire properties. The majority of the smoke emission models are built on the book-keeping burned area-technique (BA) [*Seiler and Crutzen*, 1980], in which the mass of smoke emissions (M, kg) is expressed as:

$$M = a \cdot \alpha \cdot \beta \cdot EF \tag{1.1}$$

where a is the burned area (m^2), α is the available biomass fuel (kg carbon/m^2); β is the combustion factor (unitless), and EF is the emission factor for smoke particulate matter or the specific aerosol component (kg/kg carbon). The developments in remote sensing instruments (AVHRR, GOES, MODIS, etc.) and fire retrieval algorithms since the 1980s [*Dozier*, 1981; *Prins and Menzel*, 1992; *Giglio et al*., 2003; *Roy et al*., 2005] make accurate estimation of burned area time series at the regional and global scale feasible.

Two types of fire products on different theoretical bases can be used to generate the burned area time series. The first type (so-called "burn scars" type) is based on changes in the surface reflectance (e.g. MODIS burned area product MCD45A1[*Roy et al*., 2005]) or the vegetation index (e.g. MODIS direct broadcast burned area algorithm [*Giglio et al*., 2009]). The advantage of the "burn scar" type of product is obvious: No additional assumptions are needed to apply the BA technique since it already reports the final total size of the burned area [*Roberts et al*., 2011; *Pentrenko et al*., 2012; *Randerson et al*., 2012]. However, in this type of product, the uncertainty associated with the date of burn (DOB) is too large (±8 days) for meso-scale modeling [*Roy et al*., 2005]. The second product type, "active fire," is derived from the fire signature of high brightness temperatures in mid-infrared channels [*Dozier*, 1981]. Derived from the observations of GOES satellites, the WF_ABBA (wildfire automated biomass burning algorithm) product reports the instantaneous estimation of sub-pixel fire sizes with high temporal resolution (15~30 minutes) but relatively low spatial resolution (especially for high latitude, 6km×8km) [*Prins et al*., 1998]. The instantaneous fire size is usually treated as a proxy for the burned area; however, this assumption could lead to biases. For example, when applying the WF_ABBA product in modeling extreme wildfire events, many studies

significantly underestimate smoke emissions by 5 to 10 times as compared to aerosol optical depth (AOD) observations [*O'Neil et al., 2006*; *Wu et al*., 2011; *Lu and Sokolik*, 2013b; *Reid et al*., 2009]. In these extreme cases, fire may propagate very fast and leave a burned area larger than all instantaneous fire sizes combined. Underestimation of smoke loading may also result from the limited capability of WF_ABBA above 60°N [*Reid et al*., 2009].

The other three factors (α, β, EF) in Eq. 1.1 primarily depend on the vegetation types of biomass fuel, which can be obtained by projecting the burned area to vegetation/land cover maps such as GLCC (Global Land Cover Characteristic data base) v2 map for FLAMBE (Fire Locating And Monitoring of Burning Emissions) smoke emission inventory [*Reid et al*., 2009], the MODIS IGBP (International Geosphere Biosphere Programme) map for FINN (Fire INventory from NCAR) smoke emission inventory [*Wiedinmyer et al*., 2011], and GLC2000 (Global Land Cover 2000) in [*Pentrenko et al*., 2012]. The uncertainties associated with these three factors are noticeable, and hamper the accuracy of smoke emission estimation [*Langmann et al*., 2009]. For example, the available biomass fuel in boreal North America can easily vary by a factor of 3-20 within a region of limited ecosystem diversity [*McKenzie et al*., 2007].

In order to shortcut the uncertainties associated with the last three factors in the BA technique, *Kaufmann et al.* [1998] and *Ichoku and Kaufmann* [2005] suggested a novel technique for estimating smoke emissions. In this technique, the fire radiative power (FRP) is utilized as the driver for estimating smoke emissions. FRP is retrieved as a function of brightness temperatures at 4 μm channel. The FRP values of active fires are usually obtained from the MODIS active fire product MOD/MYD14 (or MCD14ML). In

this technique, the smoke emissions rate of active fire is proportional to the FRP value. The ratio of the smoke emissions rate to FRP, called the particulate matter emission coefficient (C_e) in some studies, is a function of regions [*Ichoku and Kaufmann*, 2005] or vegetation types [*Sofiev et al*., 2009; *Kaiser et al*., 2012]. Despite the superior spatial resolution of the MODIS active fire product, its temporal resolution is limited by the orbit of satellites.

Each satellite product and technique discussed above has its own advantages and limitations in terms of estimating the smoke emissions. Many studies integrate multiple satellite products and generate a more accurate time series of smoke emissions [*Giglio et al*., 2010; *Zhang et al*., 2011; *Randerson et al*., 2012; *Roberts et al*., 2011; *Freeborn et al*., 2011], because using multiple products can compensate for the limitations of one individual sensor. For example, *Randerson et al*. [2012] integrated active fire product (fire count) with burned area product, because the former can provide additional information about small fires. The ratio of burned area to fire count is applied to the fire signals that are only detected by the active fire product. *Zhang et al.* [2011] also calculated the ratios of burned areas (Landsat TM/ETM+-based burn scars) to fire counts (AVHRR and MODIS). In addition, the fire duration derived from the WF_ABBA product is used to constrain the diurnal pattern of fires.

The smoke emissions are injected to different altitudes, depending on burning phases (flaming or smoldering phases), vegetation types of biomass fuel, and environmental conditions [*Kahn et al*., 2008; *Val Martin et al*., 2012]. The smoke injection height is critical for determining the transportation of smoke plumes [*Sessions et al*., 2011] and RF_{ari} of smoke [*Myhre et al*., 2013]. However, many modeling studies

assumed that the smoke particles are either emitted to the first layer of the model [e.g. *Graf et al*., 2009] or to a certain height [e.g. *Wang et al*., 2006; *Pfister et al*., 2008]. *Freitas et al.* [2007] developed a physically based plumerise model, which can calculate the smoke injection height from different types of vegetation. The plumerise model has been successfully coupled in the RAMS [*Freitas et al*., 2009] and WRF-Chem models [*Grell et al*., 2011]. However, *Sessions et al*. [2011] demonstrated that the plumerise model is very sensitive to the assumptions about the burned areas.

Table 1.1: Meso-scale modeling studies that focus on the impact of smoke or aerosol on microphysical processes.

Paper	Model	Region	Size and composition	Smoke's effect on liquid-phase process	Smoke's effect on ice-phase process
Martins et al. [2009]	BRAMS	Amazon	N/A	Fixed CCN	N/A
Graf et al. [2009]	REMOTE-CCFM	Indonesia	TPM	Empirical CCN activation	N/A
Grell et al. [2011]	WRF-Chem	Alaska	Yes(fixed σ); OM+BC	Prognostic CCN (ARG scheme [b])	N/A
Wu et al. [2011]	WRF-Chem	Amazon	Yes(fixed σ); OM+BC	Prognostic CCN (ARG scheme)	N/A
Ten Hoeve et al. [2012]	GATOR-GCMOM	Amazon	Yes; OM+BC	Prognostic CCN	PK97 IN scheme[c]
Morrison et al. [2008][a]	MM5	Alaska	Prescribed aerosol	Diagnostic CCN (ARG scheme)	Size-dependent RCE[d]
Saleeby et al. [2009][a]	RAMS	Colorado	Prescribed aerosol	Diagnostic CCN	Size-dependent RCE[d]
Seifert et al. [2012][a]	COSMO-DE	Germany	Prescribed aerosol	Diagnostic CCN (look-up table)	P08 IN scheme[e]

[a] Three studies consider general aerosols
[b] ARG scheme: *Abdul-Razzak and Ghan* [2000] scheme
[c] PK97 IN scheme: *Pruppacher and Klett* [1997] ice nucleation scheme
[d] Size-dependent RCE: size-dependent riming collection efficiency
[e] P08 IN scheme: *Phillips et al.* [2008] ice nucleation scheme

Recently, significant efforts have been focused on developing a more complex representation of microphysical processes and better coupling of them to atmospheric aerosols [e.g. *Saleeby et al*., 2009; *Gustafson et al*., 2007; *Yang et al*., 2011]. Table 1.1 reviews how the microphysical processes are coupled with the properties of smoke (or general aerosols) in recent meso-scale modeling studies. Physically-based coupling between smoke (the aerosol module) and cloud (the microphysics module) requires information on smoke size distribution, chemical composition, and mixing state. In *Graf et al*. [2009], the smoke emissions are incorporated in the model as total particulate matter (TPM); therefore, only the empirical relationship between smoke mass concentration and CCN number concentration can be applied. In the studies [e.g. *Grell et al*., 2011; *Wu et al*., 2011] that employ the WRF-Chem model [*Grell et al*., 2005], the smoke emissions are size- and composition-resolved. For example, the chemical composition of freshly emitted smoke particles is assumed as a function of the vegetation type of biomass fuel. (The size distribution of fresh smoke particles is prescribed, with a fixed standard deviation σ). In addition, the WRF-Chem model is able to simulate many processes (e.g. coagulation, dry/wet deposition) that are related to the evolution of smoke particles. Coupled with the aerosol properties, the WRF-Chem model is able to calculate the CCN activation using a physically-based parameterization, the *Abdul-Razzak and Ghan* [2000, hereinafter ARG] scheme [e.g. in *Gustafson et al*., 2007]. The performance of the ARG scheme has been systematically evaluated in *Ghan et al*. [2011]. The results reveal that the ARG scheme performs well under the most common conditions compared to more complex parameterizations, such as the Nenes scheme [*Fountoukis and Nenes*, 2005].

The impacts of smoke on ice-phase microphysical processes (e.g. primary ice nucleation and the riming process) are poorly represented in the majority of meso-scale models as shown in Table 1.1. The poor representation is, to a great extent, due to our inadequate understanding of the ice-phase microphysical processes [*IPCC AR5*, 2013; *Fridlind et al*., 2007], and is also partially due to the limitation of the one-moment microphysics scheme used in meso-scale models (e.g. the Lin microphysics scheme in WRF-Chem [*Grell et al*., 2012; *Wu et al*., 2011]). In contrast, a two-moment microphysics scheme (e.g. the Morrison two-moment scheme [*Morrison et al*., 2005]) predicts both the number concentrations and the mixing ratios of hydrometeors; therefore, it allows the effective radius to evolve in a realistic manner, which is critical for several microphysical processes, such as riming.

Although the importance of IN has been discussed above, the majority of studies that focus on the smoke-cloud-precipitation interaction do not directly account for the IN activated from smoke particles. Either the effect of IN is not considered at all [*Graf et al*., 2009], or temperature-dependent ice nucleation parameterizations are employed [*Langmann*, 2007; *Wu et al*., 2011; *Grell et al*., 2012; *Ge et al*., 2014]. Significant efforts have been devoted to the development of heterogeneous ice nuclei parameterizations, either through in-situ measurement and laboratory experiments or through derivation of classical theory (e.g., *Lohmann and Diehl*, [2006]; *Hoose et al*., [2008]; *DeMott et al*. [2010]; *Phillips et al*. [2008]; *Khvorostyanov and Curry* [2004]). When tested in modeling studies, these ice nucleation parameterizations yield diverse results in predicting the IN number concentrations [*Eidhammer et al*., 2009; *Curry and Khvorostyanov*, 2012]. It is worth mentioning that the Phillips scheme [*Phillips et al*.,

2008], which can be tuned to predict IN activated from smoke particles (OM+BC), and account for many smoke aerosol properties, such as aerosol concentration, composition, and size distribution, is in good agreement with recent observations [*Eidhammer et al*., 2010].

1.2 Goal and Outline of Dissertation

As discussed above, the meso-scale model WRF-Chem offers some advantages in modeling the smoke-cloud interactions; however, its performances are impeded by several considerable limitations, such as large uncertainties associated with the smoke emissions and poor representations of the impacts of smoke on ice-phase microphysical processes. Therefore, the goals of this thesis are 1) to develop a fully coupled meso-scale WRF-Chem-SMOKE model by incorporating a selection of smoke emission models and improving the representations of aerosol-cloud interactions in the microphysics scheme; and 2) to address to what extent and how smoke released from boreal wildfires affects local cloud properties, precipitation, and radiative fluxes using WRF-Chem-SMOKE in conjunction with remote sensing observation. The specific objectives are as follows:

1. Compare the performances of different smoke emission models and evaluate the realism of smoke emission datasets and resulting 3D smoke plumes.
2. Examine the effect of varying amounts of smoke emission on cloud properties and precipitation by modeling a short-term 2007 North America wildfire case.
3. Examine the extent to which smoke can alter the cloud properties, precipitation, and radiative fluxes under varying fire regimes and meteorological conditions.

The thesis is organized as follows:

Chapter 2 describes the development of and new capabilities in the WRF-Chem-SMOKE model, which is built on the public version of the WRF-Chem model [*Grell et al*., 2005]. Firstly, we prepare three independent smoke emission models/datasets based on different techniques and fire products, namely the BA technique + WF_ABBA or MCD45A1 products, and FRP technique + MCD14A1 product. The three independent smoke emission datasets are further integrated as one dataset following a novel algorithm. Next, we describe how smoke emissions, with information regarding chemical composition and size distribution, are incorporated into the WRF-Chem-SMOKE model, and how optical and microphysical properties of smoke particles are calculated using Mie code [*Fast et al*., 2006] and the ARG scheme, respectively. Lastly, we improve the Morrison two-moment microphysics scheme by introducing size-dependent riming collection efficiency [*Thompson et al*., 2004] and smoke-property-dependent Phillips heterogeneous ice nucleation parameterization [*Phillips et al*., 2008].

In Chapter 3, we focus on the 2007 eastern Canada wildfire event, which is monitored by several satellites, including GOES satellites, MODIS/Terra, and MODIS/Aqua. We first examine the spatiotemporal distributions of different smoke emission datasets in several major fire clusters and try to interpret the differences by assessing the fire characteristics in each fire cluster, such as fire phase, smoke injection height, and surface wind. The realism of smoke emission datasets is evaluated by comparing the modeled smoke plumes against remote sensing observations. Finally, we examine the effect of varying amounts of smoke emissions on cloud properties, such as total water path (TWP), cloud water path (CWP), rain water path (RWP), and snow water path (SWP), as well as precipitation.

In Chapter 4, we focus on the 2002 central Siberia (Yakutsk) wildfire season. During the entire fire season, the smoke particles are emitted into the atmosphere under different fire regimes and meteorological conditions, namely a strong frontal system, a blocking high-pressure system, and a relatively weak frontal system. Therefore, the CCN and IN activations from smoke, smoke-induced changes in cloud microphysical properties (CWC, RWC, IWC, and SWC), cloud macrophysical properties (cloud coverage and cloud lifetime), and precipitation fields associated with the convective mixed-phase clouds in two frontal systems are all examined in a dynamical/meteorological context. Finally, we evaluate modeled radiation fields (such as upward shortwave fluxes at TOA, $SW_{TOA}\uparrow$) against the NASA GEWEX SRB dataset. The radiative effects due to smoke-radiation interactions and smoke-cloud interactions under different meteorological conditions is also examined.

The main findings are summarized in Chapter 5.

CHAPTER 2

DEVELOPMENT OF THE WRF-CHEM-SMOKE MODEL

2.1 Introduction

This chapter describes the development and new capabilities of a fully coupled meso-scale model WRF-Chem-SMOKE. The WRF-Chem-SMOKE model is specifically designed for examining the impacts of smoke on clouds, radiation, and precipitation in the boreal region. The "on-line" smoke emission is incorporated into the WRF-Chem-SMOKE model, and fully coupled with the dynamical, radiative, and microphysical modules.

The WRF-Chem-SMOKE model must be first initiated by smoke emission datasets with a high innovation frequency (≤ 1 hour, [*Reid et al*., 2009]). In Section 2.3, we design a selection of smoke emission models/datasets for meso-scale modeling based on different techniques and satellite products. In order to maximize the benefits of each smoke emission dataset, we also introduce an algorithm that integrates them together. In Section 2.4, we describe how smoke-radiation and smoke-cloud interactions are treated in the WRF-Chem-SMOKE model. In particular, we improve the cloud microphysics scheme by introducing the Phillips ice nucleation scheme. The main findings are summarized in Section 2.5.

2.2 Overview of the WRF-Chem-SMOKE Model

In this thesis, we employ two versions of WRF-Chem-SMOKE model (v3.1.1 and v3.3.1) , which are built on the corresponding versions of public WRF-Chem model

[*Grell et al.* , 2005]. Two versions of WRF-Chem-SMOKE are employed in Chapters 3 and 4, respectively, and they differentiate from each other, in terms of the treatments of heterogeneous ice nucleation (discussed in Section 2.4). The WRF-Chem public version is modified to compute online hourly smoke emissions (Section 2.3), to link emitted smoke with an aerosol module MOSAIC (section 2.4.1), to compute the aerosol optical properties (Section 2.4.2), and to couple smoke with cloud microphysics processes (section 2.4.3).

Table 2.1: The WRF-Chem-SMOKE model configuration and options.

Model aspect	Setting
Grid	Arakawa C grid; Horizontal grid: $\Delta x=\Delta y=5$km; Vertical grid: 36 vertical layer
Meteorology initialization	NCEP FNL or GFS reanalysis data
Time step	20 seconds
Microphysics	The Morrison two-moment scheme
Radiation	The RRTM longwave radiation scheme The Goddard shortwave radiation scheme
Cumulus	No cumulus parameterization
Land surface	The NOAH land surface model
Planetary boundary layer	the YSU PBL scheme
Gas chemistry driver	The CBM-Z gas chemistry module
Aerosol driver	The MOSAIC aerosol module

Table 2.1 summarizes the WRF-Chem-SMOKE configurations selected for this thesis. The horizontal resolution (5 by 5 km), vertical resolution (36 vertical layers), and time step (20 seconds) are fixed; however, the domain sizes as well as simulation periods vary according to individual wildfire cases. The standard model physics packages used in simulations are as follows: the NOAH land surface model, the YSU PBL scheme, the RRTM longwave radiation scheme, the Goddard shortwave radiation scheme, and the Morrison two-moment microphysics scheme. Since the 5 km resolution grid resolves the vertical motion explicitly, the model does not include any cumulus parameterization. We use NCEP Global Forecast System (GFS) [*Moorthi et al.*, 2001] or FNL (http://rda.ucar.edu/datasets/ds083.2/) reanalysis data to provide the boundary and initial meteorological conditions to the model.

2.3 Smoke Emission Models in the WRF-Chem-SMOKE Model

We prepare three original smoke emission datasets based on different techniques and fire products, namely BA technique + WF_ABBA or MCD45A1 products, and FRP technique + MCD14ML product, which are referred to as ABBA, MCD45, and FRP datasets in this study. In addition, we integrate three smoke emission datasets into a new one (the integrated smoke emission dataset) following an algorithm discussed in section 2.3.4. To initiate WRF-Chem-SMOKE, we calculate the model gridded hourly smoke emission flux $F_j(x, y, t)$ (unit: $kg/m^2/hour$), where x and y indicate the index of model grid, t represents the time step, and j corresponds to different aerosol components in smoke particles. In this thesis, smoke aerosols are assumed to consist of organic matter (OM), black carbon (BC), and residual particulate matter (RPM). We first estimate the

emission fluxes of PM2.5, OM, and BC as described below, so the emission flux of RPM is then computed by subtracting the emission fluxes of OM and BC from that of PM2.5. Introducing the residual particulate matter allows us to close the mass budget gap, given the fact that the total OM and BC mass is smaller than PM2.5 mass in all smoke emission inventories (e.g., *Wiedinmyer et al*. [2011]).

2.3.1 ABBA Smoke Emission Dataset

Mass, M (kg), of the smoke emitted by each active fire can be expressed as:

$$M_{i,j}(lat, lon, t) = a_i \cdot \alpha_i \cdot \beta_i \cdot EF_{i,j} \quad , \qquad (2.1)$$

where i denotes the active fire, j denotes the aerosol type, $M_{i,j}$ (kg) is the emitted mass, *a* is the burned area, α is the available carbon in biomass fuel (kg C/m^2), β is the combustion factor (unitless), EF_j is the emission factor for the j-*th* aerosol type (kg/kg C), lat/lon is the location of the fire pixel center, and t is the time of fire detection.

Smoke mass emissions are computed using the WF_ABBA fire products, which are derived from two mid-infrared channels (3.9 and 11μm) of GOES (Geostationary Operational Environmental Satellites). Because GOES are geostationary satellites, their spatial resolution is relatively low (~4 km at the nadir and ~8 km at limb viewing), while their temporal resolution is high (about 15 minutes). WF_ABBA provides the time of fire detection, the location of the fire (in latitude and longitude), the instantaneous estimates of the sub-pixel fire size, obtained by assuming that measured radiance originates from a linear mixture of fire and background radiances, and the solutions to two nonlinear equations [*Prins et al*., 1998]. A quality flag is reported for each fire detection, ranging from 0 to 5 corresponding to the best quality, saturated fire pixel, cloudy, high-, medium-

and low-probability fires, respectively. It should be noted that the sub-pixel fire size is calculated for only the best quality (flag=0) fire detection.

The processing of the WF_ABBA data in this study involves several steps. Because WF_ABBA records a series stream, we first perform temporal filtering to screen fire detection with the largest estimate of the size of the fire. If the size is not retrieved for one fire detection because of low quality (quality flag>0) data, the hourly domain averaged burned area is assigned to this fire detection. After temporal filtering and filling in the missing values, we use the fire size as a proxy for the burned area.

Table 2.2: Five common GLCC vegetation types associated with active fires in the boreal region and corresponding values of carbon in biomass fuel, combustion factor, and emission factors (described in the text).

GLCC category	Carbon in biomass fuel (kg C/m^2)	Combustion Factor (β)	PM2.5 EF (g/kg C)	OM EF (g/kg C)	BC EF (g/kg C)
Conifer boreal forest	6	0.5	32.0	22.4	1.38
Wooded tundra	2	0.6	17.0	11.1	1.59
Narrow conifers	5	0.5	32.0	22.4	1.38
Cool mixed forest	7	0.5	32.0	22.4	1.38
Mire, bog, fen	2	0.6	17.0	11.1	1.59

The WF_ABBA dataset also provides information on the vegetation type of the burned area based on the USGS 1 km, 99-category Global Land Cover Characterization (GLCC) classification (version 2, http://edc2.usgs.gov/glcc). Vegetation type is assigned to the fire pixel according to the latitude/longitude of the pixel center. Table 2.2 presents five common GLCC vegetation types associated with active fires in the boreal region,

and values for the carbon in biomass fuel based on the Olson dataset [*Gibbs*, 2006]. However, the Olson dataset contains no information regarding the combustion factor β and the emission factor EF for the GLCC 99 vegetation categories. Therefore, we adopt the combustion factors and emission factors for PM2.5 from *Reid et al*. [2009]. These factors are reported for ten bulk vegetation types, which are formed by grouping the GLCC 99 vegetation categories based on the similarities in ecosystem and burning behaviors [*Reid et al*., 2009]. For the factors β and EFs of conifer boreal forest, narrow conifers, and cool mixed forest categories, we adopt the values of that of "Temperate/Boreal-Low" (see Table II in *Reid et al.* [2009]). For wooded tundra and mire, bog, fen categories, we take the values of "Light Grasses/tundra" and "Wetland", respectively. Because *Reid et al.* [2009] does not provide chemical speciation of PM2.5, we adopt the OM/BC/PM2.5 mass ratios from *Wiedinmyer et al*. [2011], who specifically consider the chemical composition of smoke emitted by boreal forest wildfires. We multiply the *Wiedinmyer et al*. OC/PM2.5 mass ratios by a factor of 1.4 to obtain the OM/PM2.5 mass ratio [*Reid et al*., 2005]. However, we find that the BC fractions reported by *Wiedinmyer et al*. [2011] are too low compared to other studies. For instance, the BC/OC mass ratio for boreal forest is 0.026 in *Wiedinmyer et al*. [2011] but it is 0.062 in *Andreae and Merlet* [2001], 0.1 in *Petrenko et al.* [2012], and 0.07 in *Reid et al*. [2005]. Therefore, we adjust the BC/PM2.5 mass ratios by using values from *Andreae and Merlet* [2001]. Thus we use the OM/BC/PM2.5 ratio of 0.71/0.04/1 for conifer boreal forest, narrow conifers, and cool mixed forest (that corresponds to the "Boreal Forest" category in *Wiedinmyer et al*. [2011] and "Extratropical Forest" in *Andreae and Merlet* [2001]). Our OM/BC/PM2.5 ratio for wooded tundra and mire, bog, fen (the "Savanna

and Grassland" category in *Wiedinmyer et al*. [2011] and *Andreae and Merlet* [2001]) is 0.65/0.09/1.

The smoke emission released from each detected fire is re-gridded to WRF grids. The smoke emissions occurred during the t to $t+t_{if}$ period are interpolated into model grids based on the location of the fire pixels. Here, t_{if} is the innovation frequency, according to which smoke emission inputs are updated in the model. The emitted smoke mass from all active fires in the same grid (x, y) within the t_{if} time period are summed. Re-gridded smoke emission fluxes, F ($kg/m^2/s$), for each aerosol type j are computed as

$$F_{j,ABBA}(x,y,t) = \frac{M_{j,ABBA}(x,y,t)}{A(x,y)\cdot t_{if}} \qquad (2.2)$$

where M_j denotes the mass of the j-*th* aerosol type emitted by all active fires that occurred within one hour at model time step t in the (x, y) grid. Here, A (m^2) is the area of grid (x, y). *Reid et al.* [2009] suggested that for mesoscale modeling the innovation frequency (t_{if}) should be around or smaller than one hour. Actually, t_{if} can be as small as 15 min. (i.e., the temporal resolution of WF_ABBA); however, we select t_{if} = 1 hour, mainly because of its computational efficiency. It should be noted that, as discussed in Chapter 1, a correction factor must be applied to the ABBA smoke emission dataset, since the ABBA dataset usually underestimates the smoke emissions. In this thesis, we determine the multiply factor by comparing modeled smoke AOD against MODIS AOD. (e.g. in Chapter 3, the multiply factor equals 10 for the 2002 eastern Canadian wildfire case)

2.3.2 MCD45 Smoke Emission Dataset

Retrieved from the MODIS observation of burn scars (fire-induced changes in surface reflectance), the MCD45A1 product reports the approximate date of burn (DOB)

for fire pixels at a spatial resolution of 500m. However, the uncertainty associated with the DOB is +/- 8 days, which is significant. Therefore, the DOB must be aligned to the dates when actual burning occurs. In order to do so, we adopt an approach similar to the one in [*Roberts, et al*., 2011]. During one particular day "D", we assume a buffer zone with 1 km radius for each BA pixel, and search for the active fire pixel observed by MODIS (the MCD14ML product) in this buffer zone during the same day. If the corresponding active fire pixel does not exist, we keep searching in the time windows of D±1, D±2 ..., D±8, until we find the temporally closest one, and adjust the DOB. However, if the corresponding active fire pixel is not found within a ±8 days time window, we do not adjust the DOB.

As a "burned scar" type of product, the MCD45A1 product can be used in the BA technique without any assumptions. Therefore, the MCD45 smoke emission dataset is calculated in a manner similar to the ABBA dataset. By replacing the instantaneous estimations of sub-pixel fire sizes of WF_ABBA product by the burned area (the area of burned pixel) of the MCD45A1 product, we obtain the mass of *j-th* component in smoke particles emitted during "D" day in model grid (x,y), $M_{j,MCD45}(x,y,D)$. We assume a uniform emission rate for each burned area pixel through the day; therefore, the smoke emission flux $F_{j,MCD45}(x,y,t)$ equals $M_{j,MCD45}(x,y,D)$ divided by the model grid area A and then by 24 hours. Although we do calculate the model gridded MCD45 smoke emission dataset, we do not incorporate it in the WRF-Chem-SMOKE model, because the uniform smoke emission rate is not capable of depicting the diurnal cycle of fire activity. The MCD45 smoke emission dataset is only used in the algorithm for integrating the smoke emission datasets.

2.3.3 FRP Smoke Emission Dataset

For each fire detected by MODIS in the MCD14ML product, the fire radiative power (FRP, in megawatts) is calculated as:

$$FRP = 4.34 \times 10^{-19}(T_4^8 - T_{4b}^8) \quad (2.3)$$

where T_4 is the brightness temperature at the 4 μm channel, and T_{4b} is the background (pixels surrounding the fire pixels) brightness temperature at the same channel. The smoke emissions rate is then calculated as:

$$dM_{i,j}(lat, lon, ts)/dt = C_e \times FRP_i(lat, lon, t_S) \times r_{i,j}(lat, lon) \quad (2.4)$$

where i denotes each active fire detected by MODIS, j denotes aerosol type, lat and lon indicate the location of the fire detection, t_S is the satellite/MODIS overpass time, and $dM_{i,j}/dt$ is the emission rate of *j-th* smoke aerosol component (kilograms per second). C_e is the particulate matter emission coefficient, which equals 0.02kilograms per megawatts for North America (table II in *Ichoku and Kaufman*, [2005]), and $r_{i,j}$ is the mass ratio of the *j-th* component in smoke particles. Similar to the BA technique discussed above, the OM/PM2.5 and BC/OM2.5 ratios are adopted from *Wiedinmyer et al*. [2011] and *Andreae and Merlet* [2001], respectively. The active fire detections are projected to the 17-category MODIS IGBP land cover map in the FRP technique because the OM/PM2.5 ratios were originally built for the MODIS IGBP land cover map in *Wiedinmyer et al*. [2011]. (It should be noted, for the BA technique, we use the 99-category GLCC land cover map because it can provide available biomass fuel for 99 land cover categories according to the Olson dataset [*Gibbs*, 2006].)

In order to construct the diurnal cycle of fire activity, we divide a "day" (from 0800 LST to 0800 LST next day) into three periods: one daytime period (0800 LST-2000

LST) and two nighttime periods (2000 LST-0200 LST and 0200 LST-0800 LST). For the daytime period, we assume that the fire activity follows a modified Gaussian function [*Ellicott et al*., 2009]:

$$R(t) = \left[b + (\exp(-(t-h)^2 / 2\sigma^2))\right] \Big/ \sum_{n=1}^{24} \left[b + (\exp(-(n-h)^2 / 2\sigma^2))\right] \qquad (2.5)$$

where t is the physical time, and parameters b and σ equal 0.4 and 3.5, respectively [*Ellicott*, personal communication]. The parameter h represents the hour when fire activity peaks (1430 LST). With the emission rate (dM/dt), the overpass time (t_S), and location (lat, lon) of each fire detected by MODIS in the daytime period, we extrapolate the emission rate to any time t in daytime as the following:

$$dM'_{i,j}(lat, lon, t)/dt = dM_{i,j}(lat, lon, t_S)/dt \times R(t)/R(t_S), \qquad (2.6)$$

Terra and Aqua satellites overpass the study domain within 2000 LST-0200 LST and 0200 LST-0800 LST, respectively. During these two nighttime periods, Terra and Aqua acquire two more sets of fire detections. For one particular nighttime period, we assume the fields of FRP remain fixed. Therefore, the smoke emission rate of *i-th* active fire during the nighttime becomes:

$$dM'_{i,j}(lat, lon, t)/dt = dM_{i,j}(lat, lon, t_S)/dt . \qquad (2.7)$$

The same *i-th* fire can be detected multiple times due to overlaps of the orbits at high latitudes; therefore, each detection yields different reconstructed smoke emission rates $dM'_{i,j}(lat,lon,t)/dt$. In our study, we select the one with the largest values due to the possibility of cloud contamination, etc. The smoke emission rate of i-th active fire during time t $dM'_{i,j}(lat,lon,t)/dt$ is further gridded to the (x,y) model grid. The gridded smoke

emission flux in the (x, y) model grid during the t to $t+t_{if}$ time window is calculated as following:

$$F_{j,FRP}(x,y,t) = \frac{dM_{j,FRP}(x,y,t)/dt}{A(x,y)} \quad (2.8)$$

2.3.4 A methodology for integrating three smoke emission datasets

As discussed in Chapter 1, many previous studies tried to integrate different satellite observations to improve the estimation of one factor in either the BA technique or FRP technique. In this thesis, we directly integrate three smoke emission datasets calculated from different techniques and satellite products. The integration of three smoke emission datasets is performed on a model grid basis, similar to the methodology in *Roberts et al.* [2011], which is done on a fire cluster basis. The model grid at a spatial scale of 5km can be considered as a small cluster of the MODIS active fire (1km) or the burned area (500m) pixels. In contrast, the resolution of the GOES pixel (~6km×8km) is slightly coarser than the model grid; therefore, we consider the model grid with the ABBA smoke emissions and its surrounding 8 model grids as the buffer zone for the GOES pixel. The area of buffer zone in our study (~225km^2) is slightly smaller than the one assumed in *Soja et al*. [2009] (~314km^2), in which the buffer zone is assumed as a circle with a radius of 10km. Figure 2.1 shows an overview of the methodology for integrating the three smoke emission datasets, which is done in three steps.

Step 1. Modifying the fire duration of the FRP smoke emissions according to the ABBA smoke emissions

The integrated smoke emission dataset is mainly built on the FRP smoke emission dataset, because of its optimal spatial resolution and its ability to detect small fires. However, the assumption of 12 or 6 hours of fire duration may be inappropriate for some

short-lived fires. Therefore, the first step of integration is to merge FRP and ABBA smoke emission datasets, the latter of which provides high temporal resolution observations.

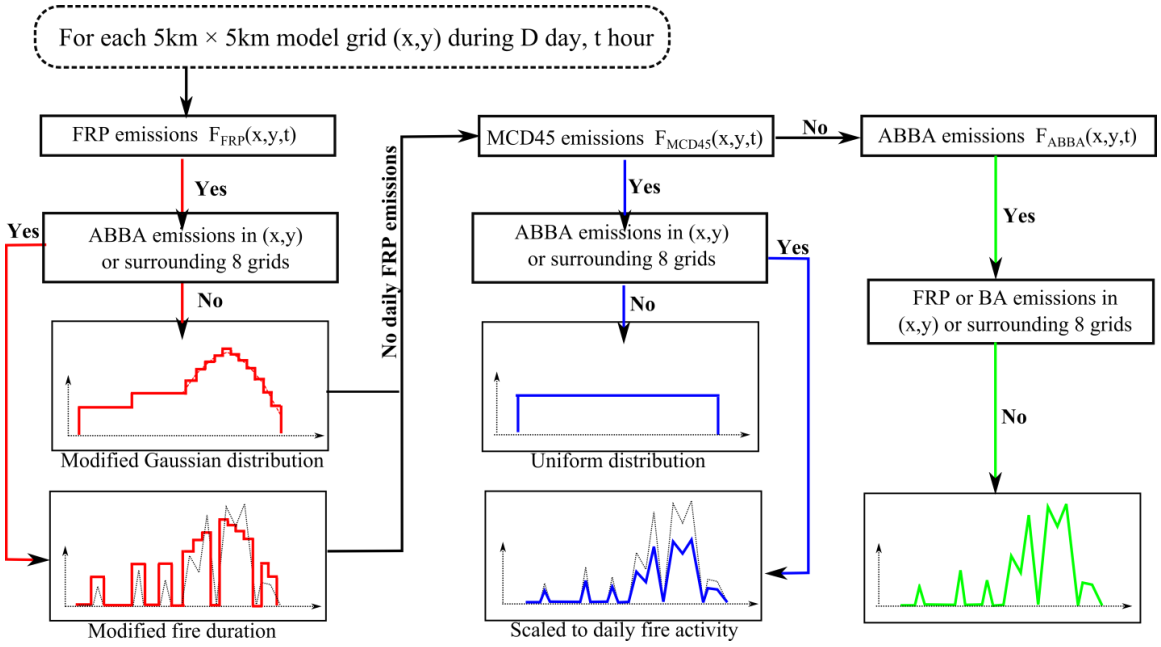

Figure 2.1: The diagram of methodology for integrating three different emission datasets

For a model grid (x,y) with FRP smoke emissions $F_{FRP}(x,y,t)$, the fire duration of active fires is adjusted according to the ABBA smoke emissions in (x,y) and surrounding 8 model grids (the buffer zone of the ABBA smoke emissions). In other words, if the sum of ABBA smoke emissions in (x,y) and surrounding 8 model grids equals zero during time step t, then we assume there should be no fire activity in the (x,y) grid, and set $F_{FRP}(x,y,t)$ to zero; otherwise the values of FRP smoke emissions will not be modified. The modified FRP smoke emissions are assumed as the integrated smoke emissions. It should be noted that the routine introduced above is only applied if the sum of daily ABBA smoke emissions in (x,y) and surrounding 8 model grids is larger than zero. Some active fires, especially those of small size, are usually detected only by the

MODIS/MCD14ML product, and omitted by the GOES/WF_ABBA product. In this case (the sum of daily ABBA smoke emissions in (x,y) and surrounding 8 model grids equals zero), we do not modify the fire duration (still 6 or 12 hours) and the values of FRP smoke emissions. To sum up step 1, the integrated smoke emissions are expressed as following:

$$F_{INTEGRATED}(x,y,t) = \delta \cdot F_{FRP}(x,y,t)$$

$$,\delta = \begin{cases} 0, if \sum_{m=x-1}^{x+1}\sum_{n=y-1}^{y+1} F_{ABBA}(m,n,t) = 0, and \sum_{k=1}^{24}\sum_{m=x-1}^{x+1}\sum_{n=y-1}^{y+1} F_{ABBA}(m,n,k) \neq 0 \\ 1, otherwise \end{cases} \quad (2.9)$$

Step 2.Partitioning the daily MCD45 smoke emissions following the fire activities derived from the ABBA smoke emissions

For the model grid (x,y) with no FRP smoke emissions, we cannot exclude the possibility of the occurrence of fires in (x,y), because the MCD14ML product may miss the fire detection due to 1) the short lifetime of the fire or 2) cloud contamination. In addition, the MCD14ML product is based on the active fire-type of the detection, so including the burn scar-type of detection as in the MCD45A1 product is extremely critical. After step 1, in the model grid (x,y) with no daily FRP smoke emissions, we examine whether MCD45 smoke emissions exist or not. When preparing the hourly MCD45 smoke emission dataset (section 2.3.2), we assume a uniform smoke emission rate through 24 hours; however, the fire activity within a day can be improved by incorporating the WF_ABBA products. We sum the hourly ABBA smoke emissions in (x,y) and the surrounding 8 model grids, and use this time series of hourly smoke emissions to describe the diurnal cycles of fires in (x,y) in a day. The daily MCD45 smoke emissions in (x,y) are partitioned according to this time series. If the sum of daily

ABBA smoke emissions in (x,y) and surrounding 8 model grids equals zero, we simply assume a uniform smoke emission rate and employ the hourly MCD45 smoke emissions as the integrated one. The integrated smoke emission in (x,y) is calculated as the following:

$$F_{INTEGRATED}(x,y,t) = F_{MCD45}(x,y,t) \cdot \varepsilon$$

$$\varepsilon = \begin{cases} 1, if \sum_{k=1}^{24} \sum_{m=x-1}^{x+1} \sum_{n=y-1}^{y+1} F_{ABBA}(m,n,k) = 0 \\ 24 \cdot \sum_{m=x-1}^{x+1} \sum_{n=y-1}^{y+1} F_{ABBA}(m,n,t) / \sum_{k=1}^{24} \sum_{m=x-1}^{x+1} \sum_{n=y-1}^{y+1} F_{ABBA}(m,n,k), otherwise \end{cases} \quad (2.10)$$

Step 3. Utilizing the ABBA smoke emissions that do not coincide with the FRP and MCD45 smoke emissions in buffer zones

In steps 1 and 2, the ABBA smoke emissions are used for describing the diurnal cycle of fire activity. In step 3, we also utilize the ABBA smoke emissions as one source for the integrated smoke emissions. However, the ABBA smoke emissions are considered to be associated with fires in a buffer zone ((x,y) and surrounding 8 grids), because of the coarse resolution of the GOES satellite at high latitudes. Therefore, to avoid counting the same active fire twice, we only consider the ABBA smoke emissions as the integrated smoke emission dataset in (x,y) if the FRP and MCD45 smoke emissions do not present in (x,y) and the surrounding 8 grids.

2.3.5 Description of the Smoke Injection Height Calculation

The public version of WRF-Chem model includes a 1D plume rise model developed by *Freitas et al.* [2007]. The ability of WRF-Chem 1D plume rise model to produce realistic injection heights was demonstrated by *Grell et al*. [2011] and *Sessions et al*. [2011]. The smoke injection height is calculated by solving five governing

equations [*Freitas et al*., 2007, Eqs.1-5], which are the first law of thermodynamics, the equation for vertical motion, and three continuity equations for water in all phases. The boundary conditions are determined by the thermodynamic stability of the atmosphere as well as by fire properties (i.e., the convective energy flux and the plume radius convective energy flux) in each model grid.

Information on plume radius/size is required. For the ABBA dataset, we assume the plume size to be the instantaneous fire size of the WF_ABBA product. As for the FRP dataset, we follow the approach in the FLAMBE dataset [*Reid et al*., 2009; *Martin et al*., 2012], which assumes a fixed daily burned area of 62.5ha for each MODIS active fire detection. During the daytime, the plume size at time step "t" is assumed as the product of 62.5ha and the modified Gaussian function R(t). As for the nighttime, we simply assume a fixed plume size of 2.6ha (1/24 of 62.5ha). This value is close to the plume size for "transitions hours" adopted in [*Val Martin et al*., 2012] (the plume size for nighttime is 0 in [*Val Martin et al*., 2012]). It is difficult to determine the plume size for the MCD45 dataset, since it reports the burned area instead of the active fire size. In order to be consistent with the other emission datasets, the plume size in the MCD45 dataset is assumed to be 2.6ha through the entire day. The value is about one tenth of the MCD45 pixel area. If the integrated smoke emission dataset $F_{INTEGRATED}(x,y,t)$ is built on one particular smoke emission dataset, then we assume that the plume size also follows the one in this smoke emission dataset, unless the smoke emission in the (x,y) model grid on time step t is set to zero (due to fire duration adjustment for example).

The convective energy flux for each active fire is proportional to the heat flux multiplied by a factor of 0.55. In the plume rise model, the heat flux released during

burning is also a function of the vegetation type. The upper and lower limits of heat fluxes for several vegetation types are listed in Table 1 of *Freitas et al.* [2007]. The limits of heat flux for boreal forest are assumed to be the same as the ones for tropical forest, because of the lack of data.

Smoke emitted from several active fires belonging to different vegetation categories may be injected into one model column at various heights, so the inputs in the plume rise model are provided separately for each vegetation category. The ratios of smoke emissions from one particular vegetation category to total smoke emissions and averaged plume radiuses for all active fires with the same vegetation categories are calculated in the preprocessing package for every model grid with smoke emissions. Together with the upper and lower limits of heat fluxes, the plume rise model calculates the depth of the injection layer for different vegetation categories. Then the time derivative of the smoke mass concentration of the j-*th* species is calculated by summing the contributions from different vegetation categories:

$$dC_j(x,y,z,t)/dt = \sum_l \lambda_l(x,y) \cdot F_j(x,y,t)/\Delta z_l, \qquad (2.11)$$

where λ_l represents the ratio of smoke emission from the l-*th* vegetation category to total smoke emission in model grid (x, y), and Δz_l represents the depth of injection layer for l-*th* vegetation category.

2.4 Smoke-Radiation-Cloud-Precipitation Coupling in the WRF-Chem-SMOKE Model

2.4.1 Treatment of Smoke Particles

Total mass emission fluxes for BC, OM, RPM, and PM2.5, computed in the

preprocessing package as a gridded time series, provide input into the WRF-Chem-SMOKE model. In the public WRF-Chem, smoke emissions are linked only to the GOCART or MADE/SORGAM aerosol modules. For this thesis, we link smoke emissions with the MOSAIC aerosol module, which simulates the evolution of size- and composition-resolved smoke particles accounting for the major aerosol processes such as coagulation, and dry/wet removal [*Zaveri et al*., 2008].

The MOSAIC module [*Zaveri et al.*, 2008] employs the sectional approach for representing the aerosol size distribution in which both the mass of different chemical components) and particle number concentration are predicted in each size bin. The size distribution of each aerosol species in the present study is represented by eight discrete size bins, spaced logarithmically in diameter between 0.039 and 10 μm. In each size bin, aerosols are assumed to be internally mixed (i.e., all particles in a certain bin have the same chemical composition). Based on *Reid et al.* [2005], we assume an initial aerosol size distribution with a volume median diameter (VMD) of 0.26 μm and a standard deviation (σ) of 1.7. The smoke emission flux for the j-*th* aerosol species in the n-*th* bin becomes

$$F_{j,n}(x,y,t) = F_j(x,y,t) \cdot \int_{\ln d1}^{\ln d2} \frac{1}{\sqrt{2\pi}\sigma} \exp\left(-\frac{\ln(d/VMD)}{2\sigma^2}\right) d \ln d \qquad (2.12)$$

where the integral represents the mass fraction for the n-*th* bin with upper and lower diameters d2 and d1, respectively. The function inside the integral is the normalized volume size distribution.

In this thesis, we do not treat background aerosols but introduce a background cloud droplet number concentration field (see section 2.4.3). The CBM-Z gas chemistry module is used for gas chemistry calculations. The initial and boundary conditions of

trace gases are represented by idealized, northern hemispheric, mid-latitude, clean environmental profiles from the NOAA Aeronomy Lab Regional Oxidant Model (NALROM) [*Liu et al.*, 1996] similar to past studies of boreal wildfires [e.g., *Sessions et al*., 2011]. No smoke gas chemistry is treated because of the complexity of fire chemistry.

2.4.2 Treatment of Smoke Optical Properties

In the public version of MOSAIC, each aerosol component is assigned a refractive index. The refractive indices associated with each size bin are calculated by volume averaging. The Mie code is first calculated once for seven representative refractive indices to obtain a table of seven sets of Chebyshev expansion coefficients. For any given refractive index, the full Mie code can be skipped. The extinction efficiency (Q_e) and scattering efficiency (Q_s) of each size bin can be calculated using bi-linear interpolation over these Chebyshev coefficients [*Ghan et al*., 2001]. The extinction, b_{ext}, single-scattering albedo, ω_0, and the asymmetry factor for scattering, g at four wavelengths (0.3, 0.4, 0.6, and 1.0 μm) are determined by summation over all eight size bins [*Fast et al*., 2006]. These optical properties, as functions of space, time, and wavelength, are further coupled with the shortwave radiation scheme, such as the Goddard shortwave radiation scheme [*Chou et al*., 1998].

For the purpose of comparing modeled smoke field against satellite observations, we need to calculate the smoke AOD at wavelength of 0.55μm, which is derived by two approaches in WRF-Chem-SMOKE. In the first approach, we follow [*Wang et al*., 2006] and smoke AOD in each model grid (x, y) is calculated as:

$$AOD(x,y) = \sum_{i=1}^{K} Q_i \times C_i \times f(RH_i) \times D_i \qquad (2.13)$$

where *i* is the index of the model layer, K is the total number of model layers, Q_i is the mass extinction coefficient, which equals 4.5 m^2/g at 0.55 μm [*Reid et al.*, 1998], C_i is the smoke mass concentration (g/m^3), f(RH) is the hygroscopic factor as a function of relative humidity, RH, and D is the depth of the i-*th* layer. In the second approach, we calculate the smoke AOD at 0.55 μm using an Angström exponent derived from AOD values at 0.4 and 0.6 μm wavelengths. Aforementioned two approaches are used in Chapter 3 and Chapter 4, respectively.

2.4.3 Treatment of Smoke-Cloud Interactions

Activation of CCN is modeled using the *Abdul-Razzak and Ghan* [2000] parameterization, which is linked with the MOSAIC module in WRF-Chem. This parameterization treats multiple aerosol size bins, each composed of an internal mixture of aerosol species. The number and mass fractions of activated aerosol particles depend on a Gaussian spectrum of updraft velocities and the properties of aerosols in each size bin (e.g., the hygroscopicity) [*Abdul-Razzak and Ghan*, 2000, *Ghan et al.*, 2011]. Activated aerosol particles may return to the interstitial state after the evaporation of cloud droplets.

Hygroscopicity values, κ, for all aerosol components are required to compute the volume-weighted hygroscopicity of aerosol internal mixtures [*Ghan et al.*, 2011]. The hygroscopicity for OM and BC are taken to be 0.14 and 10^{-6}, respectively. However, it is difficult to select a representative hygroscopicity value for residual particular matter because it may consists of various chemical species. For instance, *Kondo et al.* [2011] report the presence of several species in freshly emitted smoke in Canada in addition to

OM and BC, including sulfates (8.63% by mass), ammonia (5.12%), nitrates (3.87%), and chlorides (0.2%). The hygroscopicity of these species may be much higher than that of OM. Other studies, for instance *Carrico et al.* [2010], report the presence of species with much lower hygroscopicity values. Given the inherent uncertainty, we consider two possible options for the hygroscopicity of RPM: high hygroscopicity (κ=0.5, similar to sulfates) and low hygroscopicity ($\kappa=10^{-6}$, similar to BC). The effect of hygroscopicity of RPM is examined in Chapter 3 and only high hygroscopicity is employed in Chapter 4. It is worth mentioning that taking emission factors for the boreal forest categories (Table 2.1) gives an estimate of the volume-weighted hygroscopicity of freshly emitted smoke particles of 0.19 and 0.11 for the high and low hygroscopicity of RPM, respectively. These values are in good agreement with measurements (κ=0.18) reported by *Lathem et al*. [2013] for Canadian wildfires.

In the public WRF-Chem model, the predicted number concentration of cloud droplets is passed to the Lin microphysics scheme [*Chapman et al*., 2009]. In WRF-Chem-SMOKE, we choose to use the Morrison two-moment microphysics scheme [*Morrison et al*., 2005], which we have coupled with the MOSAIC and Abdul-Razzak and Ghan parameterization. Compared to the Lin scheme, the Morrison scheme has several advantages. For one, it predicts the number concentration and the mass mixing ratio of five hydrometeors (cloud droplets, cloud ice, rain, snow, and graupel). Furthermore, it was specifically designed for mixed-phase clouds, which are common in northern latitudes and are of interest to this thesis.

For the coupling, we replaced the fixed cloud droplet number concentration (CDNC) with prognostic CDNC predicted by the Abdul-Razzak and Ghan

parameterization, which affects the processes such as autoconversion, immersion and contact freezing, and the accretion of cloud droplets by rain, snow, and graupel; added calculation of the loss rate of cloud droplets (caused by the microphysics processes such as autoconversion or immersion freezing), which was then provided to the MOSAIC module; added calculation of the grid-resolved precipitation of cloud ice, rain, snow, and graupel at all levels for the wet removal process [*Easter et al*., 2004]; and introduced the size-dependent collection efficiency for the riming process. It should be noted that the MOSAIC and Abdul-Razzak and Ghan parameterization have been coupled with the Morrison scheme in a more recent WRF-Chem version 3.3 [*Yang et al*., 2011]. Since both our study and *Yang et al*. [2011] follow *Chapman et al.* [2009], the coupling is done in a similar manner. We confirm that by performing test runs with WRF-Chem v3.3. Still there exist at least one difference between *Yang et al.* [2011] and our study is that we introduced the size-dependent collection efficiency for the riming process. The riming growth of snow is calculated following *Thompson et al*. [2004], which in WRF-Chem-SMOKE uses the size-dependent collection efficiency between cloud ice/snow and droplet.

In two versions of WRF-Chem-SMOKE (v3.1.1 and v3.3.1), the ice nucleation from smoke particles are treated differently. As shown in Figure 2.2 (a), the Morrison scheme originally includes the parameterizations to treat homogeneous ice nucleation and four "standard" heterogeneous ice nucleation processes (modes). For condensation-freezing and deposition modes, the Cooper curve [*Cooper*, 1986] is used. The immersion-freezing mode is based on *Bigg* [1953]. Contact ice nucleation depends on contact ice nuclei, which is parameterized with temperature dependence following *Meyers et al.*

[1992] and the contact of cloud droplets with IN through Brownian diffusion. It should be noted that these parameterizations of ice nucleation are based on mid-latitude conditions. The freezing rate of the contact mode is proportional to the prognostic CDNC. The freezing rate of immersion mode depends on the ambient temperature and the spectrum of cloud droplets [Eq. A22 in *Reisner et al*., 1998]. Because we replaced the fixed CDNC field with the prognostic CDNC field in WRF-Chem-SMOKE v3.1.1, ice crystal initiation implicitly depends on the 3D smoke field in our study as shown in the schematic diagram Figure 2.2(b).

In WRF-Chem-SMOKE v3.3.1, however, we replace the default setup of temperature-dependent IN parameterizations in the public WRF-Chem with the Phillips parameterization, which explicitly depends on aerosol properties [*Phillips et al*., 2008]. The Phillips parameterization is empirically derived from field measurements of aerosols and IN. The IN activation depends on temperature, supersaturation w.r.t. ice, aerosol species (external mixture of OM, BC, and dust), and the total surface area of aerosol particles with diameter larger than 0.1μm, which is a function of aerosol size distribution. The IN number concentration corresponds to three heterogeneous ice nucleation modes (immersion, condensation freezing, and deposition).

The IN number activated from species X is expressed as:

$$n_{IN,X} = \int_{\log(0.1\mu m)}^{\infty} (1 - \exp[-m_x(D_x, S_i, T)]) \frac{dn_x}{d\log D_x} d\log D_x \qquad (2.14)$$

and

$$m_x = a_X H_X(S_{i,v}, T) x(T) \left(\frac{n_{IN,1,*}(S_{i,v}, T)}{w_{X,1,*}}\right) \cdot \frac{dw_X}{dn_X}, \qquad (2.15)$$

where S_i and T are saturation w.r.t. ice and temperature, respectively, and X corresponds to different species, such as BC, OM, or dust. Here, we only discuss the parameters for BC and OM since dust is not considered in this study. All variables in Eqs. 2.14 and 2.15 with subscript X are species-dependent: μ_x is the average of the number of activated ice embryos per insoluble aerosol particle of size D_X, $n_{IN,1,*}$ is the reference activity spectrum of the average number concentration of IN, which is constructed from field measurements, $dn_x/dlogD_x$ represents the size distribution of BC or OM, Ω_x indicates the surface area of a certain material X, and $d\Omega_x/dn_x \approx \pi(D_X)^2$ according to *Phillips et al.* [2008]. The reference particle surface area $\Omega_{x,1,*}$ equals 2.7×10^{-7} m^2kg^{-1} for BC and $9.1\times10^{-7}m^2kg^{-1}$ for OM. The fraction α_x equals 0.273 for BC and 0.06 for OM. H_x is an empirically defined fraction that represents the scarcity of heterogeneous nucleation of ice in substantially subsaturated conditions. H_{BC} equals H_{OM}, which is a function of temperature and supersaturatation w.r.t. ice. ξ is an empirically derived function of temperature. The differences in $\Omega_{x,1,*}$ and α_x for BC and OM show that BC is a more efficient ice nuclei if all the other conditions are the same.

Several assumptions have to be make in order to employ the Phillips scheme, which might affect the accuracy of IN prediction. First, the Phillips scheme cannot distinguish between different heterogeneous ice nucleation modes. In the immersion-freezing mode, smoke particles initially undergo the CCN activation, forming cloud droplets and then ice crystals, while for the other two modes, ice crystals form directly from interstitial aerosols. We assume that smoke particles in both the interstitial and cloud-borne states are eligible for IN activation. The IN predicted from smoke particles in two states replace both the Cooper scheme and the Bigg scheme in the Morrison

microphysics scheme. Since the percentage of IN undergoing the immersion freezing is unknown, it is impossible to calculate the sink of cloud droplets. As a result, we ignore this sink term.

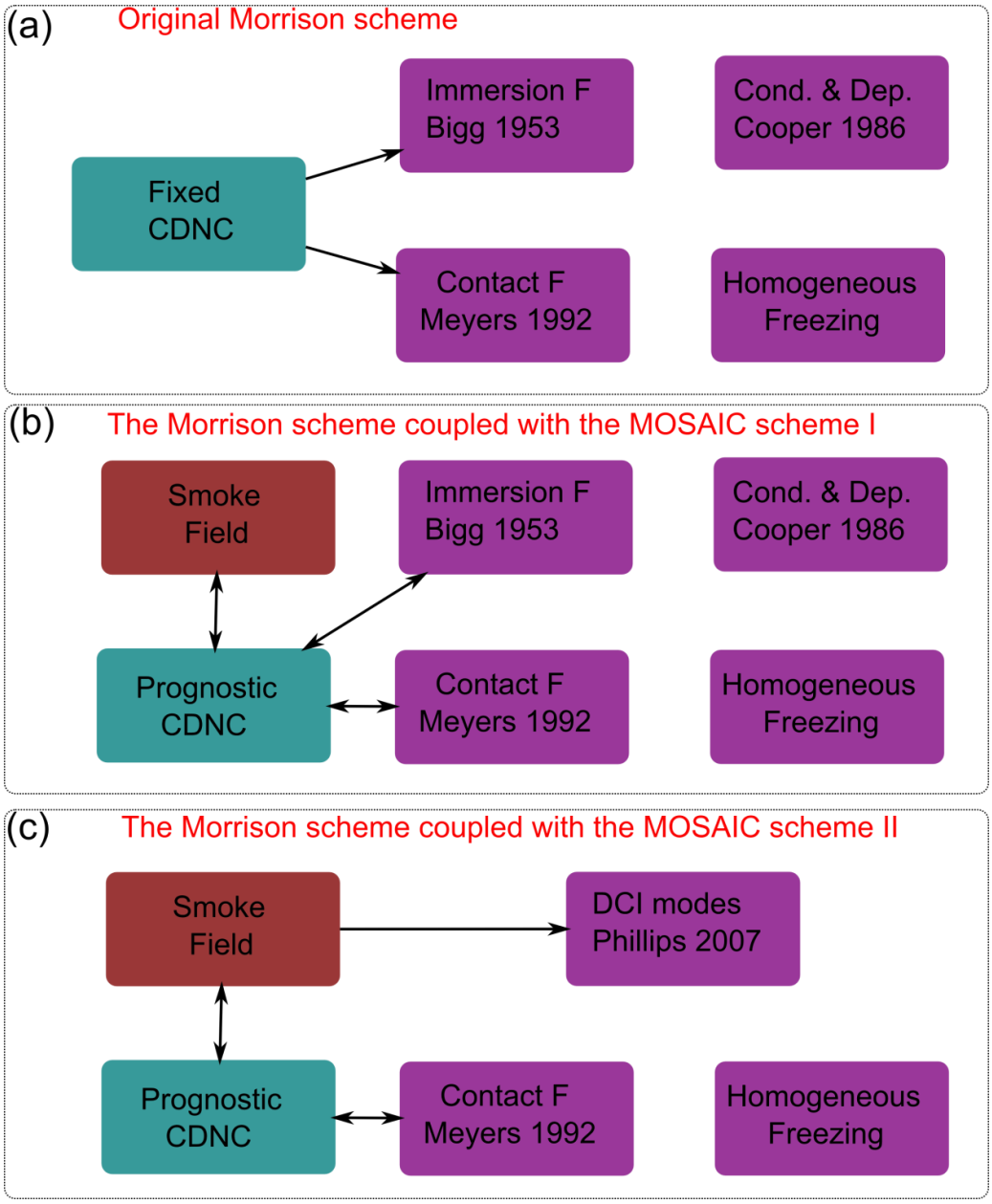

Figure 2.2: Schematic of ice nucleation schemes in (a) the original Morrison scheme; (b) the Morrison scheme in WRF-Chem-SMOKE v3.1.1; (c) the Morrison scheme in WRF-Chem-SMOKE v3.3.1.

Second, the Phillips scheme is designed for insoluble dust, BC, and OM, and implicitly assumes that they are not internally mixed. The MOSAIC aerosol module used in WRF-Chem-SMOKE, however, treats internal aerosol mixtures only. In addition, a number of studies [e.g., *Reid et al*., 2005] have demonstrated that smoke particles are often internally mixed. We assume that an internally-mixed particle becomes IN whenever one component nucleates ice. Examining the parameters in Eqs. 2.14 and 2.15, we find that it is obvious that BC is more efficient in nucleating ice than OM. Hence, we assume that the ice nucleation ability of a smoke particle depends on its BC component only. By multiplying the mean diameter of smoke particles with the cubic roots of BC volume ratios, we calculate the mean diameter of BC core in each size bin as the D_X in Eq. 2.14. Therefore, as shown in Figure 2.2(c), the three heterogeneous ice nucleation modes (immersing-freezing, condensation-freezing, and deposition) are represented by the Phillips scheme, while the contact-freezing mode still depends on prognostic CDNC fields in WRF-Chem-SMOKE v3.3.1.

2.5 Conclusions

The overall structure of the WRF-Chem-SMOKE model is shown in Figure 2.3. WRF-Chem-SMOKE is initiated by the meteorological fields (temperature, wind, and relative humidity, etc.) from reanalysis data and smoke loading and smoke properties (size and chemical composition) from smoke emission models. In this thesis, we develop three original smoke emission models/datasets based on the BA technique + WF_ABBA or MCD45Al products and the FRP technique + MCD14ML product. In addition, to maximize the benefits of each products, we develop an algorithm that integrates the three

original smoke emissions together. The size- and composition-resolved hourly smoke emissions are injected into a certain altitude calculated by a plumerise model and are incorporated into the MOSAIC aerosol scheme in WRF-Chem-SMOKE. The microphysical properties (CCN and IN activations) and optical properties (b_{ext}, ω_0, and g) of smoke particles are further coupled with the microphysics scheme and radiation schemes, respectively. In order to constrain the performance, we compare the modeled smoke field, cloud field, and radiation field against the satellite observations. The multiple products retrieved from different sensors onboard different satellite will be discussed in the following two chapters.

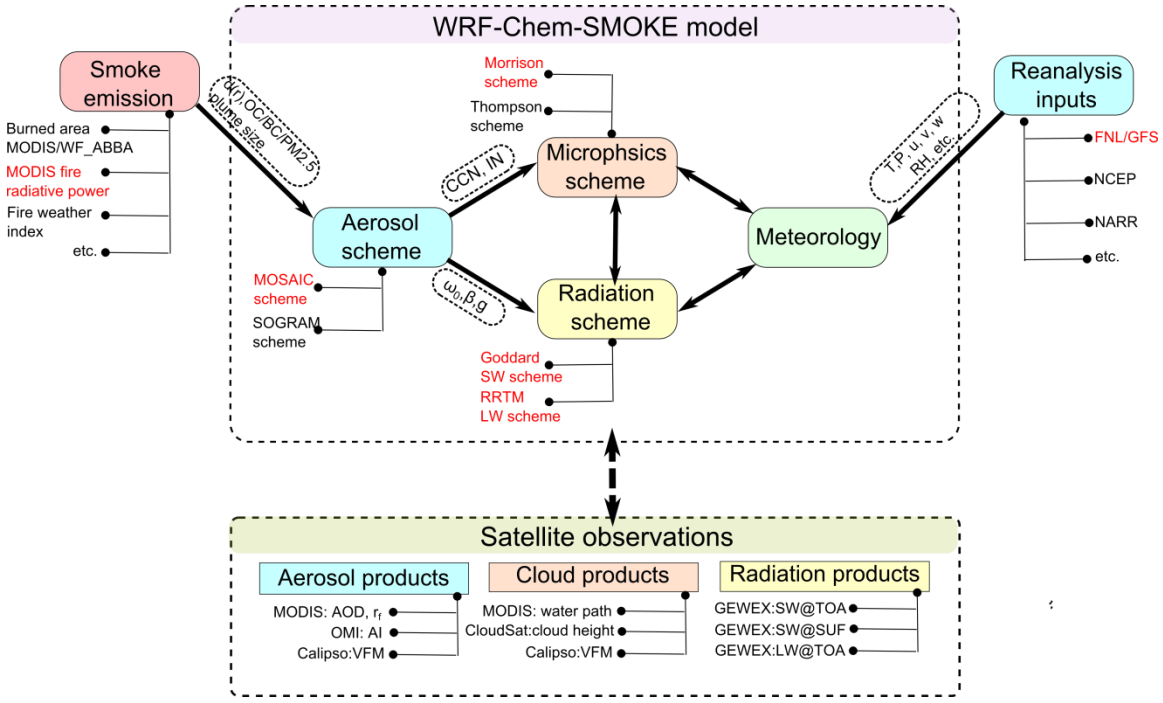

Figure 2.3: Overall structure of the WRF-Chem-SMOKE model

The smoke-cloud coupling, or the coupling between the MOSAIC scheme and the Morrison two-moment microphysics scheme in WRF-Chem-SMOKE is represented in Figure 2.4. The CCN and IN activations explicitly depend on smoke loadings and smoke

properties (size, chemical composition, and mixing state). With more CCN or CDNC, the warm-rain or collision-coalescence process is firstly suppressed (the cloud lifetime effect), which can lead to the production of ice hydrometeors in the deep convective clouds (the thermodynamic effect). In addition, since we introduce a size-dependent riming collection efficiency, more CDNC can also suppress the riming process (the riming indirect effect). Last but not least, more IN activated from smoke particles can promote the formation of ice hydrometeors (the glaciation indirect effect). To sum up, the WRF-Chem-SMOKE model is set up to simulate the complex nature of smoke-cloud interactions in the boreal region as discussed in Chapter 1. Apparently, the effect of smoke on precipitation is complex and non-linear. We will examine the effects of smoke on cloud, radiation, and precipitation in details by performing case studies using WRF-Chem-SMOKE in the following two chapters.

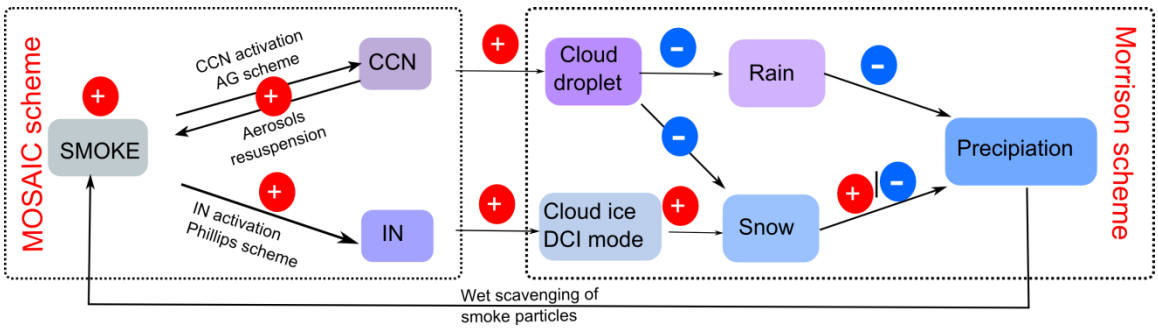

Figure 2.4: Schematic of smoke-cloud coupling in the WRF-Chem-SMOKE model

CHAPTER 3

ANALYSES OF NORTH AMERICAN BOREAL WILDFIRES: THE REALISM OF MODELED SMOKE EMISSIONS AND THE EFFECT OF VARYING AMOUNTS OF SMOKE EMISSIONS ON CLOUD AND PRECIPIATATION

3.1 Introduction

Since the pioneering work of *Seiler and Crutzen* [1980], many smoke emission models based on satellite observations have been developed and employed in studies on the biogeochemistry cycle and carbon-climate feedback [*Randerson et al*., 2006; *van der Werf et al*., 2010], or studies on pollution and its impact on human health [*O'Neil et al*., 2006]. Recently, examining the direct and indirect effects of smoke and the impacts on the local energy budget and hydrological cycle using meso-scale models has drawn considerable attention [*Wang et al*., 2006; *Wu et al*., 2011; *Grell et al*., 2011; *Lu and Sokolik*, 2013b]. Compared to other types of studies, meso-scale modeling studies require smoke emission data with higher spatiotemporal resolutions [*Reid et al*, 2009]. For example, *Wang et al*. [*2006*] shows that, compared to daily smoke emissions, hourly smoke emissions can produce a more realistic representation of the diurnal variation of AODs, which can potentially improve the estimation of the smoke direct effect near the smoke source region in Central America. However, preparing the smoke emissions with high spatiotemporal resolutions, especially for the boreal region, poses significant challenges. For example, the performance of geostationary products, such as WF_ABBA,

is hampered by coarse spatial resolutions over 60°N. Moreover, the hourly smoke innovation frequency in meso-scale modeling [*Reid et al*, 2009] pushes the polar-orbiting products, such as MCD14ML and MCD45Al, to their limits.

The performance of polar-orbiting satellite products has been evaluated by studies that use global chemical transport models (e.g. the Goddard Chemistry Aerosol Radiation and Transport model in [*Petrenko et al.,* 2012]). However, which product, either from a geostationary or polar-orbiting satellite, yields the most realistic smoke emissions in the boreal region is still unknown. In order to compare the performance of different satellite products and smoke emission datasets, we focus on wildfire events in North America, since this region is monitored by multiple satellites and sensors. We are particularly interested in evaluating whether the spatiotemporal resolutions of satellite products suit meso-scale modeling, as well as determining what level of accuracy in smoke emission datasets (e.g. reasonable fire diurnal activity, fire spreading rate) is needed in meso-scale modeling.

In order to determine the radiative and microphysical properties of smoke, quantification of the chemical composition of smoke emissions is necessary. The dominant contribution of organic particulate matter is well recognized, and organic and black carbon are commonly included in biomass burning emission inventories (e.g., *Wiedinmyer et al*. [2011]); however smoke emissions consist of various chemical species that are either directly emitted during a biomass burning event (e.g., primary aerosols) or formed from emitted gaseous precursors (e.g., secondary aerosols). In addition to OC and BC, the presence of inorganic aerosols (such as sulfates and nitrates) even in very fresh

smoke has been demonstrated by modeling studies [*Albarado and Prinn*, 2009] and from observations [*Kondo et al*., 2011, *Pratt et al*., 2011].

Because of the complexity of fire chemistry, modeling studies of smoke-cloud-precipitation interactions have to rely on emission inventories of certain chemical species rather than simulate the fire chemical processes. *Albarado and Prinn* [2009] and other studies argue, however, that by taking emission inventories of primary trace gases and aerosols and injecting them into model grids, models ignore the substantial nonlinear chemical and physical transformations that occur in highly concentrated freshly-emitted smoke, e.g., rapid formation of secondary aerosols such as sulfates or organics. A related problem is that even total particulate mass and PM2.5 (particulate mass for aerosols with diameter < 2.5 μm) in biomass burning emissions remain highly uncertain. *Wu et al*. [2011] multiply OM and BC emissions from 3BEM by a factor of five in their WRF-Chem study of smoke in South America. Several studies that use Fire Locating and Modeling of Burning Emissions (FLAMBE) data, which are also based on WF_ABBA, apply a mass correction factor of 4-6 to emitted PM [*O'Neill et al*., 2006; *Reid et al*., 2009]. Therefore, examining the extent to which varying emission amounts affect 3D smoke loads and smoke-cloud interactions may provide important insights regarding the impact of wildfires on the weather and climate, as well as may help determine accuracy needed in biomass burning emission inventories.

The goal of Chapter 3 is to evaluate the realism of different smoke emission datasets and resulting 3D smoke plumes and examine the effect of varying amounts of smoke emissions on cloud properties and precipitation through an in-depth analysis of boreal wildfires occurring in central and eastern Canada during the summer of 2007. The

study uses the WRF-Chem-SMOKE model, a modified version of the public WRF-Chem (version 3.1.1), in conjunction with A-Train satellite constellation data. Specifically, in Section 3.2, we describe the model configurations and data used in this chapter. In Section 3.3, we examine the spatiotemporal distributions of different smoke emission datasets in several major fire clusters, which are defined as large areas (a group of contiguous model grids, in a spatial scale around 50km) with strong smoke emissions. We try to interpret the differences between the smoke emission datasets using the fire properties retrieved from the MISR plume height project [*Kahn et al*., 2007]. We perform both feature analysis and statistical analysis to validate the modeled smoke AODs against observed AODs at level 2 pixel resolution. Moreover, in Section 3.4, we attempt to quantify the influence of varying emission amounts on 3D smoke aerosol fields along with smoke-induced changes in the cloud droplet number concentration, cloud water path, rain water path, snow water path, total water path, and daily precipitation. We also explore the effect of hygroscopicity by considering smoke composed of organic matter, black carbon, and residual particulate matter, which may have low or high hygroscopicity. The conclusion is summarized in Section 3.5.

3.2 Model Configuration and Data

3.2.1 Description of the 2007 North America Wildfire Event

During 21-24 July 2007, a large widespread wildfire event occurs in central and eastern Canada. This event provides an excellent case study of how smoke aerosols affect the properties of clouds and precipitation because of its extremely high intensity and

dominance over the background aerosol (as determined from MODIS aerosol optical depth).

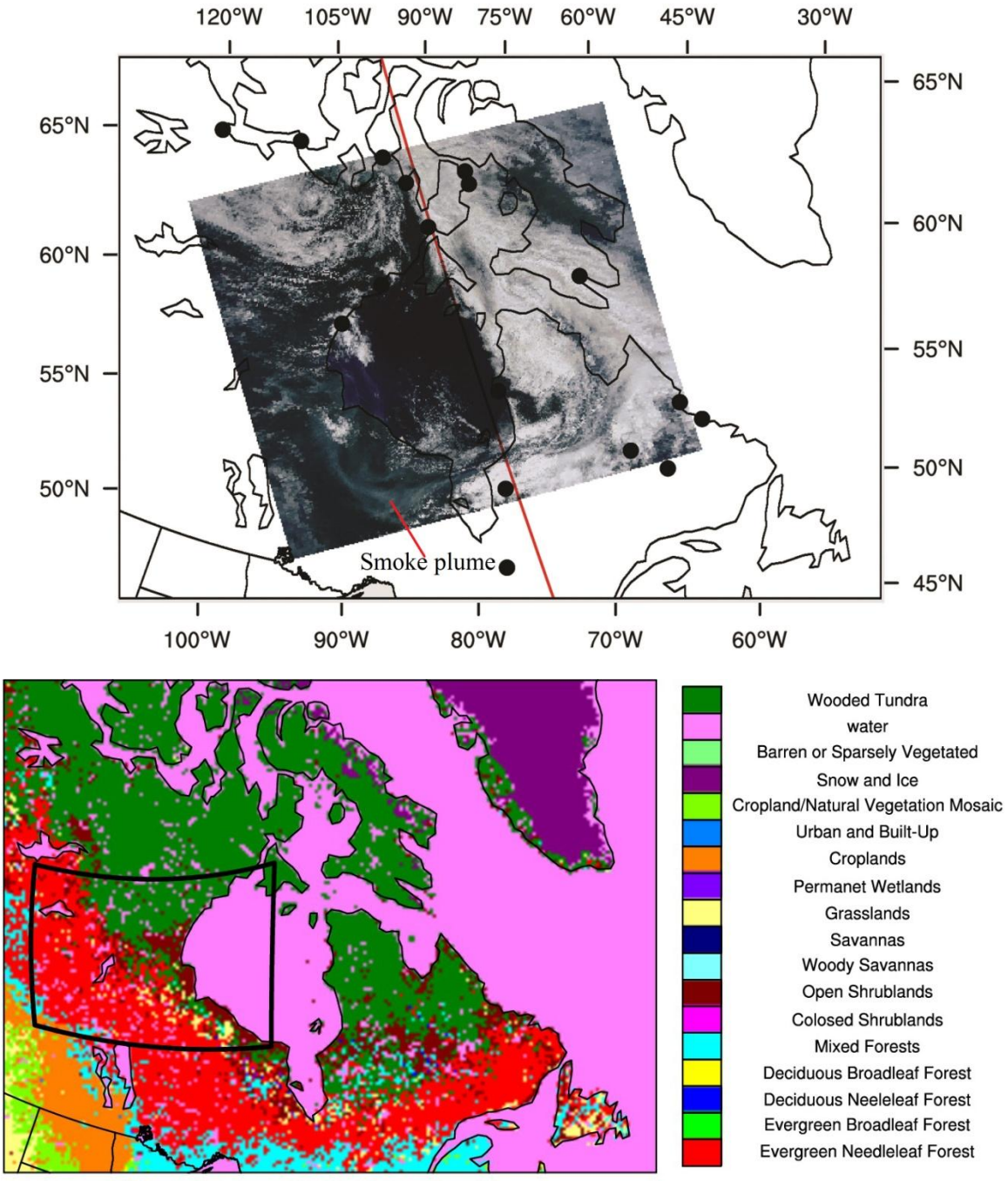

Figure 3.1: (a)WRF simulation domain overlaid by a MODIS true color image (TCI) for 1805-1810 UTC 23 July 2007. The red line indicates the A-Train path. The black dots indicate the precipitation observation stations; (b) simulation domain overlaid by MODIS IGBP vegetation map.

3.2.2 Description of Model Configuration

The WRF-Chem-SMOKE model version 3.1.1 is used in this Chapter. The model has a horizontal resolution of 5 by 5 km, with 842 grids in the east-west direction and 602 grids in the south-north direction, and 36 vertical layers. Figure 3.1(a) and (b) show the study domain, which covers major active fires occurring during the study period, the MODIS true color image on 23 July 2007, and MODIS IGBP-17 category vegetation map. The simulation period is from 20 July 0000UTC to 25 July 0000UTC, 2007, including two-days of model spin-up. The standard model physics packages used in simulations are discussed in Chapter 2.

We use NCEP Global Forecast System (GFS) reanalysis data [*Moorthi et al*., 2001] to provide the boundary and initial meteorological conditions to the model. In order to validate the meteorological fields modeled by WRF-Chem-SMOKE, we obtain the ground-based observations from the Canadian National Climate Data and Information Archive (http://www.climate.weatheroffice.gc.ca/climateData/canada_e.html). For three days of 22, 23, and 24 July 2007, the daily mean records (surface temperature, sea level pressure, and wind speed) of about 300 stations are compared to the WRF model outputs (the SMOKE10 case) of corresponding model grids in scatter plots (Figures 3.2, 3.3, and 3.4). In addition, we perform regression and correlation analyses, the results of which are summarized in Table 3.1. It should be noted that the model outputs are averaged four times a day (0000, 0600, 1200, 1800 UCT), and the daily mean records are derived by averaging at least four times a day (<=24 times). The results show that the model performs very well in terms of simulating the meteorological fields of 22-24 July 2007. Compared to the surface temperature and sea level pressure, the correlation coefficients

between modeled and observed wind speed are relatively low, but the values still pass 0.01% significance test. The reason is obvious since the wind speed is more varying within a day compared to the other two variables.

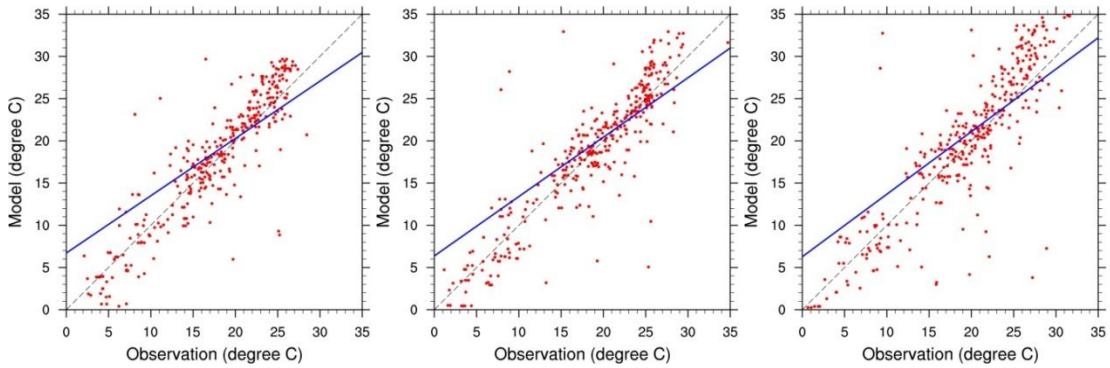

Figure 3.2: The scatter plots for observed and modeled surface temperatures on 22, 23, and 24 July 2007. Blue lines indicate the regression lines.

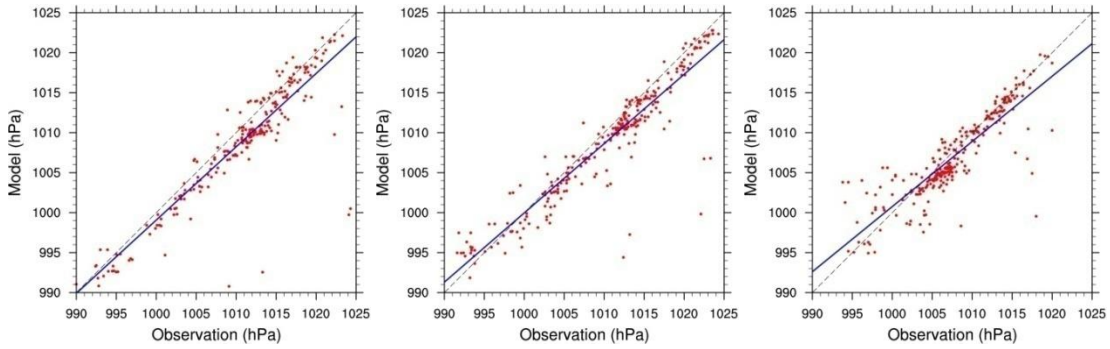

Figure 3.3: The scatter plots for observed and modeled sea level pressure on 22, 23, and 24 July 2007. Blue lines indicate the regression lines.

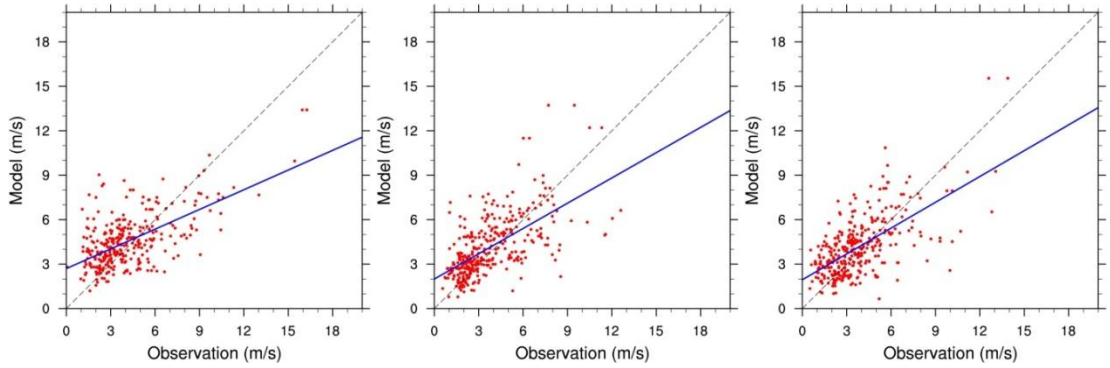

Figure 3.4: The scatter plots for observed and modeled wind speed on 22, 23, and 24 July 2007. Blue lines indicate the regression lines.

Table 3.1: The results of regression and correlation analyses between observations (X) and model outputs (Y) for surface temperature, sea level pressure, and wind speed on 22, 23, and 24 July.

	Slope of regression	Intercept of regression	Correlation coefficient	No. of model grids (stations)
Surface temperature (22 July)	0.68	6.7	0.70	340
Surface temperature (23 July)	0.70	6.4	0.72	356
Surface temperature (24 July)	0.74	6.27	0.70	350
Sea level pressure (22 July)	0.91	82.5	0.92	240
Sea level pressure (23 July)	0.87	133.6	0.93	274
Sea level pressure (24 July)	0.81	185.9	0.87	267
Wind speed (22 July)	0.44	2.7	0.61	328
Wind speed (23 July)	0.57	2.0	0.62	342
Wind speed (24 July)	0.58	1.9	0.64	340

In this Chapter, we design five smoke cases and one clean case. The simulation with the WF_ABBA product and BA technique, which is referred to as the SMOKE1 case, yields very low smoke aerosol loadings, resulting in unrealistically low AODs. Following the approach of *O'Neill et al*. [2006], we gradually increase smoke emissions by a single-digit factor to achieve the best agreement with MODIS AOD fields. The best agreement is found when smoke emission is multiplied by a factor of 10 (referred to as

the ABBA smoke emission dataset by default). The simulation case with the ABBA smoke emission dataset is called SMOKE10. In order to evaluate the performances of different smoke emission datasets/models (Section 3.3), we compare the SMOKE10 case against the FRP case (the simulation with the FRP smoke emission dataset) and the integrated emission case (the simulation case with the integrated smoke emission dataset).

For further analysis of the effect of varying amounts of smoke emissions on cloud properties (Section 3.4), we consider three smoke emission cases: SMOKE1, SMOKE5 (five times of SMOKE1 emission), and SMOKE10. In each case, we perform two sets of runs with low or high hygroscopicity of residual particulate matter, while the hygroscopicity values of OM and BC remain unchanged. The cases with the low hygroscopicity of residual particulate matter are denoted by "LH" (e.g., SMOKE10_LH).

In order to delineate the smoke influence on clouds, we simulate a smoke-free case (called CLEAN). In the CLEAN run we do not model the activation of background aerosols. Instead, we introduce a background CDNC field following the study of *Graf et al*. [2009]. Above 850 hPa (lower altitudes), CDNC is set to 100 no./cm^3, while below this pressure level (higher altitudes), the number concentration is 50 no./cm^3. In the CLEAN run, only the background CDNC field is provided to the Morrison scheme. In smoke-laden conditions, the background CDNC field is added to the prognostic (smoke-activated) CDNC field.

3.2.3 Aerosol and cloud data

In order to constrain the model simulation, we use the aerosol and cloud products from MODIS/Aqua, CALIOP (Cloud-Aerosol Lidar with Orthogonal

Polarization)/CALIPSO (Cloud-Aerosol Lidar and Infrared Pathfinder Satellite Observation) satellite, and MISR plume height project [*Kahn et al*., 2008]. MODIS (Moderate Resolution Imaging Spectroradiometer) onboard the Aqua (EOS PM) satellite covers the entire globe in one to two days, acquiring data in 36 spectral bands from 0.4 μm to 14.4 μm. We use the MODIS Level 2 aerosol optical depth (AOD) at 550 nm from the most recent Collection 5 data set. The spatial resolution of AOD is 10×10 km at the nadir. In addition, we use MODIS Level 2 cloud water path product, which has a 1×1 km resolution at the nadir.

CALIOP measures the vertical profiles of aerosols and clouds. For analysis, we use the vertical feature mask (VFM) product from the most recent version 3.01 data (http://eosweb.larc.nasa.gov/PRODOCS/calipso/table_calipso.html). The vertical and horizontal resolutions of VFM are 30 m and 333 m below 8 km, respectively.

The Multi-angle Imaging SpectroRadiometer (MISR) instrument is on board Terra satellite. MISR acquires multi-angle radiance imagery from a set of nine cameras with viewing angles ranging from -70° to +70°. MISR's multiple view angles allow the retrieval of the heights of smoke plumes above the terrain. In this thesis, we use MISR plume height project [*Nelson et al*., 2008], which calculates the heights and wind speeds associated with smoke plumes.

3.3 Evaluation of Smoke Emission Models

3.3.1 Comparison of Smoke Emission Datasets

3.3.1.1 Comparison of the Spatiotemporal Distributions of Smoke Emissions

Figure 3.5 shows a portion of the modeling domain, which contains the major active fires from 20 to 24 July 2007. This sub-domain, as labeled by the black box in Figure 3.1(b), is located around the southwestern shore of Hudson Bay. The various colored dots in Figure 3.5 represent the model grids with different smoke emission datasets (red: FRP, green: ABBA, blue: MCD45, black: the integrated dataset). However, since the spatial extent of the sub-domain is too large as compared to each individual fire cluster, it is impossible to compare the spatial distribution of different smoke emission datasets in Figure 3.5. Therefore, we zoom in on several boxes (box1-6 as labeled in Figure 3.5) in which the major fire clusters occurred. The smoke emissions in these 6 boxes account for about 77% of total smoke emissions (based on the FRP dataset).

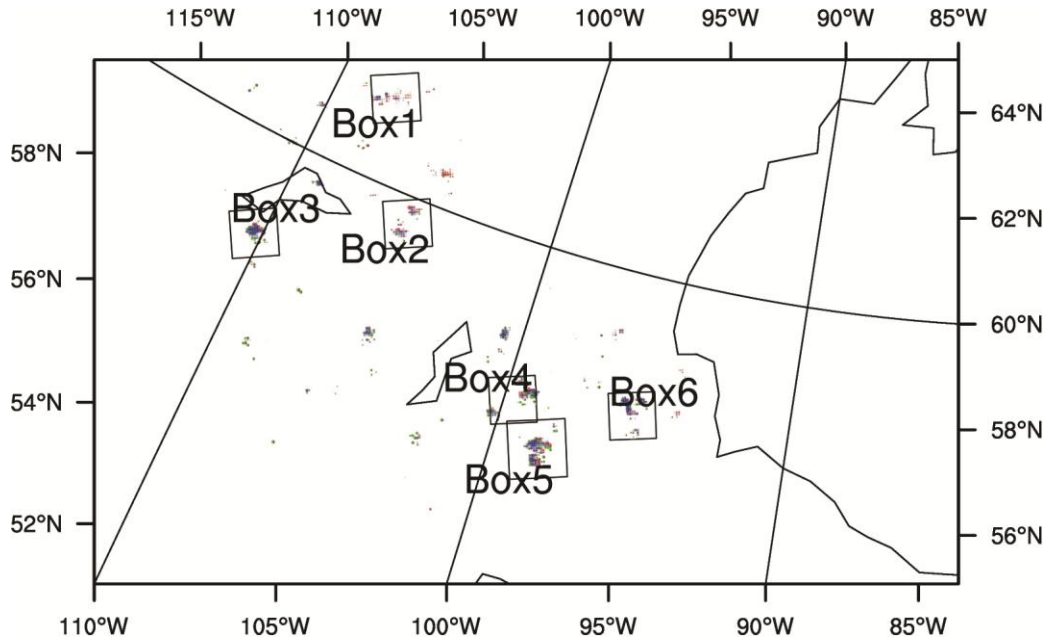

Figure 3.5: The sub-domain that contains the major active fires. In the boxes are the major fire clusters.

We integrate the gridded hourly smoke emissions over time (space) to demonstrate the spatial (temporal) distribution of smoke emission in Figure 3.6. As shown in Figures 3.6(a, c, e, g, i, and k), we employ pie chart plots over maps to represent the smoke

emissions of the three original datasets and the integrated dataset in each box. For each model grid in a box, we sum the gridded hourly smoke emissions of four datasets from 20 to 24 July 2007 to yield gridded total smoke emissions of the four datasets. The ratios between these four values are represented by the percentage of four different colors in the pie chart (red: FRP, green: ABBA, blue: MCD45, black: the integrated emission), while the size of the pie chart indicates the value of the integrated emission dataset. At the bottom of Figure 3.6(a) are example pie charts with varying sizes, which correspond to different emission amounts. As shown in Figures 3.6(b, d, f, h, j, and l), we plot the time series of the box-integrated hourly smoke emissions of four datasets (red: FRP, green: ABBA, blue: MCD45, black: the integrated dataset), which are defined as the sum of all gridded hourly smoke emissions within a box at a certain time step. The values of box-integrated daily smoke emissions are also labeled in these figures.

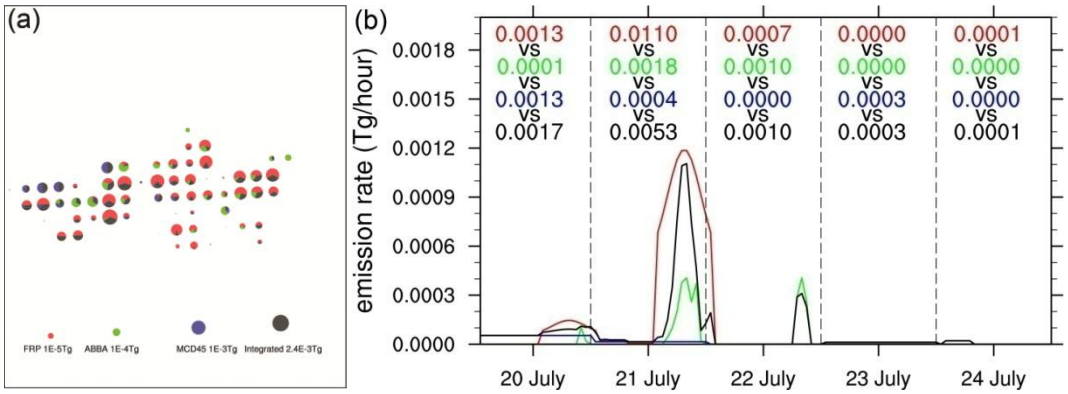

Figure 3.6: The spatial and temporal distributions of four smoke emission datasets in boxes 1-6 as labeled in Figure 3.5. The figures with the pie charts show the gridded total smoke emissions of four datasets. The figures with the x-y plots show the time series of box-integrated hourly smoke emissions of four datasets.

As shown in Figure 3.5, the largest fire cluster north of 60°N resides in box 1. According to Figures 3.6(a) and 3.6(b), the MCD14A1 product detects active fires distributed in several model grids during the daytime of 21 July 2007 in box 1. The box-

integrated daily smoke emission amount of the FRP dataset on 21 July 2007 is 0.011Tg. In contrast, both the spatial coverage (number of model grids) and the total amounts of ABBA and MCD45 emissions in box1 are smaller compared to FRP emissions. For example, during the three days of 20-22 July, the ABBA dataset predicts several active fires with durations less than 12 hours. The total box-integrated ABBA smoke emission amount is around 0.0033Tg. The MCD45 dataset predicts smoke emissions on 20 July in four model grids near the northwest corner of the fire cluster, where both the FRP and ABBA datasets do not detect any active fires. This difference between MCD14 and the other two original datasets may be due to smoke particles being deposited on the ground and thus reducing surface reflectance as the smoke plumes are transported to the north. As for the integrated dataset, we find that the most noticeable "improvement" or change is that the fire durations in the FRP dataset are adjusted according to the ABBA dataset. The box-integrated daily smoke emission amount of the integrated dataset on 21 July is 0.0054Tg, which is about the half of the value of the FRP dataset.

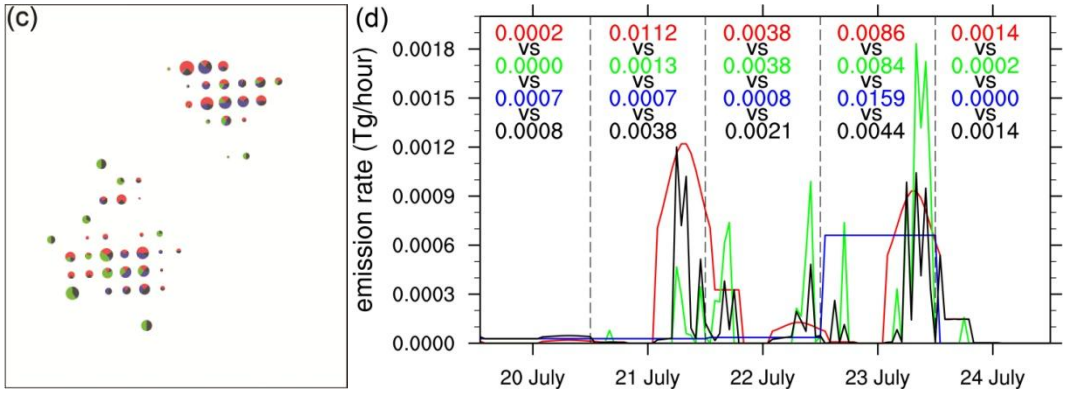

Figure 3.6: continued

The spatiotemporal distributions of the smoke emissions in box2 are shown in Figures 3.6(c) and 3.6(d). Box 2 contains two fire clusters located near 60°N. Similar to box 1, the box-integrated daily smoke emissions of the FRP dataset are much larger

compared to the other three datasets on 21 July, very likely due to the unreasonable assumption of a long fire duration of 12 hours. With the fire duration adjusted, in box 2 on 21 July the box-integrated daily smoke emissions of the integrated dataset are about one third of the FRP smoke emissions and three times that of ABBA smoke emissions. On 23 July, the box-integrated daily smoke emissions of the FRP and ABBA datasets are close to each other and about the half of those of the MCD45 dataset as shown in Figure 3.6(d); however, the MCD45 dataset does not significantly contribute to the integrated dataset due to the fact that FRP and MCD45 smoke emissions appear in almost the same model grids on the same day as shown in Figure 3.6(c) (only the FRP dataset contributes to the integrated dataset in this circumstance). As a result, the integrated smoke emissions have fire durations similar to the ABBA dataset but magnitudes similar to the FRP dataset on 23 July. The box-integrated daily smoke emission amount of the integrated dataset (0.0044Tg) is about half of those of the FRP and ABBA datasets (0.0086 and 0.0084Tg) as shown in Figure 3.6(d).

An interesting pattern of smoke emissions in box 2 is noteworthy: In the outer rings of the fire clusters only ABBA smoke emissions exist, some of which contribute to the integrated smoke emissions. Also apparent in boxes 3, 4, 5, and 6, this pattern of smoke emissions may be due to 1) the unique capability of the WF_ABBA product in tracking the wildfires as they spread to different regions; or 2) active fires in the WF_ABBA product being interpolated to nearby model grids because of the coarse spatial resolution, which is larger than the resolution of the model grid.

The spatiotemporal distributions of smoke emissions in box 3 are shown in Figures 3.6(e) and 3.6(f). As shown in the pie chart map of Figure 3.6(e), in the middle of the fire

cluster exist large amounts of MCD45 smoke emissions, relatively smaller amounts of ABBA smoke emissions, but very small or no FRP smoke emissions. In addition, Figure 3.6(f) shows that the box-integrated smoke emission amount of the FRP dataset in box 3 is significantly smaller compared to that of the MCD45 dataset on 22 and 23 July (0.0114 vs. 0.0323Tg). Therefore, unlike the integrated emissions in boxes 1 and 2, the integrated emissions in box 3 are mainly built on the MCD45 smoke emissions (step 2 as discussed in Chapter 2), while the diurnal cycles of the fire activities in these model grids completely follow the ABBA dataset in the same model grid or surrounding 8 grids.

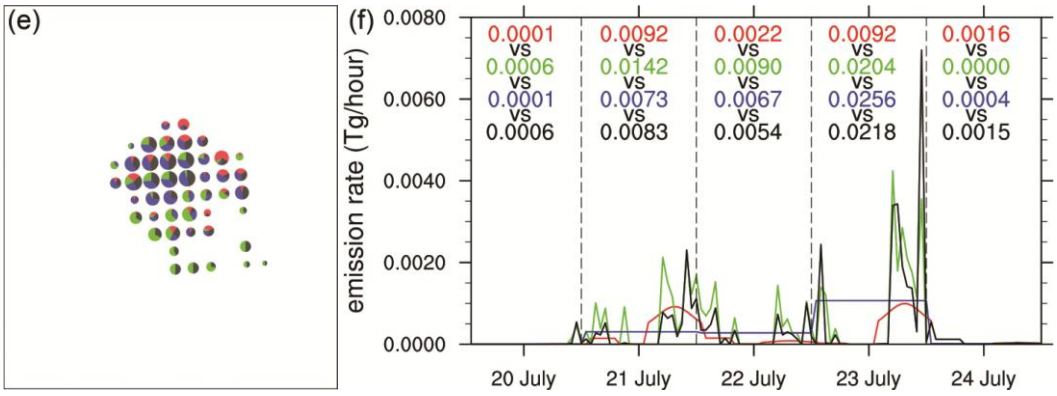

Figure 3.6: continued

As shown in Figure 3.6(g), box 4 contains one small and one large fire cluster. In the larger one, we find that the spatial distributions of the three original smoke emission datasets do not agree with each other. For example, the ABBA smoke emissions mainly reside in the lower portion of the large fire cluster, whereas in the upper right and upper left portions of the large fire cluster exist more MCD45 and FRP smoke emissions, respectively. By examining Figure 3.6(h), we find that the three original datasets produce a large amount of smoke on 23 and 24 July. On 23 July, the box-integrated daily smoke emissions of the FRP and ABBA datasets are about 2 and 1.7 times that of the MCD45

dataset (0.02Tg and 0.0188Tg versus 0.0108Tg). During the second nighttime period of 24 July (0200-0800LST), the ABBA dataset produces enormous amounts of smoke emissions, which leads to larger box-integrated daily smoke emissions as compared to the FRP andMCD45 emissions on 24 July (0.195Tg versus 0.119Tg and 0.119Tg). Although the integrated dataset in box 4 is built primarily on the FRP dataset with adjusted fire duration, the MCD45 dataset also contributes to the integrated smoke emissions on 21 July and 23 July (not shown).

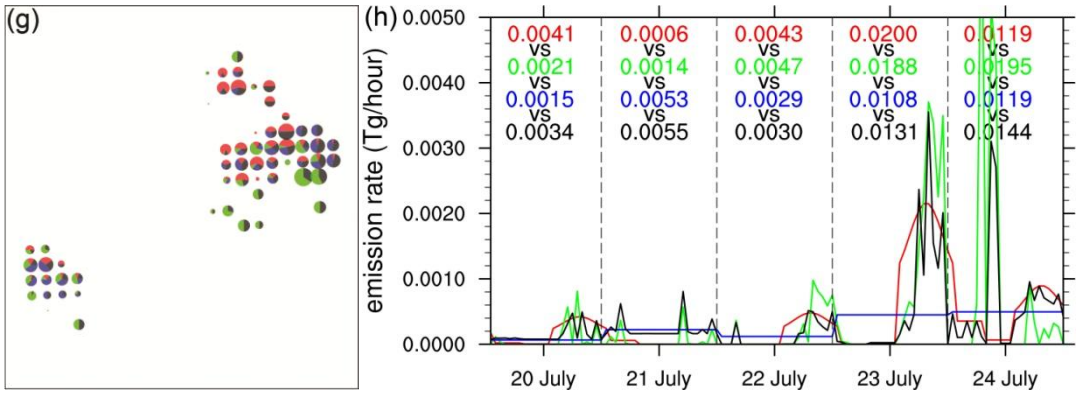

Figure 3.6: continued

Box 5 is located close to box 4, and contains the fire cluster with the largest box-integrated total smoke emissions (based on all three original datasets) as compared to the other boxes during the study period. Similar to the other boxes (except box 1), many model grids in the outer ring of the fire cluster have only ABBA smoke emissions as shown in Figure 3.6(i). In the upper left portion of the fire cluster, the amount of the MCD45 smoke emissions is much larger compared to the very small amount of the FRP smoke emissions. Meanwhile, large amounts of the FRP smoke emissions and relatively smaller amounts of the MCD45 smoke emissions are predicted in the upper right portion of the fire cluster. It should be noted that, if the DOB adjustment is not performed,

MCD45 smoke emissions would not exist in the upper right portion of the fire cluster. Consequently, the integrated smoke emissions on the upper left and right portions of the fire cluster are mainly based on the MCD45 and FRP datasets, respectively. As shown in Figure 3.6(j), the FRP dataset produces very strong box-integrated daily smoke emissions on 23 July (0.0399Tg), which are about 1.4 times the ABBA smoke emissions and twice the MCD45 smoke emissions. Compared to the FRP dataset, the integrated dataset produces an approximately 40% smaller amount of smoke emissions on 23 July, mainly due to adjusted fire durations.

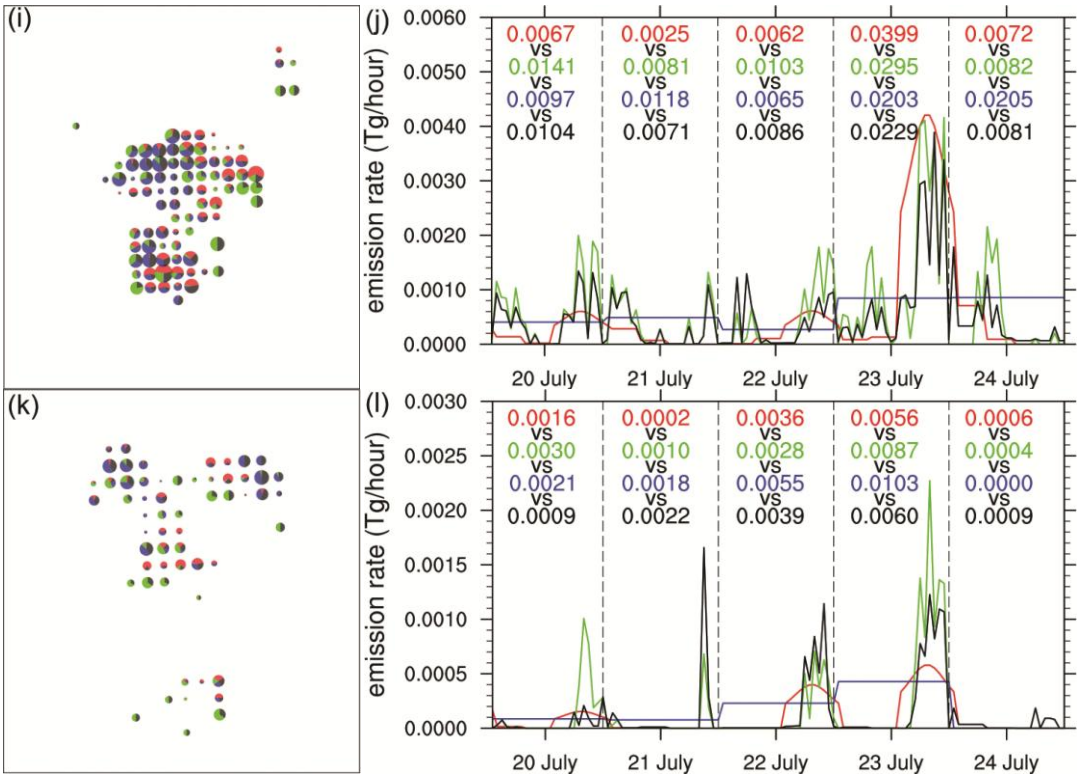

Figure 3.6: continued

As shown in Figures 3.6(k) and 3.6(l), box 6 contains more MCD45 smoke emissions than FRP and ABBA smoke emissions, especially from 21 to 23 July. Similar to box3, the daily MCD45 smoke emissions are partitioned to the diurnal cycles of fire

activities following the ABBA dataset, and become the main component of integrated smoke emissions.

3.3.1.2 Examining the Correction Factor Used in the ABBA Dataset

As discussed in Section 3.2.2, we find a multiplying factor of 10 is needed for the smoke emissions derived from the BA technique and the WF_ABBA product to match the MODIS AOD observations (as shown in Section 3.3.2).

Our finding of low smoke emissions agrees with past studies, which use FLAMBE emission estimates which are also based on the WF_ABBA fire products [*Wang et al*., 2006; *O'Neill et al*., 2006; *Reid et al*., 2009]. *Reid et al.* [2009] showed that smoke emissions estimates for wildfires that occurred in Alaska in 2004-2005 were low by a factor of 4. For a wildfire in Quebec in 2002, *O'Neill et al*. [2006] showed that FLAMBE underestimated smoke emissions by a factor of 6. Their studies suggest that the underestimation is most likely the result of the low emission factor used in FLAMBE. However, we find that the emission factor for PM2.5 in *O'Neill et al*. [2006] (40 g/kg C for Temperate/Boreal-Low) is actually higher than that used by most other studies. For instance, it is higher than the value used in the FLAMBE latest version [*Reid et al.*, 2009] (32 g/kg C for Temperate/Boreal-Low). The values of EFs for PM2.5 used in other studies are 25.5 g/kg C (the "Extratropical Forest" category in *Andreae and Merlet* [2001]), 25.2 g/kg C (the "Extratropical Forest" category in *van der Werf et al.* [2010]), 30.6 g/kg C (the "Boreal Forest" category in *Akagi et al.* [2011]), 25.5 g/kg C (the "Evergreen Needleleaf Forest" category in *Wiedinmyer et al.* [2011]), and 12.9 g/kg C (BC+OC only, the "Tree Cover needle-leaved evergreen" category in *Petrenko et al.* [2012]). It should be noted that the above studies use g/kg dry mass burned as the unit for

EF, so we have to convert the unit to g/kg carbon by assuming a mass fraction of carbon (0.51, "Temperate/Boreal-Low" category, Table II in *Reid et al.* [2009]). Although *Reid et al.* [2005] suggest that the emission factors of large fire events can be much higher than commonly accepted values, we think that the variation in the emission factor itself cannot explain low smoke emission by a factor of 5-10.

Another possible source of low emissions is biases in estimates of the sub-pixel fire size in WF_ABBA. Studies [e.g., *Reid et al*., 2009] suggest that over high latitudes WF_ABBA products tend to underestimate the burned area more compared to other geographical regions. In addition, using instantaneous observational snapshots (instantaneous fire size) to characterize the continuous variable smoke emission process (burned area) poses a significant challenge [*Ichoku et al*., 2012]. For example, if WF_ABBA reports two active fires in the same pixel within 15 minutes, it may be the same fire burning over this location for 15 minutes, or another type of fire that quickly propagates to a different location but still within the same 6 km × 8 km pixel. In our study, we assume the former situation and a fire lifetime of one hour. However, if it is the latter situation, even summing all instantaneous fire size may not be adequate. We find that omitting temporal filtering leads to an increase in emission fluxes by a factor of 1.5 only. Therefore, like previous studies, our study confirms that smoke emissions computed with WF_ABBA need to be corrected before they can be used in meso-scale models.

In addition, we prove that this correction factor is necessary by comparing the ABBA smoke emissions (10 times the original smoke emissions derived from the WF_ABBA products) against the smoke emissions derived from other satellite products and techniques. For the fire clusters above or very close to 60°N (box 1 and box2), the

FRP smoke emissions on 21 July are 6-8 times larger than the ABBA smoke emissions, although the FRP smoke emissions in boxes 1 and 2 on 23 July are very likely overestimated because of unrealistic assumption of fire duration. For other fire clusters, the ABBA and FRP datasets are comparable on a daily basis. Furthermore, we take the box-integrated daily MCD45 smoke emissions as benchmarks, compare them with one tenth of the box-integrated daily ABBA smoke emissions, and calculate the ratios between these two values for each box. The results show that the ratios vary significantly from one fire cluster or one day to another (for example, the ratios equal 2.2 (box 1, 21 July), 5.4 (box 2, 21 July), 18.9 (box 2, 23 July), 12.5 (box3, 23 July), 5.7 (box 4, 23 July), 6.8 (box5, 23 July), and 11.8 (box 6, 23 July)).Since the values of α, β, and EF in the two datasets are the same, these ratios basically demonstrate the underestimation of the burned areas in the ABBA dataset. Therefore, the underestimation of burned areas in the ABBA dataset is mainly caused by the underestimation of the propagation speed of the fire front in WF_ABBA in cases of extreme wildfire.

3.3.1.3 Examining the effect of the fire characteristics

We find that, even in one wildfire event, the differences in spatiotemporal distributions of FRP, ABBA, and MCD45 smoke emissions vary from one fire cluster to another, and these inconsistent differences may be due to various fire characteristics. In order to support our reasoning here, we also analyze the results from the MISR plume height project in Figure 3.7. Several smoke plumes recorded in the MISR plume height project actually originated from several fire clusters discussed above. In Table 3.2, we list the names of a total of 7 smoke plumes, as well as the dates of detection, the boxes in which the active fires occurred, wind speeds of the "first point" across and along the

smoke plumes, and the median heights of the smoke plumes. The "first point" here refers to the point of the smoke plume that is located closest to the corresponding active fire. If the wind speeds for the first point are not available, we select the wind speeds of the second, or third closest points, or so on and so forth.

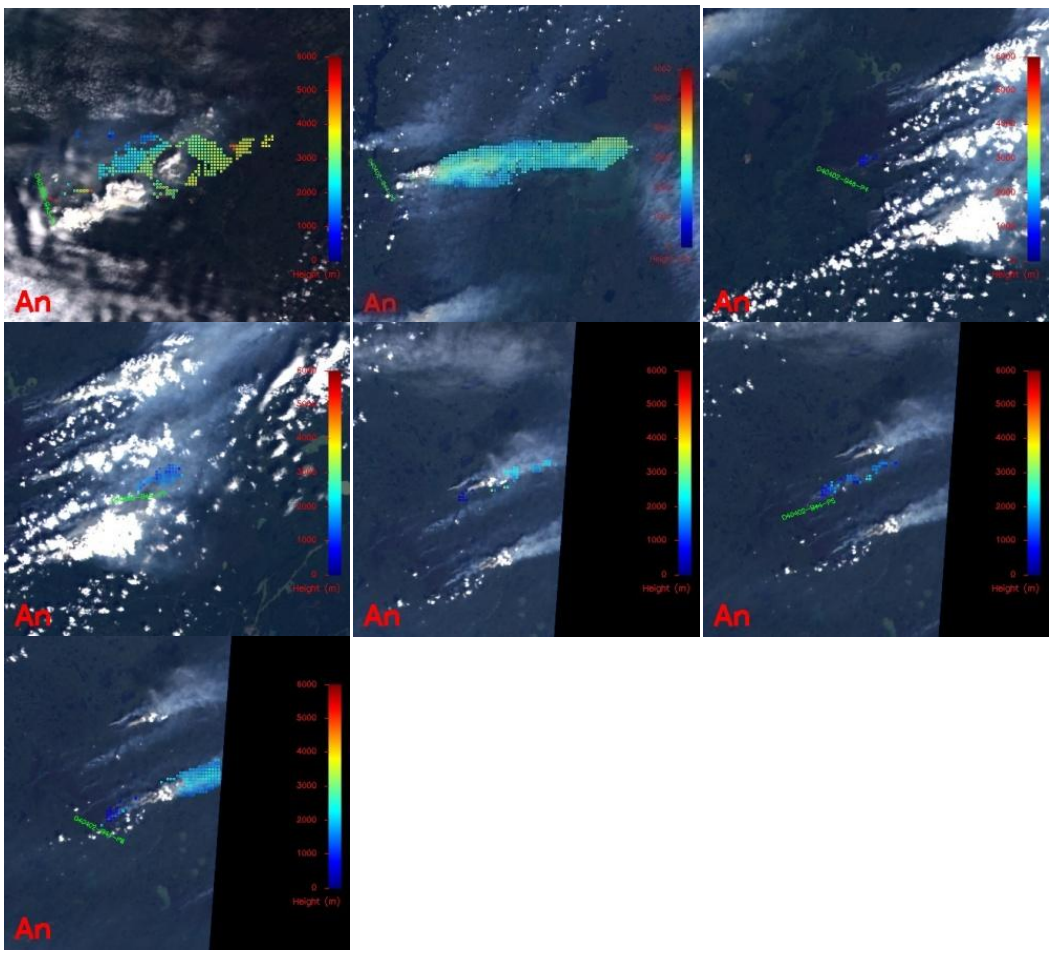

Figure 3.7: The MISR true color images of the smoke plumes as listed in Table 3.2. The pixels and the colorbars indicate the heights of the smoke plumes. Figures are generated by the MISR plume height project

Unfortunately, the smoke plumes originating from the fires in boxes 1 and 2 were not detected by the MISR sensor. Based on the discussion above, we know that the FRP dataset produces more smoke emissions than the ABBA dataset in box 1 and box 2 on 21

July. This fact may indicate that the fires burned intensively with high FRP values but were quickly extinguished, because of the relatively short fire duration according to the ABBA dataset.

Table 3.2: The list of MISR smoke plumes examined in our study and their properties.

MISR smoke plume	Date of detection	Box	Wind speed of first point (cross, m/s)	Wind speed of first point (along, m/s)	Median plume height (m)
O40388-B43-P1	July 22	Box3	10.5	4	3110
O40402-B44-P9	July 23	Box4	-1.3	-0.2	2429
O40402-B45-P4	July 23	Box5	0.4	0.2	748
O40402-B45-P7	July 23	Box5	13.5	12.5	1489
O40402-B44-P3	July 23	Box6	5.7	2.2	2041
O40402-B44-P5	July 23	Box6	-1	-0.5	1320
O40402-B44-P6	July 23	Box6	7.5	4.4	1829

In box 3, the MCD45 dataset produces significantly more smoke emissions than the FRP dataset, indicating that many active fires are missed by the MCD14A1 product. The true color image of the smoke plume associated with the active fires in box 3 on 22 July is shown in Figure 3.7(a). Both Figure 3.7(a) and the height of this smoke plume listed in Table 3.2 prove that these active fires were actually in the flaming phase, and triggered strong pyro-convections, which in turn blocked the detection of the active fires by MODIS. Similarly, by studying one of the two smoke plumes associated with active fires in box 4, we find that the active fires in box 4 also induced strong pyro-convections and consequently strong smoke plumes as shown in Figure 3.7(b). As the smoke plume travels further downwind to the east, it may very likely block active fire detection by

MODIS, or deposit a large amount of smoke on the ground and thus decrease the surface reflectance. Either of these two effects of the smoke plume can explain the fact that the MCD45 dataset produces more smoke emissions in the upper right portion of the fire cluster as shown in Figure 3.6(g); however, if the latter effect occurs, the smoke emissions by the MCD45 dataset are actually overestimated in this region.

As discussed above, the MCD45 and FRP smoke emissions dominate in the upper left and right portions of the fire cluster in box 5, respectively. In order to explain this pattern according to the fire characteristics in box 5, we examine two smoke plumes (O40402-B45-P4 and O40402-B45-P7 as shown in Figures 3.7(c) and 3.7(d)), which originated from the active fires in the upper left and right portions of the fire cluster in box 5, respectively. The median height of the smoke plume O40402-B45-P4 is very low, about 750m above the ground, which indicates that some fires in the upper left portion of the fire cluster are very likely in the smoldering phase. In contrast, the smoke plume O40402-B45-P7 is injected to an altitude of 1489m, which indicates the flaming phase of burning. It should be noted that the retrieved wind speeds associated with the plume O40402-B45-P7 are larger than 10m/s. If not for the strong wind speed, the plume would be injected to an even higher altitude [*Freitas et al*., 2010]. By examining the modeled meteorological conditions (not shown), we find that the strong winds are actually induced by the over-passing cold frontal system; therefore, the wind speeds at the surface should be large also. Based on all the information discussed above, we speculate that, in the upper portion of the fire cluster in box 5, the wind-driven fire front is composed of many active fires in the flaming phase, which burn intensively and propagate very quickly from west (upper left) to east (upper right), leaving fires in the smoldering phase and resulting

in burn scars in the upper left portion of the fire cluster. This also explains why the ABBA dataset captures the active fires in both the upper right and upper left portions of the fire cluster, as it has longer temporal coverage.

Three smoke plumes associated with the active fires in box 6 were observed by MISR. Two smoke plumes (O40402-B44-P3 and O40402-B44-P6) are very similar in nature, for example with regard to the high plume height (~1900-2000m) and relatively strong retrieved wind speed (~6 m/s). Similar to box 3, the MCD45 dataset generates more smoke emissions than the other two datasets in box 6; however, the higher MCD45 smoke emissions are not due to pyro-convections (like in box 3) as shown in Figure 3.7(e). One possible explanation for higher MCD45 smoke emissions is that the active fires may burn for a long time, propagate very fast, and scorch a large area.

3.3.2 Validation of Modeled Smoke Plumes

In this section, we incorporate the ABBA, the FRP, and the integrated smoke emission datasets into the WRF-Chem-SMOKE model version 3.1.1 and compare modeled smoke AOD against the MODIS AOD fields (10 km×10 km, level 2, and collection 5). Level 2 MODIS AOD fields at 1710-1900 UTC on 22 July, 1800-1815 UTC on 23 July, 1900-1910 UTC on 24 July are shown in the first column of Figure 3.8. In the next three columns of Figure 3.8 are AOD fields modeled by the SMOKE10 case (the one with the ABBA smoke emissions), the FRP case, and the integrated emission case at 1800 UTC on 22, 23, and 24 July.

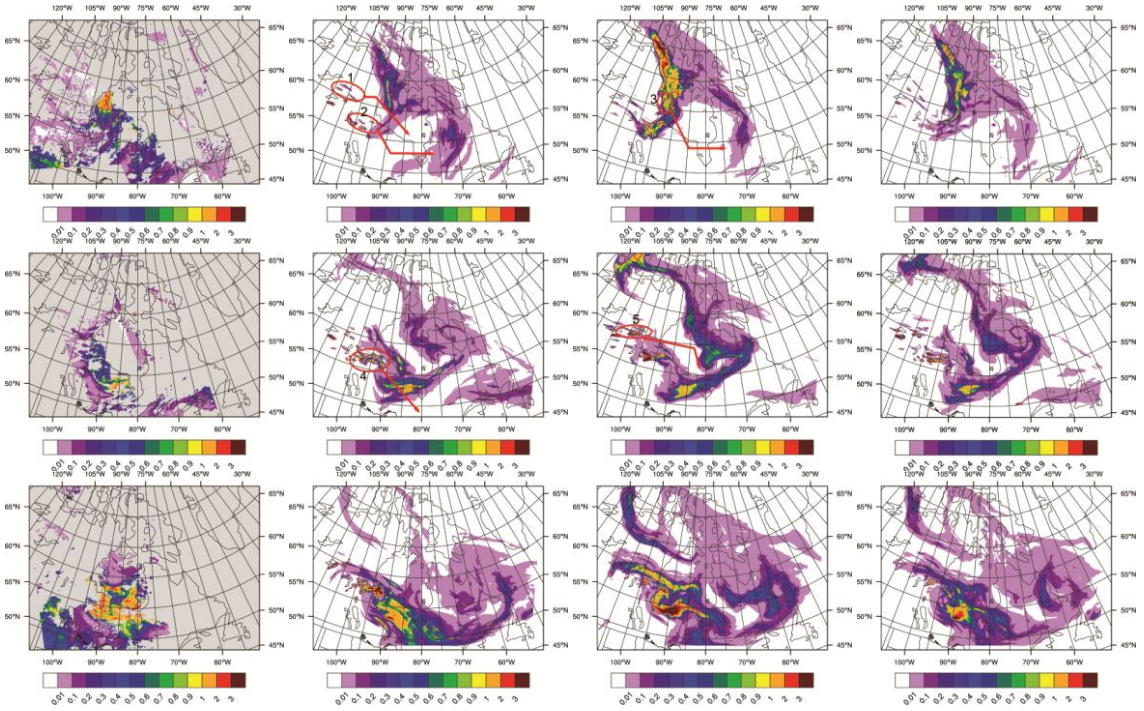

Figure 3.8: Observed and modeled AOD fields. The first column shows the MODIS level 2 collection 5 AOD fields around 1800UTC (± 1 hour time difference) from 22 July to 24 July, 2007. The next three columns show the AOD fields from 22 July to 24 July at 1800UTC modeled by the SMOKE10, the FRP, the integrated cases, respectively.

In addition, we conduct several statistical analyses: for each MODIS AOD pixel (resolution: 10 km×10 km) within an area that contains strong smoke plumes (for 22 July: 58°~65°N, 95°~85°W; for 23 July: 50°~62°N, 95°~80°W; for 24 July: 50°~60°N, 95°~78°W) we search for the corresponding 2×2 model grids (model grid resolution: 5 km×5 km) and calculate the average values of modeled AODs in these four model grids. For 22, 23, and 24 July, we collect 1364, 2587, 6452 pairs of MODIS and modeled AODs. Based on these values, we construct correlation, root-mean-square difference (RMSD) analyses between the MODIS and modeled AODs for three cases and three days in Table 3.3. We also compare the averaged values of MODIS and modeled AODs. The performance of modeling cases is scored by the Taylor skill metric as following:

$$S = \frac{2 \cdot (1+\rho)}{(\sigma_{norm} + 1/\sigma_{norm})^2}, \qquad (3.1)$$

where S is the Taylor skill metric, ρ is the correlation coefficient, σ_{norm} is the ratio of modeled to observed (MODIS) standard deviation [*Taylor*, 2001].

On 22 July, according to the MODIS AOD field shown in Figure 3.8(a), a relatively strong smoke plume, with a maximum MODIS AOD of around 2.4, is located around 58°~63°N, 95°~90°W. Both SMOKE10 and FRP cases (Figure 3.8(b) and 3.8(c)) capture this smoke plume; however, the SMOKE10 case significantly underestimates the magnitude and the horizontal extent of smoke AODs in this region. For example, as shown in Table 3.3, the averaged MODIS AOD in this region is as high as 0.85, while the averaged AOD modeled by the SMOKE10 case is only 0.18. Even if we consider a background AOD, say with a value of 0.1, the modeled AOD is still only one third of the MODIS AOD in this region. As shown in Figure 3.8(c), the magnitude of AODs modeled by the FRP case are very close to the MODIS AODs, whereas the horizontal extent is also underestimated similar to the SMOKE10 case. As a result, the averaged AOD of 0.54 (plus a background AOD, of say 0.1) modeled by the FRP case is closer to observations (0.85) than the SMOKE10 case. In contrast, the SMOKE10 case yields a better correlation coefficient than the FRP case as shown in Table 3.3 (0.603 versus 0.365). This is due to the fact that the SMOKE10 case successfully predicts the portion of the smoke plume with the highest AOD values at around 90°W. As shown in Figure 3.8(d) and Table 3.3, the integrated emission case produces more reasonable smoke AODs than the SMOKE10 case and yields better spatial distribution for the smoke plume (higher correlation coefficient) than the FRP case. The magnitude and the horizontal extent of the

AOD field, the averaged AOD value, RMSD, correlation coefficient, and Taylor skill metric in the integrated emission case are between the values of the other two cases at 1800UTC on 22 July. Due to the presence of cloud decks, the portion of the smoke plume above 63°N is not retrieved by MODIS; however, comparing Figures 3.8(b) and 3.8(c), we find that the SMOKE10 and FRP cases significantly differ from each other in this region, especially around 70°N. The differences in modeled AODs between these two cases on 22 July are mainly due to the large differences between the ABBA and FRP smoke emissions in box 1 and box 2 on 21 July, as shown in Figures 3.6(b) and 3.6(d), respectively.

In Figure 3.8, we also include several labeled red circles and arrows pertaining to the modeled smoke AOD fields, which highlight several interesting features and their approximate transport routes for the next day. In the SMOKE10 case as shown in Figure 3.8(b), several streaks of smoke plumes in circle 1 actually originate from the smoke emissions in or near box 1 on 22 July. Compared to the SMOKE10 case, the integrated emission case produces a slightly smaller amount of smoke emissions, while the FRP case barely produces any smoke plumes in the same region. These differences in smoke plumes can be explained by the differences between the ABBA and FRP smoke emissions in box 1 on 22 July as shown in Figure 3.6(b). The smoke plume originating in circle 1 travels along the shore of Hudson Bay to the south from 1800UTC 22 July to 1800UTC 23 July. Comparing the MODIS AODs (Figure 3.8(e), around 55°N, 90°W) and the smoke AODs modeled by the SMOKE10 and the integrated emission cases on 23 July (Figures 3.8(f) and 3.8(h), around 55°N, 87°W), we find that the locations of

modeled smoke plumes shift to the north by about 3°. In contrast, the FRP case fails to produce this smoke plume as shown in Figure 3.8(g).

As shown in Figure 3.8(b) (the SMOKE10 case), in circle 2 are located several smoke plumes with high smoke loadings but relatively small horizontal extent, which are traceable to the ABBA smoke emissions in boxes 4, 5, and 6 on 22 July. In contrast, the horizontal extent of the smoke plumes in the FRP case is much larger. This is due to the fact that in the FRP dataset, smoke particles are assumed to be emitted much earlier than 1800UTC 22 July as shown in Figures 3.6(h), 3.6(j), and 3.6(l). In the same region, the smoke plumes produced by the integrated emission case are very similar to the ones in the SMOKE10 case as shown in Figure 3.8(h), simply because of the fire duration adjustment process. In the next 24 hours, the smoke plumes in circle 2, as indicated by the arrow, travel down to the south first, interact with the cold frontal system, and then move to the south of Hudson Bay (50°N~55°N, 75°W~90°W). Comparing the smoke AOD fields in this region, we find that the maximum modeled AOD values in the SMOKE10 case (>2, as shown in Figure 3.8(f)) are close to the MODIS observations (Figure 3.8(e)), while the values in the FRP case are smaller (<2, as shown in Figure 3.8(g)). In addition, relatively strong smoke plumes (>0.5) in the FRP case contaminate the entire cold frontal system stretching from 55°N,70°W to 50°N, 90°W, while the smoke plumes in the SMOKE10 case are mainly concentrated in the lower portion of the frontal system (50°N~55°N, 80°W~90°W). Apparently, the differences in the maximum AOD values and spatial coverage between the SMOKE10 and the FRP cases on 23 July are due to the difference in smoke emissions in circle 2 on 22 July. It should be noted that, in the FRP case, the smoke emitted on 21 July as labeled by circle 3 in Figure 3.8(c) also

contributes to the smoke plumes that are swirled into the cold frontal system. Similar to the SMOKE10 case, the integrated emission case only produces a relatively large amount of smoke loading in the lower portion of the frontal system (50°N~55°N, 80°W~90°W) as shown in Figure 3.8(h); however, the magnitudes of modeled AODs in this region are relatively close to the ones in the FRP case, rather than the SMOKE10 case.

The SMOKE10 case performs better than the other two cases on 23 July, in terms of RMSD, correlation coefficient, and the Taylor skill metric as shown in Table 2. The better representation of the spatial distribution of smoke plumes modeled by the SMOKE10 case is to a large extent due to the reasonable amount of smoke emissions in circle 1 and the realistic diurnal cycle of smoke emission in circle 2. Comparing the RMSDs, correlation coefficients, and Taylor skill metrics of the other two cases, we find that the integrated emission case performs much better than the FRP case owing to the fire duration adjustment. In addition, we find that the average AOD values of the three cases are reasonably close to the average MODIS AOD value on 23 July, if a small value of background AOD, say 0.1, is considered. Out of three cases, the FRP case produces the highest average AOD value due to the strong smoke loadings within the entire frontal system as shown in Figure 3.8(g).

As shown in Figure 3.8(f), the modeled smoke plumes in circle 4 are traceable to the smoke emitted in boxes 4, 5, and 6 on 23 July. As discussed before, the active fires in this region (especially in box 5) quickly propagate because of the strong winds associated with the passing cold frontal system. As a result, we can see many smoke plumes in the SMOKE10 case. Each individual smoke plume has relatively small horizontal extent and relatively moderate magnitude. In contrast, the FRP case only produces a few smoke

plumes with high smoke loadings in the same region as shown in Figure 3.8(g). This is due to the fact that the FRP smoke emission dataset is not able to capture the aforementioned quick propagation of active fires. As shown in Figure 3.8(h), the smoke plumes modeled by the integrated emission case in the same region have spatial patterns similar to the ones in the SMOKE10 case, but smaller magnitude of AODs.

As indicated by the arrow in Figure 3.8(f), the smoke particles emitted in circle 4 are transported to the southeast for the next 24 hours. On 24 July, the smoke plumes mainly contaminate a region along the shore of Hudson Bay (50°N~55°N, 75°W~95°W) as shown in the MODIS AOD field (Figure 3.8(i)). Comparing the modeled smoke plumes, we find that the SMOKE10 case, as shown in Figure 3.8(j), is able to capture the horizontal extent of the smoke plumes and the magnitude of the smoke AODs (especially for the AODs with values of 1~2), but is not able to produce enough model grids with AODs higher than 2 as observed by MODIS (Figure 3.8(i)). In contrast, the FRP case, as shown in Figure 3.8(k), produces too many model grids with AODs larger than 2 and relatively smaller horizontal extents compared to the MODIS AOD field. Apparently, the differences in modeled AOD fields on 24 July between the two cases are mainly due to the differences in spatiotemporal distribution of smoke emissions in boxes 4, 5 ,and 6 on 23 July as discussed before. In the same region, the integrated emission case, as shown in Figure 3.8(l), produces smoke plumes with horizontal extent similar to those in the SMOKE10 case; however, the magnitude of smoke AODs is underestimated compared to the MODIS AODs (for example, significantly fewer model grids with AODs higher than 1 compared to the SMOKE10 case).

Table 3.3: Statistical comparison between observed and modeled AOD fields for three days from 22 July to 24 July, 2007.

Modeling cases	22 July (1364 pairs)				23 July (2578 pairs)				24 July (6452 pairs)			
	Correlation	RMSD	Averaged AOD	Taylor skill	Correlation	RMSD	Averaged AOD	Taylor skill	Correlation	RMSD	Averaged AOD	Taylor skill
MODIS	1	0	0.85	1	1	0	0.34	1	1	0	0.78	1
ABBA	0.603	0.885	0.18	0.278	0.45	0.404	0.27	0.724	0.201	0.919	0.52	0.593
FRP	0.365	0.743	0.54	0.627	0.181	0.486	0.29	0.589	0.344	1.127	0.69	0.492
The integrated	0.458	0.761	0.41	0.570	0.314	0.436	0.25	0.634	0.251	0.952	0.47	0.603

The smoke plumes modeled by the SMOKE10 and FRP cases also differ significantly in circle 5 as shown in Figure 3.8(g) on 23 July. The smoke plumes in this region are traceable to the smoke emissions in box 2 and some other fire clusters (for example, one located to the north of box 2 above 60°N). We find that the smoke plumes in the FRP case have higher smoke loading compared to those in the SMOKE10 case. This is because: 1) smoke is emitted earlier in the FRP dataset in box 2 on 23 July as compared to the ABBA dataset; 2) the ABBA dataset fails to detect many active fires in this region, especially above 60°N. Within the next 24 hours, the smoke plumes in circle 5 are transported along the route (red arrow as shown in Figure 3.8(g)) above Hudson Bay. As shown in the MODIS AOD field on 24 July (Figure 3.8(i)), the smoke plume over Hudson Bay (55°N~60°N, 80°W~90°W) is fairly intense: Many MODIS AOD pixels are around 1~2. In the same region, both the FRP and the integrated emission cases capture the spatial patterns of the smoke plumes as shown in Figures 3.8(k) and 3.8(l); however, the former case moderately underestimates the magnitude of smoke AODs, especially in the region of 55°N~58°N, 80°W~85°W, while the latter case underestimates the magnitude of smoke AODs at least by a factor of two. In contrast, the SMOKE10 case is not able to reproduce the smoke plume in this region as shown in Figure 3.8(j) mainly because the ABBA dataset significantly underestimates the smoke emissions in circle 5 on the previous day.

By examining the statistical analysis results for 24 July in Table 3.3, we find the following results: 1) The smoke loading produced by the FRP case is reasonably close to the observation based on averaged values of observed and modeled AODs (0.69 versus 0.78). In contrast, the averaged AOD value in the SMOKE10 case is lower than the

observation (0.52 versus 0.78). Even if we consider a background AOD, for instance a value of 0.1, the modeled AOD is still lower than the observation by a value of about 0.1~0.2. The underestimation, to a large extent, originates from the fact that the SMOKE10 case fails to reproduce the smoke plumes over Hudson Bay. Due to the fire duration adjustment, the integrated emission case significantly underestimates the smoke AODs as compared to the other two cases and MODIS observations. 2) Similar to the previous two days, the correlation coefficient and RMSD produced by the integrated emission case rank between the values of the other two cases. 3) Because the integrated emission case captures the smoke plumes in both circles 4 and 5, it acquires the highest Taylor skill metric among all three cases.

As shown in Table 3.3, for three days, the averaged AOD values modeled by the three cases are all smaller than averaged MODIS AOD values. As discussed above, the underestimation of AODs by the modeling cases is mainly due to 1) omission of the background of AODs; 2) active fire not being detected by GOES or MODIS satellites in some regions; and 3) disagreement in the spatial distribution of smoke plumes between modeling and observations (i.e. the location of the modeled smoke plume over Hudson Bay shifts to the north by about 3° as shown in Figure 3.8(f)).

3.4 Assessment of the Effect of Varying Amounts of Smoke Emissions on Clouds and Precipitation

3.4.1 Analysis of the SMOKE10 Case against Observations

The horizontal distribution of smoke field modeled by the SMOKE10 case has been validated in the previous section. In this section, we first use the vertical feature mask (VFM) product from CALIPSO to evaluate the model smoke vertical distribution. Figure 3.9 shows a cross section of the VFM product along the A-Train path on 1800 UTC 23 July 2007. In Figures 3.9(a) and 3.9(b), the red circles (between 54°N-55°N and 3-4 km above the ground) show the presence of smoke inside the cloud deck captured by CALIPSO. Figures 3.9(c) and 3.9(d) show that this signal is well reproduced by WRF-Chem-SMOKE. Simulations with two different smoke emission cases (SMOKE1 and SMOKE10) exhibit similar spatial distributions of smoke plumes but differ in smoke loadings: the maximum smoke concentrations (54°N-55°N and 3-4 km above the ground) are 59.0 μg/m^3 and 5.2 μg/m^3 for SMOKE10 and SMOKE1, respectively.

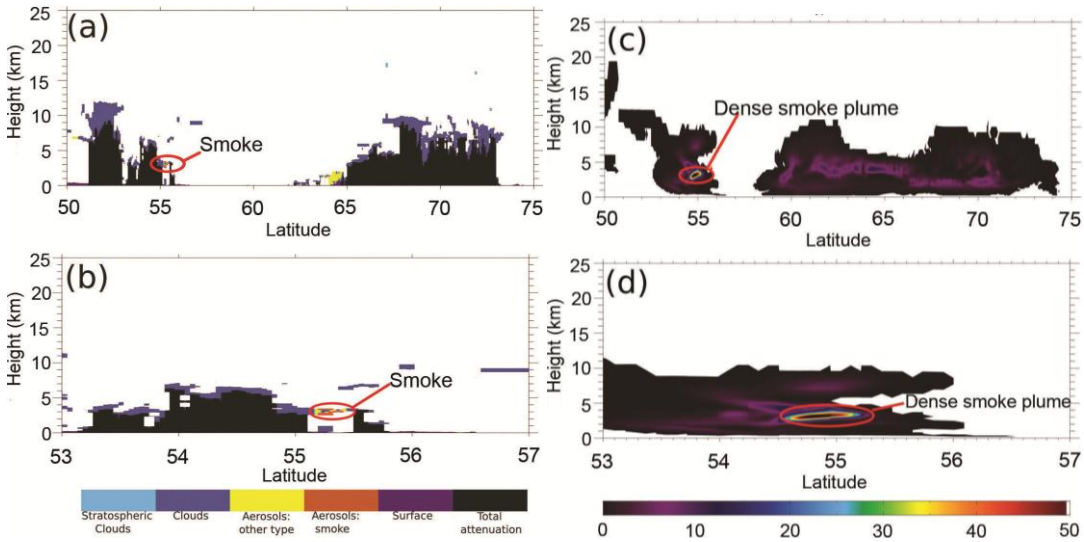

Figure 3.9: (a) CALIPSO vertical feature mask (VFM) cross section along the A-Train path shown in Fig. 3.1 on 1800 – 1810 UTC 23 July 2007, (b) zoom in CALIPSO VFM between 53°N and 57°N, and (c) and (d) modeled smoke mass concentration (μg/m3) along the same A-Train path corresponding to (a) and (d).

We use the SMOKE10 case (strong smoke emissions) to compare simulated smoke and cloud fields against A-Train observations. A high-latitude cyclonic system

developing on 21 July 2007 over northwestern Canada moves over the Hudson Bay on 22 July. A large deck of mixed-phase altocumulus clouds forms along the cold front seen in MODIS images, CALIPSO VFM product, and CloudSat cloud classification (not shown). At the same time, the cloud desk is affected by smoke. On 23 July, this system reaches a mature stage. An occluded front that formed in the system stretches along the east coast line of Canada, as seen in the MODIS true color image (Figure 3.1, the comma-shaped cloud system) and MODIS water path product (Figure 3.10(a)). In the meantime, a new cyclonic system starts to form in northeastern Canada. Then between these two systems, several low-level cloud decks form around Southampton Island. MODIS cloud top temperature product (not shown) suggests that they are liquid-phase clouds.

The modeled AOD field (Figures 3.8(f)) shows that at 1800UTC on 23 July 2007, the mature cyclonic system is under the influence of smoke, especially the cloud system in the cold front, which contains a large amount of smoke, as seen in the MODIS true color image (Figure 3.1(a)), MODIS AOD (Figure 3.8(e)), and CALIPSO VFM (Figure 3.9(b)). The smoke concentration in the warm front is relatively low because of wet removal as discussed below.

The column-integrated CDNC field activated from smoke particles is not necessarily proportional to smoke loading because smoke CCN activation also requires favorable thermodynamic conditions. We find the largest column-integrated CDNC from smoke particles ($>2\times10^{11}$ no./m^2) occurring in the occluded front and the liquid phase cloud deck of the newly-forming cyclonic system (Figure 3.10(b)). Examining CDNC of each model grid reveals that SMOKE10 produces a CDNC value much higher than the background value (maximum 2100 no./cm^3 vs. 50 or 100 no./cm^3).

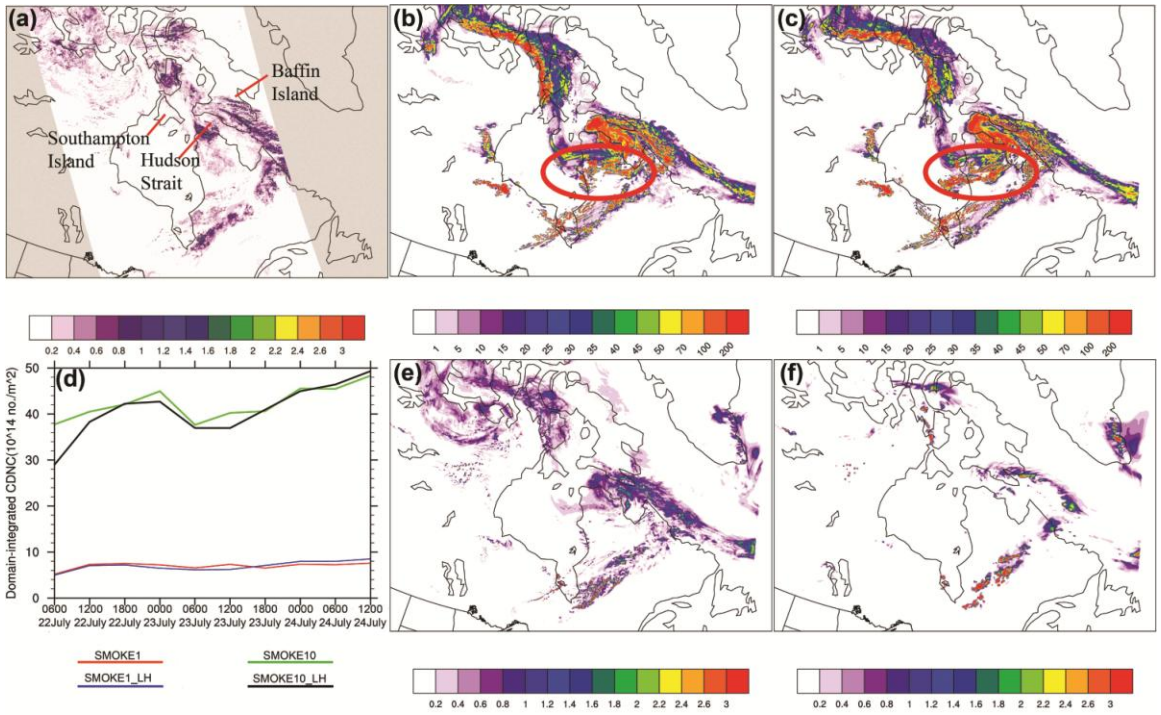

Figure 3.10: (a) MODIS water path product (kg/m^2) on 1800-1810 UTC 23 July, 2007. (b) Column-integrated cloud droplet number concentration (CDNC) (SMOKE10 case, 10^9 no./m^2) on 1800 UTC 23 July, 2007. (c) Column-integrated cloud droplet number concentration (CDNC) (SMOKE10_LH case, 10^9 no./m^2) on 1800 UTC 23 July, 2007. (d) Time series of domain-integrated CDNC (the sum of column-integrated CDCN over the domain) for SMOKE10, SMOKE10_LH, SMOKE1, and SMOKE1_LH (10^{14} no./m2) (e) Modeled liquid water path (SMOKE10 case, cloud water + rain, kg/m^2). (f) Modeled ice water path (SMOKE10 case, cloud ice + snow + grauple, kg/m^2).

To assess the effect of hygroscopicity of the residual particulate matter on smoke CCN activation, we examine the column-integrated CDNC field of the SMOKE10_LH case shown in Figure 3.10(c). By comparing Figures 3.10(b) and 3.10(c), we find that the CDNC fields in SMOKE10_LH and SMOKE10 are very similar in terms of the spatial distribution and magnitudes. The only noticeable differences between these two fields occur in the cloud streaks behind the cold front where more CDNC is produced in SMOKE10_LH (shown with the red circles in Figures 3.10(b) and 3.10(c)).

For the snapshot (1800UTC 23 July) shown in Figures 3.10(b) and 3.10(c), SMOKE10_LH generates 0.8% more domain-integrated CDNC (the sum of all column-integrated CDNC values over the domain) than SMOKE10. It seems like an unexpected result since the residual particulate matter in SMOKE10_LH has lower hygroscopicity compared to SMOKE10. However, examining the time series of the domain-integrated CDNC values shown in Figure 3.10(d), we note that SMOKE10 produces, on average, 7.5% more CDNC than SMOKE10_LH before 1800UTC 23 July and about 1.5% less after that time. This can be explained by the longer time required for smoke particles to be activated in SMOKE10_LH compared to SMOKE10. Nevertheless, overall differences in the domain-integrated CDNC between SMOKE10_LH and SMOKE10 are very small. In contrast, varying total smoke emission amounts has a significant impact. Figure 3.10(d) shows that the domain-integrated CDNC values in SMOKE1 and SMOKE1_LH are similar but much lower than those predicted in SMOKE10 and SMOKE10_LH cases.

Figures 3.10(e) and 3.10(f) show the modeled liquid water path (LWP) (cloud water + rain) and ice water path (IWP) (cloud ice + snow + graupel) for 1800UTC 23 July 2007 for SMOKE10. In general, the spatial distribution of the modeled LWP reasonably reproduces the pattern of clouds compared to that of the MODIS water path product (see Figure 3.10(a)). However, the modeled total (liquid+ice) water path is higher in the SMOKE10 case than it is in observations, especially in the frontal system with a high ice water path (mainly snow).

The SMOKE10 case reproduces the occluded front feature stretching along the east coast of Canada very well. The portion of the occluded front with dominant liquid

phase water has a LWP value from 0.8~1.4 kg/m^2, which is in agreement with observations. However, the occluded front consists of several cells with LWP larger than 2 kg/m^2. Although the water path retrieval also shows some cell features with a large LWP value, the magnitudes are much smaller compared to modeled LWP, possibly resulting from a relatively coarse model grid (5×5 km) compared to the finer resolution of the MODIS water path product (1×1 km). However, the water path of the modeled cloud deck associated with the low-pressure center of the cyclonic system is reasonably reproduced, but the spatial distribution is biased. As shown in Figures 3.10(a) and 3.10(e), the observed low-pressure center is located over the northern Quebec province, while the modeled low-pressure center is located in the northeast. Compared to observations, the cold front is well simulated. The model successfully reproduces the smaller-scale cloud rolls and streaks behind the cold front, which are classified as stratocumulus clouds by CloudSat (not shown). The model also reasonably captures the other cloud features in the study domain, such as the newly-forming cyclonic system and cloud decks around Baffin Island and Southampton Island.

3.4.2 Effect of Smoke Loading Amount

To examine how various smoke loadings affect the cloud properties and resulting precipitation, we perform modeling experiments with the three smoke emission cases: SMOKE1, SMOKE5, and SMOKE10. In each case, we examine the effect of low vs. high hygroscopicity of residual particulate matter, while the hygroscopicity values of OM and BC remain unchanged. Results are then compared against the CLEAN (smoke-free) case, in which only the background CDNC is considered.

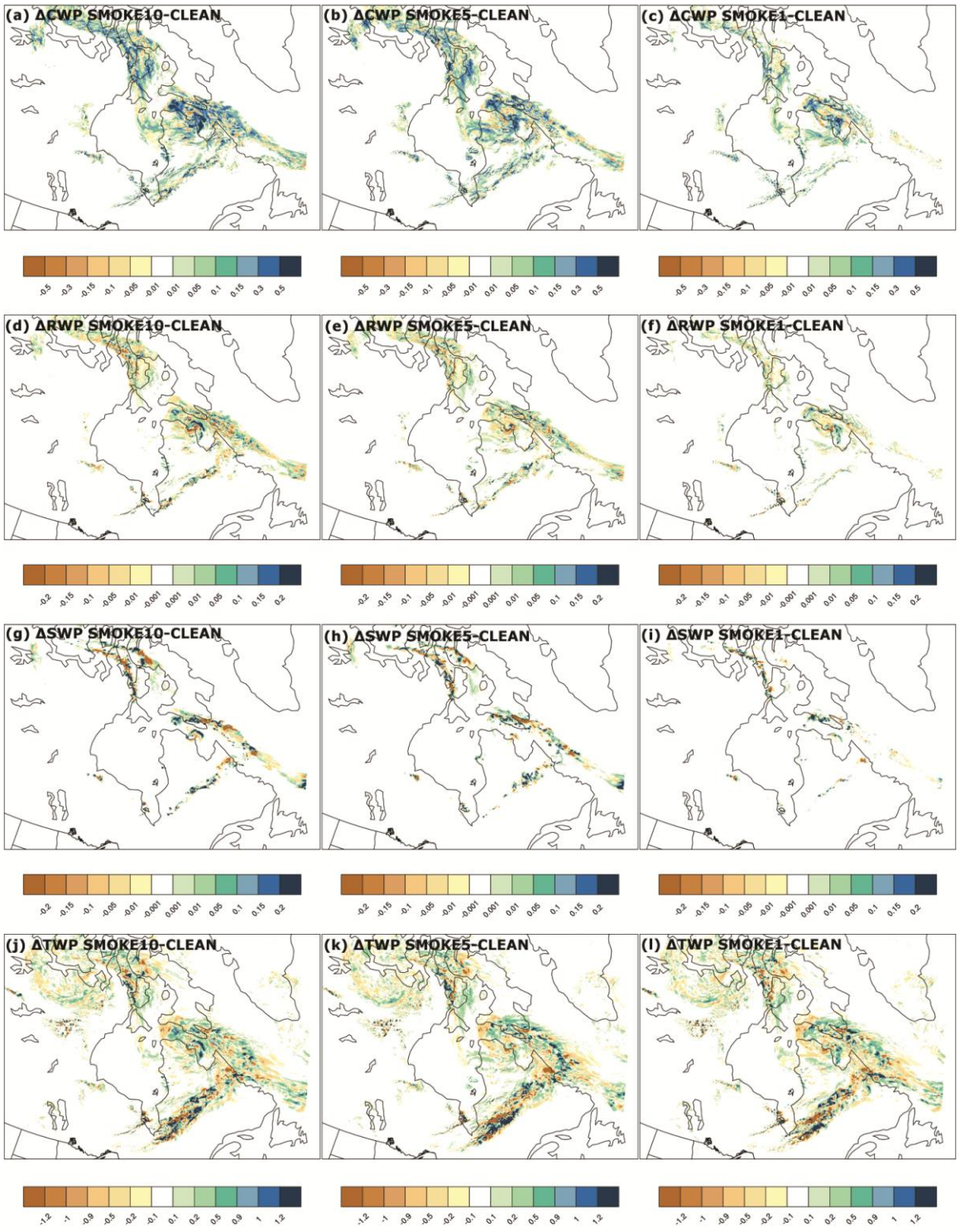

Figure 3.11: From left to right: difference fields between the smoke cases (SMOKE10, SMOKE5 or SMOKE1) and clean case (CLEAN). From top to bottom: CWP differences (kg/m^2) (shown are only model grids with CDNC activated from smoke particles (CNDC>5 no./cm^3); RWP differences in CDNC-masked model grids (kg/m^2); SWP differences (kg/m^2) in CDNC-masked model grids; and TWP differences (kg/m^2). All results are for 1800 UTC 23 July, 2007.

The first three rows in Figure 3.11 present differences in cloud water path (CWP), rain water path (RWP), and snow water path (SWP) between each smoke case and CLEAN (from left to right: SMOKE10-CLEAN, SMOKE5-CLEAN, and SMOKE1-CLEAN)) on 1800 UTC 23 July 2007. In order to delineate the smoke-induced changes in the cloud properties, only the model grids with CDNC activated from smoke particles are shown (CDNC > 5 no./cm^3). The last row in Figure 3.11 shows the differences in TWP. Shown values of TWP are for all of the model grids (no CDNC masking) to demonstrate the overall effect of smoke. The first row in Figure 3.11 shows that the absolute value and the spatial extent of CWP difference fields gradually decrease from SMOKE10 to SMOKE1. For SMOKE10 and SMOKE5, it is apparent that the model grids with CDNC activated from smoke particles contain large amounts of cloud water (dominant positive changes). For SMOKE10-CLEAN, nearly all of the cloud decks in the region with activated CDNC have positive differences (Figure 3.10(b)). In particular, the occluded front and low-pressure center of the mature cyclonic system show the largest difference value, higher than 0.5 kg/m^2. The differences in CWP of SMOKE5-CLEAN are similar to those of SMOKE10-CLEAN, except the values are smaller in the former group. Unlike in the SMOKE10 and SMOKE5 cases, both positive and negative changes are apparent in the differences between SMOKE1 and CLEAN. While the occluded front mainly show positive changes of around 0.1 kg/m^2, the cold and warm fronts show either positive or negative changes but of the smaller magnitude (about +/- 0.05 kg/m^2).

Several microphysical processes control RWP in mixed-phase clouds. For fixed liquid water content, the higher number concentration of cloud droplets leads to smaller

droplet sizes and a slower collision-coalescence rate. As a result, the formation of rain is suppressed, and water remains in the form of cloud droplets (positive changes of CWP in SMOKE10 and SMOKE5, shown in Figures 3.11(a) and 3.11(b)). In addition, snowmelt during the fallout also affects RWP, which explains the existence of both positive and negative changes in RWP between the smoke cases and the clean case, as shown in the second row in Figure 3.11. For SMOKE10-CLEAN, relatively small changes in RWP (0.05~ -0.05 kg/m^2) occur in the cloud deck of the newly-forming cyclonic system. In the center of the cyclonic system and the occluded front, relatively large negative and positive RWP changes (0.2~ -0.2 kg/m^2) occur. The dipole feature in the low-pressure center indicates a shift of the rain formation in space. The strong positive signals of RWP differences over the Hudson Strait correspond to those of enhanced SWP in this region. RWP differences in SMOKE5-CLEAN are similar to those in SMOKE10-CLEAN; however, the spatial patterns of RWP changes differ significantly among these cases. For example, SMOKE5 produces more rain along the occluded front and less in the low-pressure center. Compared to the changes in RWP in SMOKE10 and SMOKE5, those in SMOKE1 are smaller in terms of both the spatial extent and the magnitude. As shown in the third row in Figure 3.11, the differences in SWP among smoke cases mainly occur at the edges of cloud decks such as fronts and low-pressure centers where snow is forming. Again, SMOKE10 tends to produce more snow in the center of the cyclone over the Hudson Strait while SMOKE5 produces more snow in the fronts.

The last row in Figure 3.11 presents the differences in the total water path (TWP), with no CDNC masking. The first three rows of Figure 3.11 show that the influence of smoke on the cloud microphysical processes leads to both positive and negative changes

in CWP, RWP, and SWP. Therefore, not surprisingly, the TWP difference fields are very "patchy". Similarly, *Graf et al*. [2009] showed very noisy, patchy patterns in cloud properties and precipitation changes caused by smoke. It is most likely that these patchy features would diminish if even higher smoke loading would be introduced. For example, compared to CLEAN, SMOKE10 tends to produce several cloud cells with high water content in the low-pressure center, while SMOKE5 tends to produce the stronger occluded front. However, the difference fields of SMOKE1 minus CLEAN have smaller magnitudes with no clear spatial patterns. Based on the TWP difference field between SMOKE10 and CLEAN, it seems that both cases fail to capture the exact location of the cloud deck associated with the low-pressure center. CLEAN is closer to the MODIS water path observations compared to other cases. However, upon closer examination of TWP of the CLEAN case (not shown), we find that CLEAN significantly underestimates TWP inside the low-pressure center, by 0.5 ~ 1.0 kg/m^2. In addition, the small-scale cloud cell with high water content is not reproduced, a finding that is inconsistent with observations.

Figure 3.12 presents differences in CWP, RWP, SWP, and TWP between SMOKE10_LH and CLEAN on 1800UTC 23 July, 2007, which are computed in the same manner as SMOKE10-CLEAN (Figures 3.11(a), 3.11(d), 3.11(g), and 3.11(j)). We find that the difference fields between SMOKE10_LH and CLEAN are very similar to the ones between SMOKE10 and CLEAN in terms of the magnitude and spatial distribution. One important discrepancy is that the cloud streaks behind the cold front (shown by the red circle in Figure 3.12(a)) have more CWP in SMOKE10_LH than in SMOKE10 because of more CDNC in this area in SMOKE10_LH seen in Figures

3.10(b) and 3.10(c). The difference fields in CWP, RWP, SWP, and TWP between SMOKE1_LH and CLEAN are also very close to the ones between SMOKE1 and CLEAN (not shown).

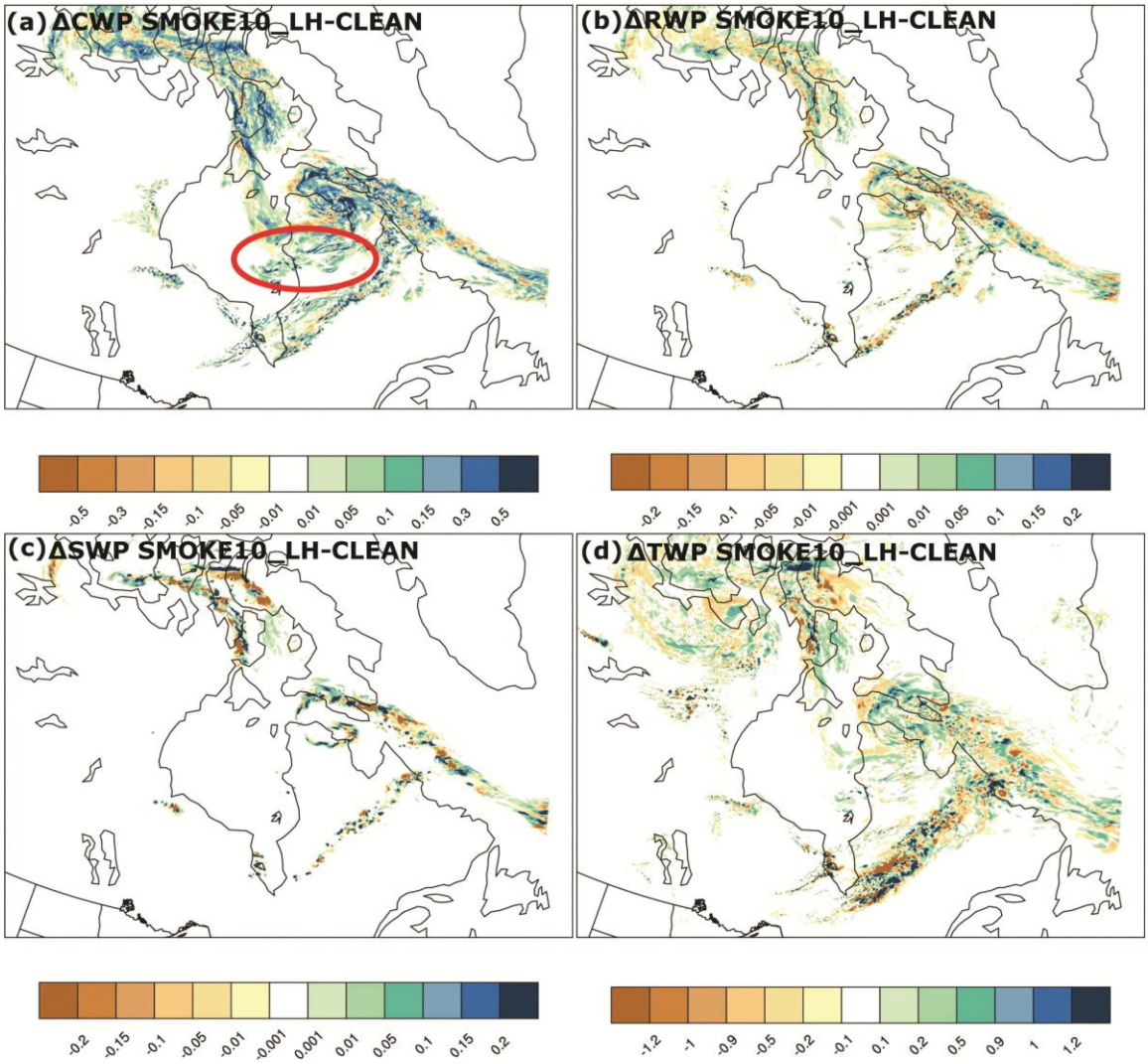

Figure 3.12: Difference fields between SMOKE10_LH and CLEAN: (a) CWP differences (kg/m^2) (shown are only model grids with CDNC activated from smoke particles (CNDC>5 no./cm^3); (b) RWP differences in CDNC-masked model grids (kg/m^2); (c) SWP differences (kg/m^2) in CDNC-masked model grids; and (d) TWP differences (kg/m^2). All results are for 1800 UTC 23 July, 2007.

In addition, we examine domain-integrated differences in clouds and precipitation between the smoke cases and CLEAN. Figure 3.13 shows differences in CWP, RWP, and SWP that are summed over the entire domain from 0600UTC 22 July to 1200UTC 24 July 2007, every six hours. Figure 3.13 also shows the differences in six-hour precipitation over the whole domain for the same time period. It should be noted that the differences in CWP, RWP, and SWP presented in Figure 3.13 are not CDNC masked.

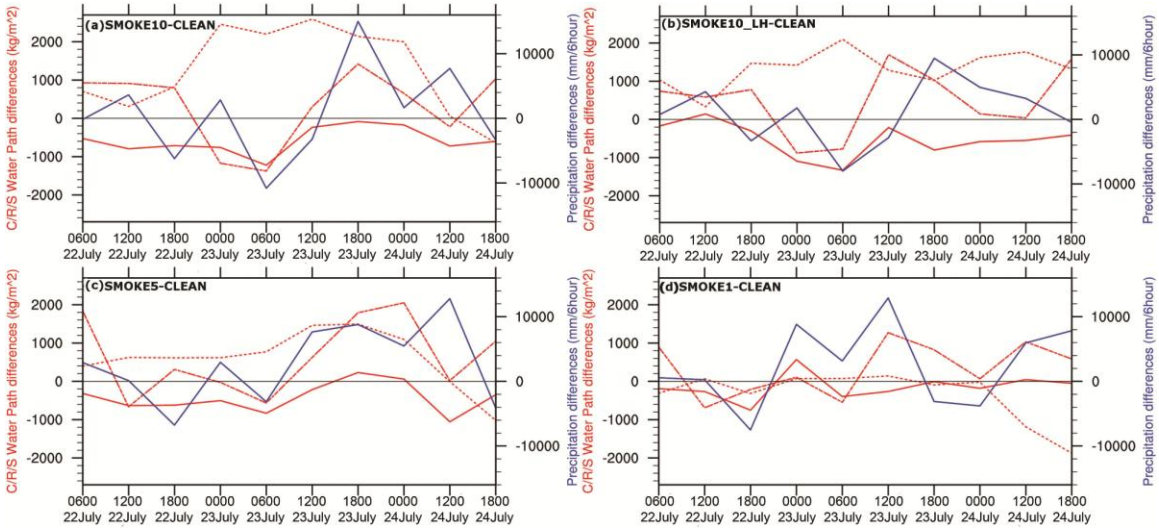

Figure 3.13: Differences in the cloud properties and precipitation between smoke cases ((a) SMOKE10, (b) SMOKE10_LH, (c) SMOKE5, or (d) SMOKE1) and the CLEAN case. Dotted line: differences (kg/m^2) in domain-integrated cloud water path between the smoke case and the CLEAN case (from 0600 UTC 22 July to 1200 UTC 24 July). Red solid line: differences in domain-integrated rain water path. Dashed line: differences in domain-integrated snow water path. Blue solid line: differences in the domain-integrated six-hour precipitation.

The solid line in Figure 3.13(a) represents differences in RWP between SMOKE10 and CLEAN. As discussed above, changes in RWP can be caused by several microphysical processes. For example, the collision-coalescence process, altered by more cloud droplets and abundant cloud water, tends to decrease RWP, while snowmelt during fallout tends to increase RWP. Figure 3.13(a) shows that changes in RWP remain

negative through the entire period, indicating that the suppressed collision-coalescence process is most likely a dominant factor in determining RWP in SMOKE10. With the warm rain process being suppressed, the excess water vapor is transferred into cloud droplets. A significant increase in CWP is seen after 1800 UTC 22 July, and it remains high until 0000 UTC 24 July. In addition, the excess water and more ice crystals produced from contact freezing and immersion freezing modes initially lead to an increase in SWP. After 0000 UTC 23 July, however, the SWP difference between SMOKE10 and CLEAN dramatically decreases, becoming negative. This is likely the result of reduced riming efficiency in the high CCN (CDNC) condition such as that in SMOKE10, which causes a slower snow growth rate [*Saleeby et al*., 2009]. In the CLEAN case, heavily rimed snow particles form and fall through the atmosphere very fast, resulting in precipitation. By contrast, in SMOKE10, lightly-rimed snow particles grow slowly at first, but after 12:00UTC 23 July they grow large enough to acquire an appreciative fall velocity. As a result, SWP differences become positive and snowmelt increases RWP (although the difference between RWP of smoke SMOKE10 and that of CLEAN remains negative). Meanwhile, the CWP differences become smaller as cloud droplets transforming into snow through the riming process.

Because of the inhibition of both the warm rain process and the riming process, precipitation in SMOKE10 is suppressed initially, until 1200 UTC 23 July. During the following six hours, however, precipitation increases significantly (> 15,000 mm, domain integrated) because of the formation of large amounts of snow. As a result, SWP, RWP, and CWP are decreased during the following 12 hours.

Figure 3.13(b) shows the differences in domain-integrated CWP, RWP, SWP, and six-hour precipitation between SMOKE10_LH and CLEAN. Similar to SMOKE10, precipitation in SMOKE10_LH is suppressed until 1200UTC 23 July and is invigorated later in time. The difference in domain-integrated six-hour precipitation in the SMOKE10_LH-CLEAN case on 1800UTC 23 July is around 10,000 mm, which is smaller compared to SMOKE10-CLEAN. The RWP differences of SMOKE10_LH-CLEAN (shown with the solid red line in Figure 3.13(b)) remain negative, except during a short period around 1200UTC 22 July. However, the magnitudes of the RWP differences in SMOKE10_LH-CLEAN and SMOKE10-CLEAN cases are similar.

SWP differences of SMOKE10_LH-CLEAN also remain negative from 0000UTC to 0600UTC 23 July, indicating the suppression of riming processes in both SMOKE10 and SMOKE10_LH during this period. However, magnitudes of SWP differences of SMOKE10_LH-CLEAN are smaller compared to those of SMOKE10-CLEAN. On 1200UTC 23 July, SMOKE10_LH produces 1694 kg/m^2 more SWP compared to CLEAN. This large positive difference in SWP between SMOKE10_LH and CLEAN is very close to the one between SMOKE10 and CLEAN on 1800UTC 23 July (1419 kg/m^2). Similar to SMOKE10, SMOKE10_LH produces much more CWP than CLEAN. Although the CWP differences of SMOKE10_LH-CLEAN are smaller than those of SMOKE10-CLEAN before 0000UTC 24 July, they are still much larger compared to the CWP differences between other smoke loading cases and CLEAN as shown below. It is noteworthy that, after 0000UTC 24 July, the CWP differences of SMOKE10_LH-CLEAN exhibit only a small decrease, whereas the CWP differences of SMOKE10-CLEAN decrease significantly.

The differences in SWP and CWP of SMOKE10_LH-CLEAN and SMOKE10-CLEAN can be explained by differences in domain-integrated CDNC between these cases as discussed above. For example, before 1200UTC 23 July, more domain-integrated CDNC are generated in SMOKE10 than in SMOKE10_LH (see Figure 3.10(d)). As a result, the positive differences in CWP in SMOKE10-CLEAN are larger than those in SMOKE10_LH-CLEAN. For the same reason, the riming process in SMOKE10 is more severely suppressed compared to SMOKE10_LH, which leads to larger negative differences in SWP between SMOKE10 and CLEAN than those between SMOKE10_LH and CLEAN. After 0000UTC 24 July, however, more domain-integrated CDNC are produced in SMOKE10_LH than in SMOKE10. As a result, the positive differences in CWP in SMOKE10_LH-CLEAN become larger than in SMOKE10-CLEAN.

Similar to the rain formation in SMOKE10, rain in SMOKE5 is suppressed during the entire period, except during a short period from 1800 UTC 23 July to 0000 UTC 24 July, shown in Figure 3.13(c). In addition, the differences in CWP remain positive; however, their magnitudes are about a half of the CWP differences between SMOKE10 and CLEAN from 1800 UTC 22 July to 0000 UTC 24 July. By examining the differences in SWP (dashed line in Figure 3.13(c)), we find that they are negative only at two times (1200 UTC 22 July and 0600 UTC 23 July) and their values are relatively small. These findings imply that the riming process in SMOKE5 is less likely affected than it is in SMOKE10 and SMOKE10_LH. After 1200 UTC 23 July, the dramatic increase in SWP in SMOKE5 leads to an increase in precipitation and RWP during a short period of

snowmelt, but it causes a decrease in CWP. The significant increase in precipitation in SMOKE5 occurs six hours earlier than it does in SMOKE10, but it is less vigorous.

Figure 3.13(d) shows that the behavior of SMOKE1 differs significantly from that of the other smoke emission cases. The CWP differences in SMOKE1-CLEAN remain small throughout the entire simulation period, leading to relatively small changes in RWP. On 0000UTC 23 July, SMOKE1 produces more RWP than CLEAN by 570 kg/m^2. This positive difference, not seen in either SMOKE10 or SMOKE5, is most likely the result of the relatively clean environment (low background CDNC) at high latitudes, where CCN activated from a small amount of smoke can establish favorable conditions for rain formation. As a result, the increase in precipitation in SMOKE1 case occurs on 0000 UTC 23 July, which is earlier than in the other smoke emission cases. We also examine differences in domain-integrated CWP, RWP, SWP, and six-hour precipitation between SMOKE1_LH and CLEAN, which turn out to be very similar to those between SMOKE1 and CLEAN (not shown). In particular, the signs and magnitudes of these differences and the delay in precipitation onset are practically same.

To further explore the effect of smoke loading on the spatiotemporal distribution of precipitation, we examine changes in precipitation patterns and compared the predicted daily precipitation of SMOKE10, SMOKE10_LH, and CLEAN to daily precipitation observations from the Canadian National Climate Data and Information Archive. In particular, we analyze precipitation data for three provinces (Quebec, Newfoundland, and Nunavut) on 23 July. Out of 391 stations, data from only 17 stations (the black dots in Figure 3.1(a)) are available for comparison; the remaining stations are located outside of the study domain, or no data are available for them. In addition, we exclude stations if

both observed precipitation and modeled precipitation of the corresponding model grid are too low. We select 17 grid cells (each 5x5 km) corresponding to the 17 considered stations to construct scatter plots of modeled vs. observed daily precipitation rates. Figure 3.14 presents the scatter plots with each point representing a station/grid pair for SMOKE10 (red dots), SMOKE10_LH (red circles), and CLEAN (blue dots). The regression analysis for SMOKE10, SMOKE10_LH, and CLEAN gives the slope values are 1.28, 1.31, and 1.60, respectively. The slope values suggest that all three cases overestimate observed precipitation, especially for heavy precipitation events. The smoke cases appear to be in better agreement with observations than CLEAN. However, since a number of factors control the formation of precipitation, we cannot prove that the inclusion of smoke in model simulations leads to better agreement with observations in this case.

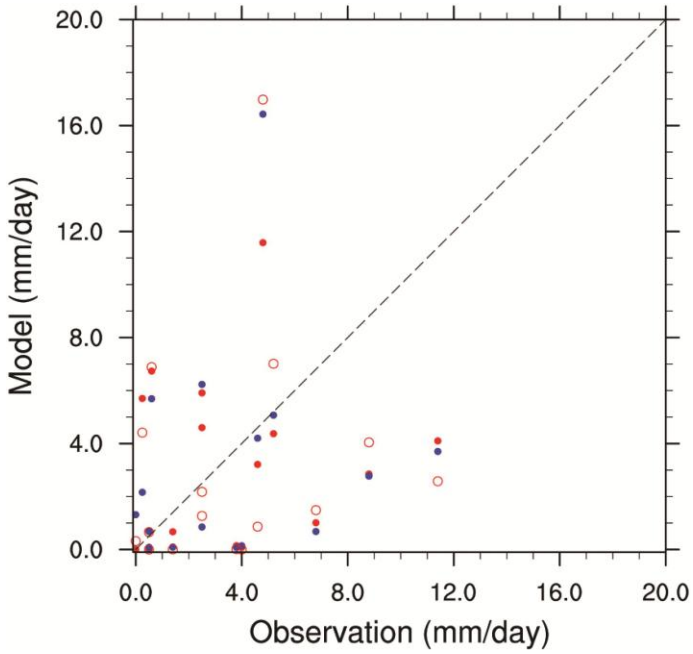

Figure 3.14: Scatter plot of the model simulations of daily precipitation vs. that of the observations for 23 July 2007. The red dots represent SMOKE10 vs. Observations, the red circles represent SMOKE10_LH vs. Observations, and blue dots represent CLEAN vs. Observations.

3.5 Conclusions

In this study, we evaluate the performances of multiple satellite products and techniques in estimating smoke emissions and examine the influence of the amount of smoke emissions on the cloud properties and associated changes in precipitation using the fully-coupled WRF-Chem-SMOKE model. The chemical composition of smoke particles is represented by organic matter (OM), black carbon (BC), and residual particulate matter (RPM). The model is capable of representing the size-resolved composition of smoke particles emitted from specific vegetation types and simulating the evolution of smoke (i.e., injection, coagulation, and dry/wet removal processes). The smoke emission datasets are prepared using the BA (burned area) technique in conjunction with the WF_ABBA and MCD45A1 products as well as the FRP (fire radiative power) technique in conjunction with the MCD14A1 product. We incorporate the smoke emission datasets into the model, and compare the modeled AODs of smoke plumes against the level-2 MODIS AOD products. Smoke interactions with clouds through CCN activation and implicitly through IN activation are also represented in WRF-Chem-SMOKE. The model was configured to simulate boreal forest wildfires occurred in Canada in the summer of 2007. The main findings are summarized in the following aspects:

a) The spatiotemporal distribution of smoke emissions estimated by different datasets

The ABBA, FRP, and MCD45 smoke emission datasets all capture the active fire/burned area signals in the major fire clusters (boxes 1-6). When zooming in on each fire cluster, we find that the spatiotemporal distributions and the magnitudes of smoke

emissions predicted by the three datasets do not agree with each other in small scale (~5 km, the resolution of the model grid). In addition, the manner in which they differ from each other varies from one cluster to another. This is directly due to the differences in fire characteristics. The differences in smoke emissions between datasets are partially due to the assumptions that we adopted in the methodology (i.e. diurnal cycle of fire activity assumed as a Gaussian function in the FRP dataset), but are more likely owing to the limitations of satellites under a certain circumstance.

For the fire clusters above or near 60°N (boxes 1 and 2), the ABBA smoke emissions are significantly lower than the FRP smoke emissions. The differences, to a large extent, are due to the fact that the WF_ABBA product/GOES satellite in this region failed to detect many active fires [*Reid et al*., 2009]. The fire clusters in boxes 3 and 4 burned intensely. Dense smoke plumes in the form of strong pyro-convections can block active fire detection in the downwind area; however, the retrieval of the MCD45A1 burned area is less affected in this circumstance. Therefore, compared to the FRP dataset, the MCD45 dataset produces about 1.5~2 times more smoke emissions in box 3 or produces smoke emissions located in the downwind area in box 4. Under the influence of strong winds, the active fires in box 5 propagate quickly from west to east. As polar-orbiting satellites, MODIS failed to capture this quick propagation of active fires. We find that the FRP smoke emissions are mainly located in the western part of the fire cluster; therefore, the horizontal extent of the FRP smoke emissions is smaller compared to the ABBA and the MCD45 emissions.

b) The differences in smoke plumes modeled by different modeling cases

As discussed in Section 3.3.2, we demonstrate that realistic representation of the dynamics of smoke emissions in individual fire clusters is critical to the ability to reasonably model the spatiotemporal distribution and magnitude of the corresponding smoke plume(s). For the smoke plumes originating from fire clusters above 60°N, the SMOKE10 case usually omits the smoke plumes or underestimates their magnitude. (One exception is smoke emissions in box 1 on 22 July, which were not detected by MODIS due to a short fire duration. Therefore, the FRP case omits the corresponding smoke plume as shown in Figure 3.8(g).) For the smoke plumes originating from fast-propagating fire clusters, the FRP case usually produces the smoke plumes with high concentrations but underestimates horizontal extent. This is because MODIS, with low temporal resolution, fails to capture the spread of the fire fronts.

By comparing them to the MODIS AOD fields (level 2) point-to-point, we also validate the modeled smoke plumes through statistical analyses. We find that, although the magnitudes of AODs modeled by the SMOKE10 and FRP cases are relatively close to the MODIS observations, the averaged values of modeled AODs are underestimated for the three days of 22-24 July, 2007. The possible reasons are discussed at the end of Section 3.3.2. Judging by the correlation coefficients, RMSDs, and Taylor skill metrics of the three days, we find that the FRP (or SMOKE10) case does not always perform better than the other throughout the three days. This fact highlights the need for integrating the smoke emission datasets.

c) The performance of the integration methodology

In this study, we propose a possible methodology for integrating the ABBA, FRP, and MCD45 smoke emissions on a model grid-basis. When examining an individual fire cluster, we find that the integrated smoke emission dataset performs reasonably well under various circumstances, and it is able to capture the fire dynamics (i.e. fast-propagating fire fronts) much better than the FRP and MCD45 datasets. However, as a trade-off for better spatiotemporal distributions, the amount of the integrated smoke emissions is reduced compared to the FRP and ABBA smoke emissions (especially during 23 July), mainly due to the fire duration adjustment. As a result, we find that the integrated emission modeling case does not omit any major smoke plumes; however, the averaged AODs are lower than the other two cases (one exception is 22 July). To sum up, the integrated emission case has the highest value for the three-day total Taylor skill metric. This indicates that the integrated emission case yields the best performance among all three cases, although it can still be improved by introducing a multiplying factor like we did for the ABBA dataset.

d) The effect of varying amounts of smoke emissions on cloud properties and precipitation

We find that the amount of smoke emission based on the WF_ABBA data (called SMOKE1 case in the present study) is too low, resulting in unrealistically low smoke aerosol loadings and AODs. To achieve agreement with the satellite data with regard to aerosol optical depth, smoke emissions need to be multiplied by a factor of 10 (the ABBA smoke emissions). Based on our and other past studies, we conclude that the underestimation of smoke emissions is very likely due to the combined effects of low EF

used and underestimation of burned areas by WF_ABBA product over high latitudes. To examine the influence of the varying amounts of smoke emissions, we model cases with five or ten times as many emission (SMOKE5 and SMOKE10) as original smoke emissions. In each case, we consider the hygroscopicity of OM, BC and RPM, with the latter having low or high hygroscopicity.

The SMOKE10 shows the best agreement with observed smoke fields. In this case, spatial distributions of cloud water path modeled with WRF-Chem-SMOKE reasonably reproduce the cloud pattern observed by MODIS. The modeled total (liquid+ice) water path is higher in both the CLEAN and smoke cases than those in observations, especially for the frontal system, which has a large ice water (ice+snow) path. Compared to CLEAN, however, SMOKE10 performs better with regard to spatial patterns and total water path.

For high smoke emissions (SMOKE10 and SMOKE5), we find that model grid cells affected by smoke stored more water in the form of cloud water drops compared to CLEAN. The positive changes in cloud water are found to be proportional to smoke loading. Comparing simulations with low vs. high hygroscopicity of RPM, we find that varying the hygroscopicity of RPM has a much smaller impact on the positive changes in cloud water compared to varying the smoke emission amount. In high smoke emission cases, the collision-coalescence process is most likely reduced because of smaller cloud droplets form in the presence of smoke, leading to the smaller amount of rain in the same grids in the smoke case than in CLEAN. Nevertheless, SMOKE1 (as well as SMOKE1_LH) produces both positive and negative changes in CWP. In addition, the activated CDNC field in these cases provides favorable conditions for rain formation,

which lead to an earlier onset of precipitation than in other smoke cases. Changes in the snow water path (SWP) occur mainly in the frontal system. Compared to other cases, snow formation in SMOKE10 significantly decreases, most likely due to the suppressed riming process. After slower initial growth, more SWP is produced with time. However, when smoke emissions is relatively low (SMOKE1 or SMOKE5), the riming efficiency is less affected. The formation of snow in SMOKE10_LH is affected in the same manner as in SMOKE10, which suggests that the hygroscopicity of RPM has no significant influence on the riming process.

Compared to the CLEAN case, smoke initially suppresses precipitation, but with time, more vigorous precipitation formed, which agrees with the findings of past studies on tropical forest wildfires. For instance, *Andreae et al.* [2004] show that the suppression of precipitation by smoke in Amazonia through the shutdown of a warm rain process eventually lead to the development of ice formation in convective clouds and then the invigoration of precipitation. Our results reveal that in addition to the suppression of warm rain processes, snow in mixed-phase clouds is also suppressed, likely the result of the shutdown of the riming growth of snow. As a consequence, precipitation is initially suppressed, but with time, it was invigorated because more ice crystals are nucleated from the contact-freezing or/and immersion-freezing modes, leading to the formation of more snow. We find that an increase in smoke emissions leads to a longer delay in the onset of precipitation but causes more vigorous precipitation in the final stage. The hygroscopicity of RPM does not affect the delay of precipitation onset, but may slightly weaken the intensity of precipitation in the final stage.

Our results also agree with the findings of an independent WRF-Chem study by *Grell et al*. [2011], who show that the inclusion of smoke leads to a decrease in the coverage and the amount of precipitation during the first 12 hours and then a significant increase during the afternoon hours from convective clouds. Although *Grell et al*. [2011] does not report smoke emission rates used in their study, their results best agree with our findings in the SMOKE10 case.

Our modeling study reveals the complex nature of smoke-induced changes in cloud properties and precipitation; nevertheless, we attempt to summarize some general features in Table 3.4. We present domain-integrated changes in CWP, RWP, SWP, and TWP by characterizing the sign of SMOKE minus CLEAN difference and its relative magnitude (small, moderate, or large), mainly based on results of Figure 3.13. Domain-integrated changes in IWP are too small in all smoke cases and are not shown. We find that high smoke loading leads to large positive changes in TWP, which indicate that smoke-contaminated clouds can hold more water producing no precipitation. Higher smoke loadings suppress precipitation initially, but ultimately cause an invigoration of precipitation.

Ultimately, the accurate simulation of the impact of smoke on clouds and precipitation will require improved treatment of many components and processes (e.g., fire chemistry, dynamics, thermodynamic, radiation, and aerosols) [*Levin and Cotton*, 2008]. Studies have shown, for instance, that the choice of the PBL scheme, the convective scheme, and the land surface model may all have a significant effect on modeled precipitation [e.g., *Jankov et al*., 2005]. Biased representation of a single component or process may lead to incorrectly predicted cloud and precipitation fields.

Even worse, a combination of several biases may lead to a "correct" prediction compared to observations, the diagnosis of which is even more difficult. Nevertheless, our analysis demonstrates the importance of an accurate assessment of smoke emissions and shows the nonlinear, complex responses of clouds and precipitation to the impact of smoke at high latitudes.

Table 3.4: The summary of changes in hydrometeors and precipitation for considered SMOKE cases relative to CLEAN.

	SMOKE10 - CLEAN	SMOKE5 - CLEAN	SMOKE1 - CLEAN
ΔCWP	large(+)	moderate(+)	small(+/-)
ΔRWP	large(-)	moderate(-)	small(+/-)
ΔSWP (early stage)	large(-)	small(-)	small(-)
ΔSWP (later stage)	moderate(+)	large(+)	moderate(+)
ΔTWP (early stage)	moderate (+)	small(+/-)	small (+/-)
ΔTWP (later stage)	large(+)	large(+)	small(+/-)
Precipitation onset time	significantly delayed (18-24 hours)	moderately delayed (12–18 hours)	slightly delayed (<6 hours)

CHAPTER 4

ANALYSES OF SIBERIA BOREAL WILDFIRES: THE IMPACT OF SMOKE ON CLOUD, PRECIPIATATION, AND RADITIVE FORCING UNDER DIFFERENT FIRE REGIMES AND METEOROLOGICAL CONDITIONS

4.1 Introduction

The impacts of aerosol/smoke on clouds and precipitation must be examined in a meteorological/dynamical context [*Levin and Cotton*, 2008]. This is because, firstly, dynamical factors (e.g. relative humidity) may have a stronger effect on precipitation than a very large (five-fold) increase in CCN [*Givati and Rosenfeld*, 2004]. As discussed in Chapter 1, CCN activated from aerosol can either invigorate or suppress deep convective clouds, depending on dynamical factors such as relatively humidity [*Khain*, 2005], wind shear [*Fan et al*., 2009], etc. Secondly, as shown in many small- and regime-scale studies, a number of mechanisms induced by aerosol perturbations, including dynamical feedbacks, are able to absorb (or offset) some effects of aerosols, and hence, buffer the aerosol-cloud-precipitation system [*Stevens and Feingold*, 2009].

Focusing on different meteorological systems, many modeling studies all find that aerosol-induced changes in precipitation, when averaged over a large area and long time, are very small. For example, when examining the impacts of aerosols on tropical convections, *van der Heever et al.* [2011] shows that the aerosol indirect effect on

shallow cloud precipitation may offset the aerosol indirect effect on deep convection precipitation. *Igel et al*. [2013] shows that the precipitation associated with an aerosol-contaminated warm frontal system remains relatively constant because smaller cloud droplets enhance vapor deposition and decrease riming efficiency at the same time. *Seifert et al.* [2012] finds that the domain-averaged precipitation in modeling cases with different combinations of high/low CCN and IN concentrations remains relatively constant, because of three possible cloud buffering feedbacks: 1) liquid water content compensating suppressed rain formation, 2) mixed-phased processes compensating for suppressed rain formation, and 3) dynamic feedbacks compensating for microphysical feedbacks. The aforementioned studies motivate us to examine the impacts of smoke on clouds and precipitation under different CCN and IN regimes, which strongly depend on meteorological/dynamical conditions and fire regimes (smoke loading, smoke injection height, etc.).

Similarly, smoke radiative forcing must also be examined under different CCN and IN regimes. *IPCC AR5* [2013] reviews many GCM studies that estimate the total aerosol radiative forcing (radiative forcing due to aerosol-radiation and aerosol-cloud interactions). The results (as shown in Figure 7.19 in *IPCC AR5* [2013]) demonstrate that inclusion of the interaction between aerosols and mixed-phase and/or convective clouds in the models causes larger uncertainties in total aerosol radiative forcing and smaller negative values, mainly due to the effect of IN, which counteracts the effect of CCN.

The goal of this chapter is to examine the extent to which wildfire smoke can alter the microphysical properties of clouds, precipitation, and radiative fluxes under varying fire regimes and meteorological conditions. In order to achieve this goal, we study the

wildfires that occurred in the summer of 2002 in the Yakutsk region (central Siberia) by running the meso-scale model WRF-Chem-SMOKE version 3.3.1 in conjunction with satellite observations. To initiate the model, we prepare the hourly size- and composition-resolved smoke emissions based on a fire radiative power (FRP) technique [*Ichoku and Kaufmann*, 2005]. In the WRF-Chem-SMOKE model, smoke particles can function as CCN, IN, and SW absorbers. Therefore, the impacts of smoke on clouds and resulting precipitation via both microphysical and radiative pathways are considered in our study. The chapter is organized as follows: Section 4.2 describes the model configuration and data used in our study. The impacts of smoke on clouds and precipitation under different fire regimes and meteorological conditions are analyzed in Section 4.3, while the impacts on radiative fluxes are examined in Section 4.4. Chapter 4 is concluded in Section 4.5.

4.2 Model Configuration and Data

4.2.1 Description of the 2002 Siberia Wildfire Event and Model Configuration

A severe fire season occurred in Yakutsk, Russia, 2002. The fire season lasted for the entire August, and caused nearly 5 Mha of total burned area. In this Chapter, we use the fully-coupled WRF-Chem-SMOKE model, which is a modified version of the public WRF-Chem v3.3.1 model.

Figure 4.1 shows a model domain centered at the Yakutsk region. The domain includes 842 (west-east) by 362 (north-south) grids with the 5 km×5 km horizontal resolution. The model is set up with 37 vertical σ-levels. The simulation period is from August 1 to August 31, 2002, with a 20-second calculation time step and a 2-hour output frequency. FNL reanalysis data (http://rda.ucar.edu/datasets/ds083.2/) are used to initiate

the meteorological fields. In WRF-Chem-SMOKE, aerosols are fully coupled with cloud microphysics and radiation through coupling between the MOSAIC aerosol scheme [*Zaveri et al*., 2008], the microphysics Morrison two-moment scheme [*Morrison et al*., 2005], and the Goddard shortwave radiation scheme [*Chou et al.*, 1998]. Hourly size- and composition-resolved smoke emission flux rates are computed in a preprocessing package (Section 2.3.3). Given the information of smoke size distribution and composition, CCN and IN activations are modeled using the *Abdul-Razzak and Ghan* [2000] and *Phillips et al.* [2008] parameterizations, respectively, within WRF-Chem-SMOKE (Section 2.4.3). The number concentrations of activated cloud droplets (CDNC) and ice crystals are coupled with the Morrison two-moment microphysical scheme. We have modified the riming coefficient in the public version of the Morrison scheme by adopting the hydrometeor size-dependent riming coefficient, following the Thompson scheme [*Thompson et al*., 2004; *Morrison et al*., 2008].

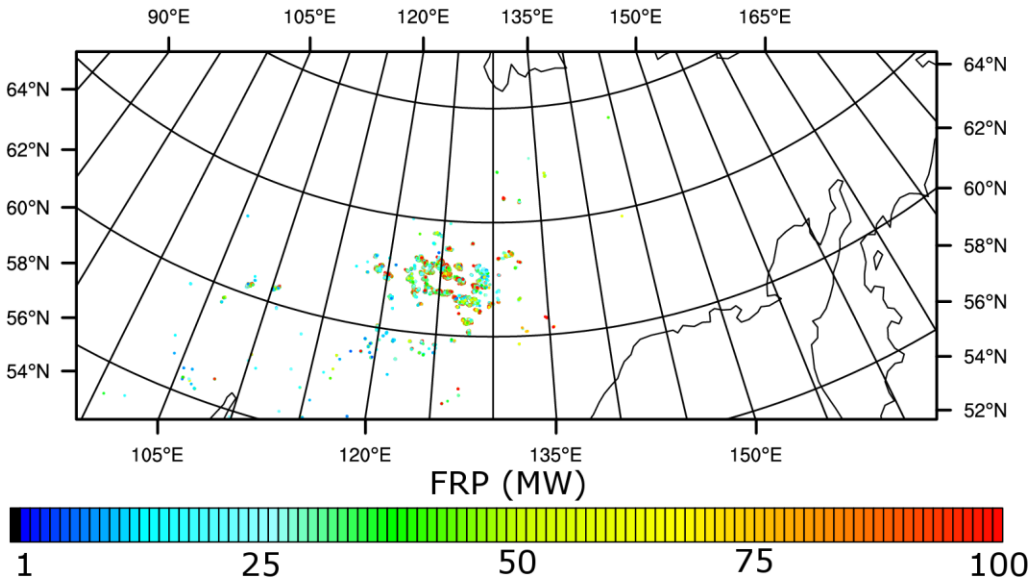

Figure 4.1: Model domain. The dots indicate the location of active fire detected by MODIS. The color of dots corresponds to the fire radiative power value of each active fire.

In our study, we compare a reference case (SMOKE) to a smoke-free case (CLEAN) to aid in the interpretation of smoke impact on cloud and precipitation. In the CLEAN case, we do not include the smoke emissions, but employ prescribed background CDNC and IN values. For CDNC, we set the value of 100 no./cc for the atmospheric layer with pressure higher than 850 hPa, and 50 no./cc for the layers with pressure lower than 850 hPa. The background number concentration of IN is based on in-situ measurements during the M-PACE campaign [*Verlinde et al*., 2007]. According to many modeling studies (e.g., *Morrison et al*. [2008], *Fridlind et al*. [2007]), however, the number concentration of IN measured during M-PACE is too low. Therefore, we use 10 times the in-situ measured value: 1.6 no./L for the background value of all heterogeneous ice nucleation. Activated CDNC and IN from smoke particles plus background values are used in the SMOKE case.

4.2.2 Aerosol, Cloud, and Radiation Data

In order to constrain the smoke plume simulation, we use several MODIS aerosol and cloud products, including aerosol optical depth (AOD), 10 km ×10 km level 2 collection 5, and cloud top temperature (CTT) product, 5km×5km level 2 collection 5. Our analysis reveals that very dense smoke plumes released during the Yakutsk wildfires can cause biases in AOD retrievals, especially in the smoke scenes with highest AOD values. Examining the MODIS retrieval algorithm, we find that some smoke pixels are misclassified as clouds. However, due to varying thermodynamic properties, smoke and clouds exhibit very different cloud top temperature (CTT). On this basis, we introduce a

threshold temperature (285K) to distinguish between misclassified smoke and actual clouds. This correction enables us to use both MODIS CTT and MODIS AOD in an integrative fashion, providing a more realistic characterization of the areal extent of smoke compared to MODIS AOD alone.

In our study, we compare modeled radiative fluxes against the Global Energy and Water Exchange (GEWEX)-Surface Radiation Budget (SRB) version 3.0 dataset. The SRB datasets are derived by two SW algorithms [*Pinker and Laszlo*, 1992, *Gupta et al*., 2001] and one LW algorithm [*Fu et al*., 1997] with cloud and radiance inputs from the International Satellite Cloud Climatology Project (ISCCP) and meteorological inputs from GMAO reanalysis dataset (http://gmao.gsfc.nasa.gov/). The SRB dataset provides radiative fluxes such as upward shortwave fluxes at TOA ($SW_{TOA}\uparrow$) and downward shortwave fluxes at the surface ($SW_{SFC}\downarrow$) every 3 hours at a spatial resolution of 1° × 1°.

4.3 Assessment of the Impact of Smoke on Clouds and Precipitation

4.3.1 Fire Regimes and Corresponding Meteorological Cconditions

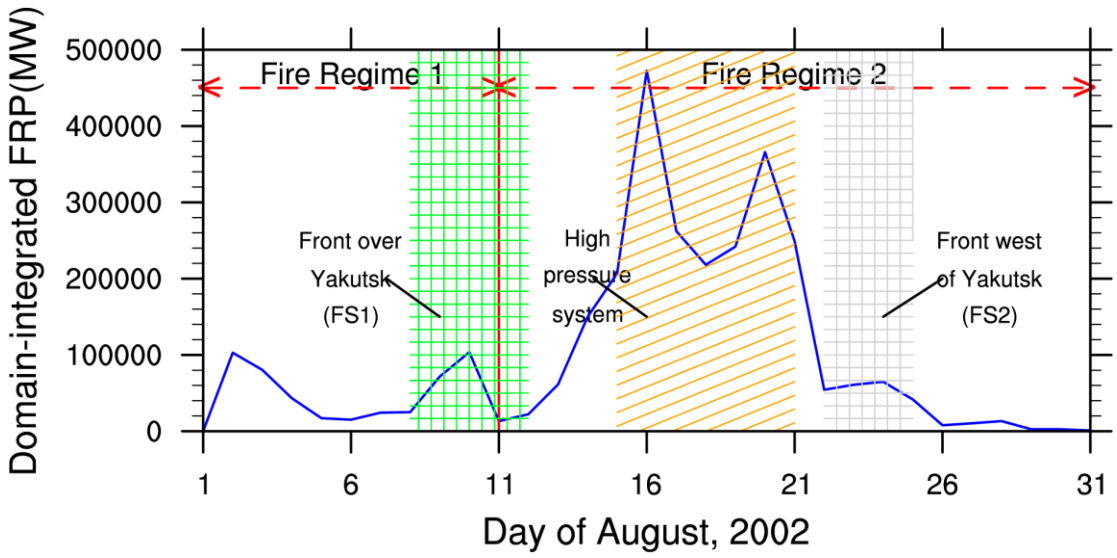

Figure 4.2: Variation of daily domain-integrated fire radiative power

Figure 4.1 shows the location of active fires detected by MODIS in August 2002 in the study domain. Most active fires during this period were concentrated around the Yakutsk region. Figure 4.2 shows the domain-integrated daily FRP for August 2002. The fire activities during the month of August can be generally characterized by two fire regimes. Fire regime 1 (FR1) is from 1-11 August, when a relatively small amount of smoke was emitted. Based on FNL re-analysis data (and modeling results), we can identify two frontal systems that passed over the Yakutsk region on 2-3 August and 9-10 August, respectively. Interestingly, these two systems corresponded well with the two peaks in FR1 as seen in Figure 4.2. This correlation may be explained by the relatively high surface temperature before the arrival of the frontal system (for example, the surface temperature over Yakutsk was higher than 27°C at noon local time on 9 August, which was much higher than the surrounding areas) or the lightning associated with the convective clouds in the frontal system. By 12 August, the second frontal system depleted much of the smoke emitted during the fire regime 1. As shown in the true color image Figure 4.3(a), this frontal system, referred to as frontal system 1 (FS1), is the focus of present study (section 4.3.2).

The second fire regime (FR2) starting on 12 August lasted until the end of August. On 14 August, a new frontal system passed over the Yakutsk region and ignited more wildfires. Then the wildfires spread due to a blocking high-pressure system, which caused dry, hot air to hover over the Yakutsk region from 15-21 August. As a result, a large amount of smoke was emitted. As shown in the MODIS true color image Figure 4.3(b), on 19 August, the edge of the blocking high-pressure system is actually weak enough for shallow convection to occur. On August 22, another early-stage frontal

system appeared in the northwest part of the study domain and began to interact with smoke emitted on previous days. This frontal system, referred to as frontal system 2 (FS2), is also the focus of present study (section 4.3.3).

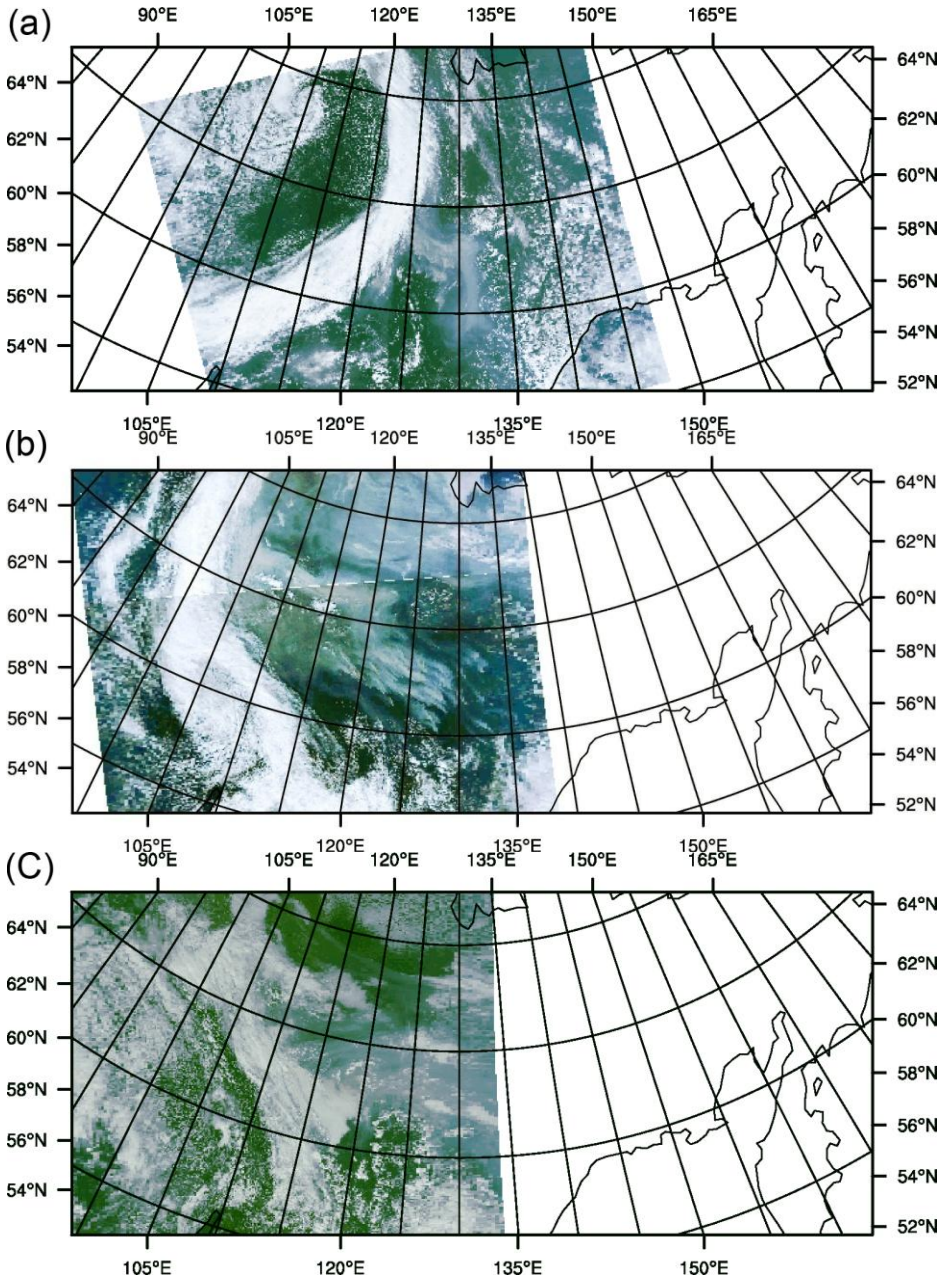

Figure 4.3: MODIS true color images for (a) 9 August 0410UTC; (b) 19 August 0445UTC; (c) 24 August 0505UTC.

4.3.2 The Impact of Smoke on Clouds and Precipitation during Fire Regime 1

4.3.2.1 Spatiotemporal Distribution of Smoke during Fire Regime 1

As demonstrated in [*Lu and Sokolik*, 2013b] or Chapter 4, the smoke loading has significant impact on cloud microphysical properties and the onset time of precipitation. Therefore, in this section (for FR1) and section 4.3.3.1 (for FR2), we study the major features of smoke plumes, compare the model outputs with the MODIS observations, and make sure both the spatial distribution and loading of smoke plume is not significantly biased.

Here we select several representative days for analysis. These days represent different meteorological and fire regime conditions: 9 August (wildfire ignition in FR1), 14 August (wildfire ignition in FR2), 19 August (wildfire spread under the influence of high-pressure system in FR2), and 23 August (wildfire decay in FR2). Modeled AOD fields are compared to composite field of MODIS AOD and CTT. Modeled optical properties of smoke particles at 400nm and 600nm, such as extinction and single scattering albedo, are first calculated by assuming a volume-averaged refractive index [*Fast et al*., 2006]. Then we calculated the AOD at 550 nm using an Angstrom exponent relationship and AODs at 400 nm and 600 nm following *Fast et al* [2006].

Figures 4.4 (a) and 4.4(b) show the composite field of MODIS AOD and CTT products and modeled smoke AOD for 0400UTC 9 August, 2002 (10 minutes time difference). The rainbow color bar represents values of retrieved or modeled AOD, while the light blue/pale yellow colors in Figure 4.4(a) indicate MODIS pixels with a CTT value lower or higher than 285K, respectively. As shown in Figure 4.4, smoke plume (pixels with high CTT) is transported to the north, and interacts with forward edge of FS1

at around 63°N. Examining modeled smoke AOD fields, we find that the WRF-Chem-SMOKE model reasonably captures the spatial distribution of smoke, especially the location where it interacts with FS1. As shown in the modeled AOD field on 9 August in Figure 4.4(b), many smoke particles, after swirled in FS1 at 63°N, are actually transported to the north within FS1. Around 130°E, 60°N, a cluster of MODIS pixels has the highest AOD values, which are around 2-4 near high CTT pixels. In the same region, the model produces a cluster with smaller size but higher AOD values of 5-6.

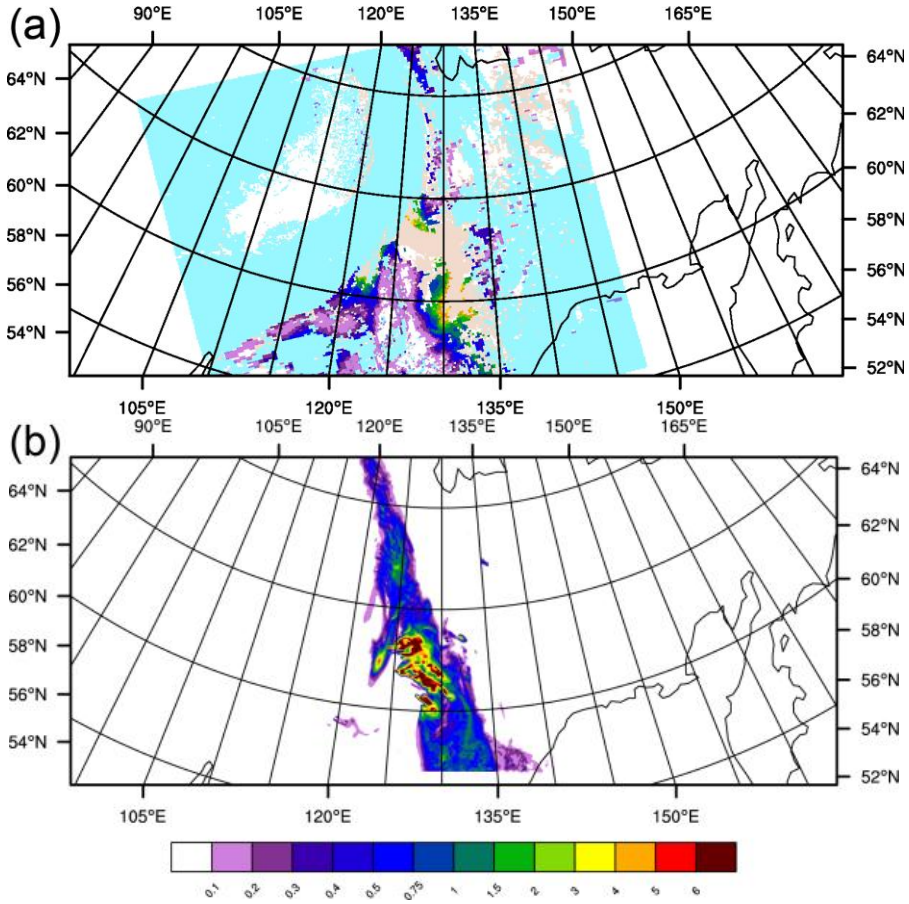

Figure 4.4: (a) A composite field of MODIS AOD and cloud top temperature for 0410UTC 9 August, 2002; (b) modeled smoke AOD field for 0400UTC 9 August, 2002.

4.3.2.2 CCN and IN Fields during Fire Regime 1

In order to aid in the interpretation of smoke-induced changes in microphysical properties, we first examine the column-integrated CDNC and IN fields. The results demonstrate that the spatial distributions of these two fields strongly depend on the how smoke particles are swirled into the frontal system.

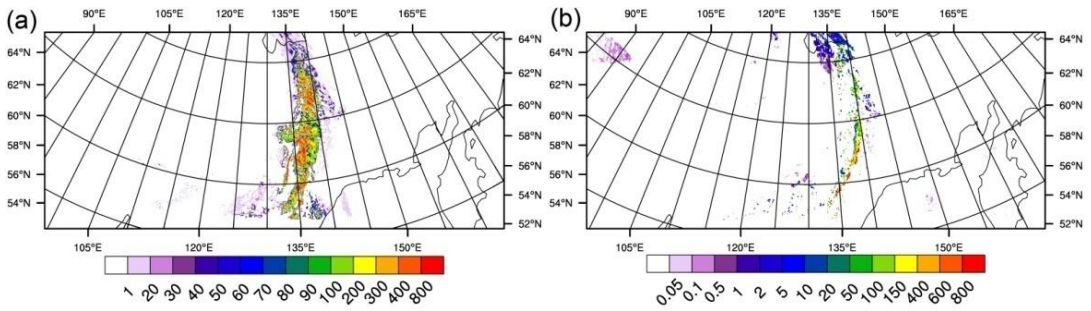

Figure 4.5: (a)Column-integrated activated CDNC (unit: 10^9 no./m2) for 0400UTC 10 August (b) column-integrated activated IN (unit: 10^4 no./m2) for the same period.

As shown in Figure 4.5, high CDNC and IN number concentrations are activated from smoke on 10 August. The activated CDNC field exists in the entire frontal system, with the maximum values of column-integrated CDNC ($>8\times10^{11}$ no./m^2) along the center axis of the frontal system (from north to south), while the maximum values of column-integrated IN ($>8\times10^6$ no./m^2) are located at the forward edge of FS1. Unlike CDNC, the IN concentration in the upper portion (>65°N) of FS1 is about ten times lower than that in the lower portion (<65°N) of FS1. This disparity primarily results from the relative position between the smoke plume and the frontal system. The day before, when the smoke particles first interact with the hydrometeors at the forward edge of the lower portion of FS1, a large fraction of them are activated as IN because the strongest updraft and the strongest supersaturation w.r.t. ice usually occur in this region (not shown). Then, as smoke particles are transported to the north within FS1, the majority of particles are

activated as CDNC. Thus, only a few of smoke particles are transported to the forward edge of the upper portion of FS1 and become IN. This strong dependency of CDNC and IN fields on the way the smoke plume interacting with the frontal system is also shown in section 4.3.3.2 for FR2.

4.3.2.3 Analysis of Smoke Induced-Changes in Cloud Microphysical Properties and Precipitation during Fire Regime 1

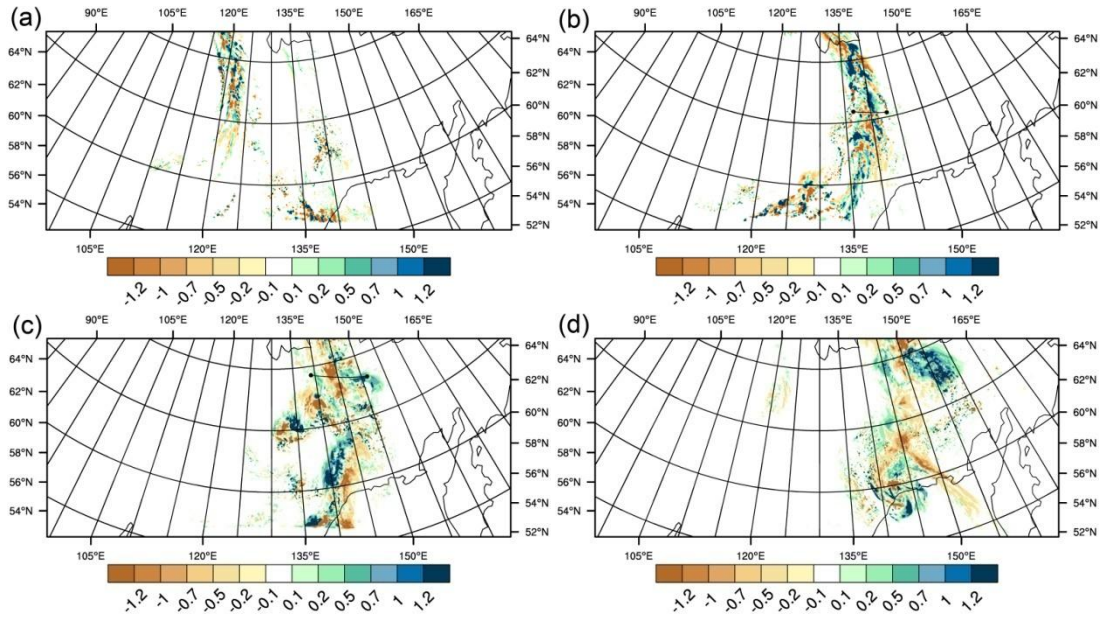

Figure 4.6: Differences in modeled total water path (TWP, kg/m^2) between SMOKE and CLEAN for (a) 9 Aug., (b)10 Aug.,(c) 11 Aug., and (d) 12 Aug. All snapshots are for 0400UTC

In this section, we examine the smoke-induced changes in 1) total water path (TWP), 2) cloud water content (CWC), rain water content (RWC), ice water content (IWC), and snow water content (SWC) along some cross-sections, and 3) daily precipitation during FR1.

Figure 4.6 shows the differences in modeled total water path (TWP) between SMOKE and CLEAN for 0400UTC 9~12 August. TWP is indicative of smoke-induced changes in the amount and spatial distribution of total cloudiness. We find that FS1 first interacts with the smoke plume on 8 August. On the next day as shown in Figure 4.6(a), the pattern of TWP difference field in FS1 becomes very noisy. In other words, the field is composed of many small-size clusters with either positive of negative differences (around ±1.2 kg/m^2). Here, the "cluster" is referred to as a group of contiguous model grids with entirely positive (or negative) TWP differences. It seems that on 9 August, the smoke only slightly changes the location and/or intensity of individual cloud cells. On 10 August, FS1 continues to develop and becomes even stronger. It passes over the Yakutsk region, depletes smoke, and carries less dense smoke plume to the east. Meanwhile, the clusters of model grids with either positive or negative TWP differences grow larger in terms of horizontal extent.

As shown in Figures 4.6(c) and (d), FS1 evolves into two parts: a sub-polar vortex above 63.5°N -65°N and a cyclone-frontal system moving to the mid-latitude on 11-12 August. Unlike the previous two days, the TWP difference fields (SMOKE - CLEAN) are mainly composed of a few clusters with large horizontal extents (the areas of clusters are around 2.5×10^4~1.2×10^5 km^2). In other words, the locations of large-scale cloud decks are altered, and the TWP difference fields exhibit a clear and organized spatial pattern. By comparing the locations of two sub-polar vortexes in two cases, we find that the sub-polar vortex in the SMOKE case appears further downwind than the one in the CLEAN case on 0400UTC 11 August. There are two possible explanations: either cloud decks in the SMOKE case move faster or they have a longer lifetime compared to

CLEAN (For the upper portion of FS1, the later explanation is correct as discussed below). The smoke-induced changes in TWP of the sub-polar vortex are mainly negative, suggesting a reduction of cloudiness. We also find that the averaged difference in TWP for the sub-polar vortex (above 63.5°N) is -0.032 kg/m^2 (we exclude the model grids with absolute values of TWP differences below 0.01 kg/m^2, hereinafter). The frontal system in mid-latitude (lower portion of FS1) has the pattern opposite to the sub-polar vortex. The frontal system in the SMOKE case appears further downwind than the one in CLEAN case, forming a dipole feature. As a result, the TWP difference field of FS1 for 0400UTC 11 August has an "X" shape (the "X" shape is more obvious during 2200UTC 10 August as shown in Figure 4.7).

On 12 August, compared to CLEAN, the SMOKE case produces higher TWP values (TWP difference > +1.2 kg/m^2) in many model grids in the sub-polar vortex. The averaged difference in TWP for the sub-polar vortex (the portion of cloud system above 65°N) is 0.072 kg/m^2. The lower portion of FS1 in the mid-latitude evolves into a cyclone on August 12. The horizontal extent of the cyclone in the SMOKE case is smaller, but it acquires a stronger low-pressure center (large positive changes in TWP), while in the CLEAN case, the cyclone had a larger radius and a stronger front.

We find that, from 0400UTC 10 August 10 to 0400UTC 11 August, the intensity of the frontal system becomes stronger. In addition, the horizontal extents of the clusters of positive/negative TWP difference increase from small scale (~2.5×10^3 km^2) to very large scale (~2.5×10^4 km^2). Why does the spatial scales of these clusters of positive/negative differences in TWP increase, and what are the effects of smoke in driving these changes? Examining the TWP differences every two hours (the frequency

of model output), we are able to track the upper portion of FS1 (sub-polar vortex) as it moves to northeast. Figure 4.7 shows the five snapshots of FS1 from 0400UTC 10 August to 0400UTC 11 August with 6-hour intervals. The magnitude of TWP differences keeps changing. For example, the frontal system weakens at 1000UTC 10 August, rebuilds its intensity between 1600UTC to 2200UTC 10 August, and reaches its maximum intensity at 0400UTC 11 August.

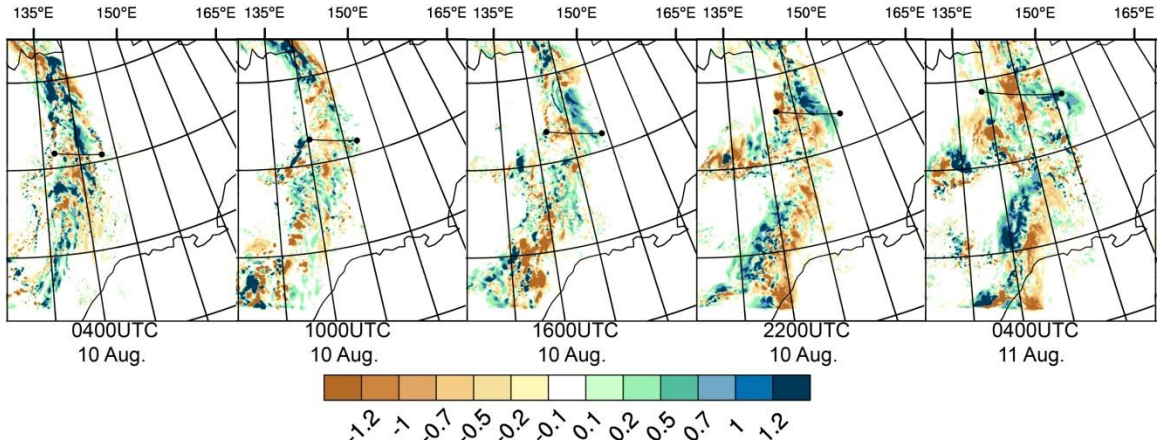

Figure 4.7: Differences in modeled total water path (TWP, kg/m^2) between SMOKE and CLEAN for 0400UTC, 1000UTC, 1600UTC, 2200UTC 10 Aug., and 0400UTC 11 Aug.

As shown in Figure 4.8, we track the upper portion of FS1 as it moves northeast, and examine smoke-induced changes (SMOKE-CLEAN) in the microphysical properties (CWC, RWC, IWC, and SWC) along the cross-section as labeled by the lines in Figure 4.7. The criteria employed to select these cross-sectional lines are as follows: first, TWP differences along these lines are large; and second, the lines should cover both positive and negative changes. We also superimpose the column-integrated CDNC and IN fields activated from smoke along the cross-sections to facilitate the interpretation of smoke-induced changes. In Figure 4.8, the X-axis represents the distance in km along these

cross-sections from west to east, while the Y-axis shows the altitude in km and the readings of column-integrated CDNC and IN in 10^{10} no./m^2 and 10^5 no./m^2, respectively. The SMOKE-CLEAN differences in CWC and IWC (unit: g/m^3 and dg/m^3) are shown in brown-green colors, while the differences in RWC and SWC (unit: g/m^3) are shown in purple-red colors. The column-integrated CDNC and IN are indicated by the solid lines. It should be noted that IN is treated diagnostically, so it represents the production rate of ice crystals and not the actual number concentration of ice crystals in clouds.

Figures 4.8(a) and (b) show the smoke-induced changes in cloud microphysical properties along the cross-section for 0400UTC 10 August. We find that the cloud system associated with FS1 covers a vast and continuous area along the cross-section. For example, the cloud system stretches from 80 to 210 km along the cross-section in the SMOKE case, whereas from 50 to 225 km in the CLEAN case (not shown). However, according to Figures 4.8(a) and (b), the differences in microphysical properties between two cases actually occur in small spatial scales (~20-30 km). A part of FS1 (50-150 km on the X-axis) is under the influence of high CDNC, which do not distribute uniformly along the cross-section. The maximum column-integrated CDNC along the cross-section in Figure 4.8(a) is higher than 6×10^{11} no./m^2. In this region, high CDNC activated from smoke particles cause 45% less rain water (Figure 4.8(a)) and 29% less snow water (Figure 4.8(b)) by mass in the SMOKE case than the CLEAN case. Meanwhile, the modeled CWC and SWC in the CLEAN case reside in higher altitudes in the same region, likely due to more latent heat release. This contrast indicates that the portion of the cloud system around 50-150 km on the X-axis in the CLEAN case is in a more mature stage than those in the SMOKE case. At 150 km on the X-axis, more SWC

appears in the CLEAN case as shown in Figure 4.8(b). In the same region, a relatively small amount of column-integrated IN indicates that ice-phase hydrometeors will be formed later in the SMOKE case. At the forward edge of FS1 around 150-225 km on the X-axis, the SMOKE case predicts more ice water at 3-4.5 km above ground. Very likely, this layer of IWC is formed from heterogeneous IN because temperature of this layer is warmer than the onset temperature for homogeneous ice nucleation and colder than the onset temperature of ice multiplication. As a result, more IWC in the SMOKE case leads to 28.6% more snow water by mass at the forward edge of FS1 compared to the CLEAN case. In addition, a weak precipitation event with a small amount of RWC from melting snow (maximum value of 0.24 g/m^3) can be seen in the SMOKE case. In the CLEAN case, the cloud layer at the forward edge of FS1 is close to its dissipating stage, because of a large amount of precipitation as RWC (maximum value of 0.48 g/m^3).

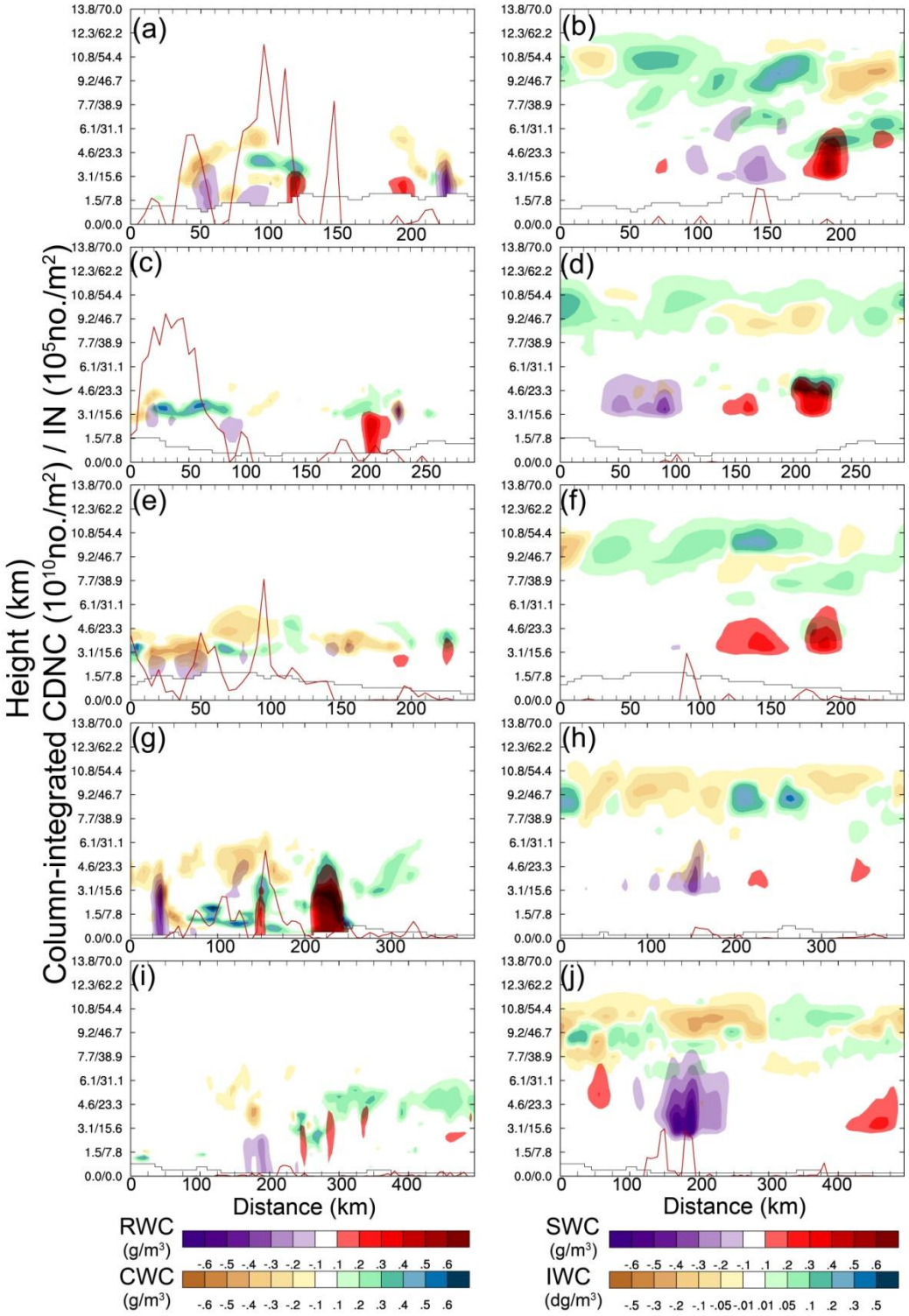

Figure 4.8: Smoke-induced changes in microphysical properties (SMOKE-CLEAN) along cross-sections from 0400UTC 10 August to 0400UTC 11 August with 6-hour intervals (top-bottom). Left column: differences in CWC (g/m^3, brown-green), RWC (g/m^3, purple-red), and column-integrated CDNC; right column: difference in IWC (dg/m^3, brown-green), SWC (g/m^3, purple-red), and column-integrated IN.

Six hours later, FS1 becomes weaker in terms of intensity and TWP. The large-scale cloud system in both the SMOKE and CLEAN cases breaks into several cloud cells with smaller sizes around 20-50 km as shown in Figures 4.8(c) and (d). Meanwhile, the maximum value of column-integrated CDNC reduces from 6×10^{11} no./m^2 to 4×10^{11} no./m^2, but the CDNC distribution becomes uniform as shown in Figure 4.8(c). At the same time, a small concentration of IN is formed in this region as shown in Figure 4.8(d). At 0-100 km along the X-axis, almost no RWC and SWC are formed in the SMOKE case. This result most likely are owing to the presence of high concentrations of CDNC that suppresses the collision-coalescence and riming processes. As a result, the water content is "trapped" in a thin but very dense layer of CWC (maximum value: 0.84 g/m^3). In contrast, a layer with SWC (maximum value: 0.42 g/m^3) and RWC (maximum value: 0.16 g/m^3, from melting snow) can be observed in the CLEAN case. This suggests that the cloud system at 0-100 km on the X-axis in the CLEAN case is in a more mature stage than the one in the SMOKE case. Around 200-225 km on the X-axis (the forward edge of FS1), the values of column-integrated CDNC are low. In the same region, the SMOKE case produces a small-scale cloud system that precipitates heavily, which indicates the cloud system is its mature stage. In contrast, the CLEAN case produces a cloud cell in its dissipating stage. Given its very small spatial scale, this cloud cell will likely disappear soon. This suggests that the cloud system at the forward edge of FS1 predicted by the SMOKE case has longer lifetime than the one predicted by the CLEAN case. Another difference between the two cases at the forward edge of FS1is that a moderate amount of SWC originating from heterogeneous ice nucleation occurred only in the SMOKE case.

Figures 4.8(e) and (f) show the differences in cloud microphysical properties between SMOKE and CLEAN for 1600UTC 10 August. The cloud droplets activated from smoke particles are significantly consumed, but the column-integrated concentrations are still high enough to suppress the formation of RWC at 50-125 km along the X-axis. In contrast, a layer of RWC with a large horizontal extent but a small magnitude (maximum value: 0.20 g/m^3) is formed in the CLEAN case at 10-80 km on the X-axis. At the forward edge of FS1 (around 125-200km on the X-axis), the CLEAN case predicts a thin layer of CWC and a small amount of RWC 3 km above the ground. In the SMOKE case, the relatively high IN concentration (1.5×10^6 no./m^2) at 100 km along the X-axis indicates the formation of ice-phase hydrometeors, which are adjacent to a pre-existing layer with a moderate amount of SWC (maximum value of 0.34 g/m^3). At the forward edge of FS1, only the SMOKE case produces a significant amount of SWC. This is probably not due to the difference in cloud developing stages as 6~12 hours ago shown in Figures 4.8(a-d). For example, we find that, the cloud layers in both cases do not reach the mature stages, because no precipitation is formed. However, more SWC production in SMOKE is very likely due to the fact that the riming process is no longer suppressed under relatively low CDNC condition (125-200 km on X-axis), and relatively more IN (100 km on X-axis) increases the onset temperature of ice crystal formation.

The differences in cloud microphysical properties along the cross sections at 2200UTC on 10 August 10 and at 0400UTC on 11 August are shown in Figures 4.8(g-h) and Figures 4.8(i-j), respectively. After 2200UTC 10 August, the upper portion of FS1 gains more convective energy and develops into a large-scale continuous cloud system with large water content. During this period, the magnitude of column-integrated CDNC

reduces from a relatively small amount (maximum value: ~3×10^{11} no./m^2) to a negligible amount (maximum value: ~3×10^{10} no./m^2) because cloud droplets are nearly consumed by transferring to other hydrometeors such as rain and snow. Moreover, smoke particles are nearly removed by precipitation, which results in less newly activated CDNC than before. This indicates that the effect of smoke as CCN becomes very small, yet as shown in Figure 4.7, the spatial scales of the TWP (cloudiness) difference fields become even larger than previous 6~18 hours. In previous 6~18 hours as shown in Figures 4.8(a-e), smoke particles significantly alter the cloud microphysical properties in terms of water phase, water content, and cloud lifetime/developing stage, but the locations of corresponding cloud systems in two cases are generally close or adjacent to each other. From 2200UTC 10 August 10 to 0400UTC 11 August, however, the entire cloud systems predicted by two cases locate in two different regions. Especially during 0400UTC 11 August as shown in Figure 4.8(i-j), the cloud systems in the two cases distance from each other for about 50 km.

In addition to the displacement of cloud systems discussed above, the life cycles of the cloud systems in SMOKE and CLEAN are not at the same stage as shown in Figure 4.8(g-j). Because of relative low concentration of CDNC at 2200UTC on August 10, the warm-rain process in SMOKE, unlike previous 18 hours, is actually invigorated. As shown in Figure 4.8(g), SMOKE produces a large amount of RWC with a maximum value higher than 1 g/m^3, which also becomes heavy precipitation falling over a vast region from 210 to 250 km along the X-axis. As an indicator of the dissipating stage of the cloud system in SMOKE, this strong precipitation event in the SMOKE case depletes the moisture in the atmosphere and consumes the convective energy. For example, Figure

4.9 shows the MCAPE fields (the maximum convective available potential energy of each model column, two-dimensional) for both CLEAN and SMOKE during 0400UTC 11 August. The CLEAN case produces much higher MCAPE values near the upper portion of FS1 than the SMOKE case in terms of their maximum values (893 KJ/kg vs. 690 KJ/kg) and horizontal extents (the number of model grids with MCAPE values higher than 300 KJ/kg: 1636 vs. 1260). As a result, a very strong cloud system develops in the CLEAN case at 0400UTC on 11 August, as shown in Figures 4.8(i-j). This system has a horizontal extent of 100 km, a vertical extent higher than 8 km (the top of cloud layer with SWC larger than 0.1 g/m^3), and a large amount of SWC with a maximum value of 0.8 g/m^3. This system is precipitating in the form of a relatively small amount of RWC. Therefore, we conclude that the cloud system in the CLEAN case is in its near-mature stage, whereas the cloud system in the SMOKE case is still in its early developing stage due to more CWC and less SWC (maximum value of 0.2 g/m^3). Notably, high IN number concentrations are activated from 120 to 200km along the X-axis, where locates the large-scale cloud system produced by the CLEAN case. This suggests that the SMOKE case will also produce more ice-phase hydrometeors in the same region later. Indeed as shown in Figure 4.6(d), in the upper portion of FS1, the SMOKE case predicts a cloud system with stronger intensity and more TWP and SWC (not shown) than the CLEAN case at 0400UTC on 12 August.

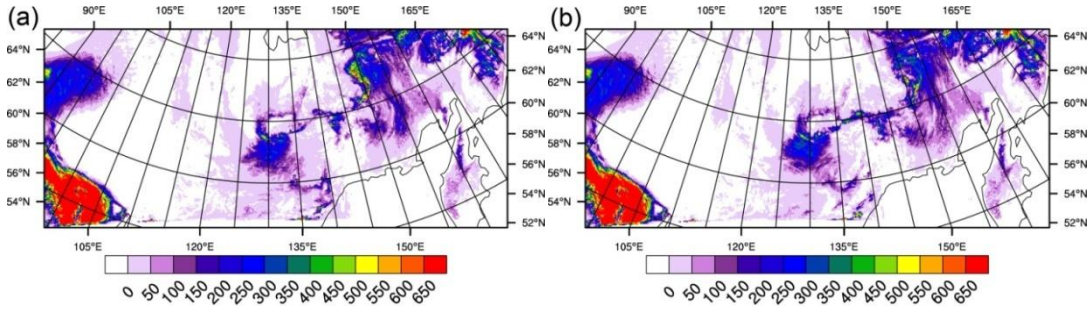

Figure 4.9: MCAPE (maximum convective available potential energy of each model column, KJ/kg) for 0400UTC 11 August (a) for the CLEAN case and (b) for the SMOKE case.

The changes in microphysical properties (shown in Figures 4.6-4.8) and large-scale dynamics (namely large-scale moisture and convective energy, shown in Figure 4.9) also significantly alter the spatiotemporal distributions of precipitation. Figure 4.10 shows the differences in daily precipitation between SMOKE and CLEAN from 10 to 12 August. Apparently, the daily precipitation difference fields are directly related to the differences in cloudiness (TWP) (Figure 4.6). As shown in Figure 4.10(a), the daily precipitation difference field in the lower portion of FS1 exhibits a noisy pattern on 10 August. The area-integrated precipitation (calculated by averaging all model grids with values larger than 0.01mm/day over a certain region, like the lower or upper portion of FS1, hereinafter) of this region (115°E-150°E, <65°N) is suppressed by smoke. On 11 August, both SMOKE and CLEAN predict a large precipitation band in the lower portion of FS1, stretching from north to south as shown in Figure 4.10(b). The precipitation band in the CLEAN case lies parallel to one in the SMOKE case, and appears 150km further downwind. The largest differences in precipitation are around ±25mm/day. On 12 August, SMOKE predicts more precipitation in the low-pressure center of the cyclone, while the CLEAN case produces more precipitation along the outer frontal system as

shown in Figure 4.10(c). The differences in precipitation of majority model grids are within ±10 mm/day.

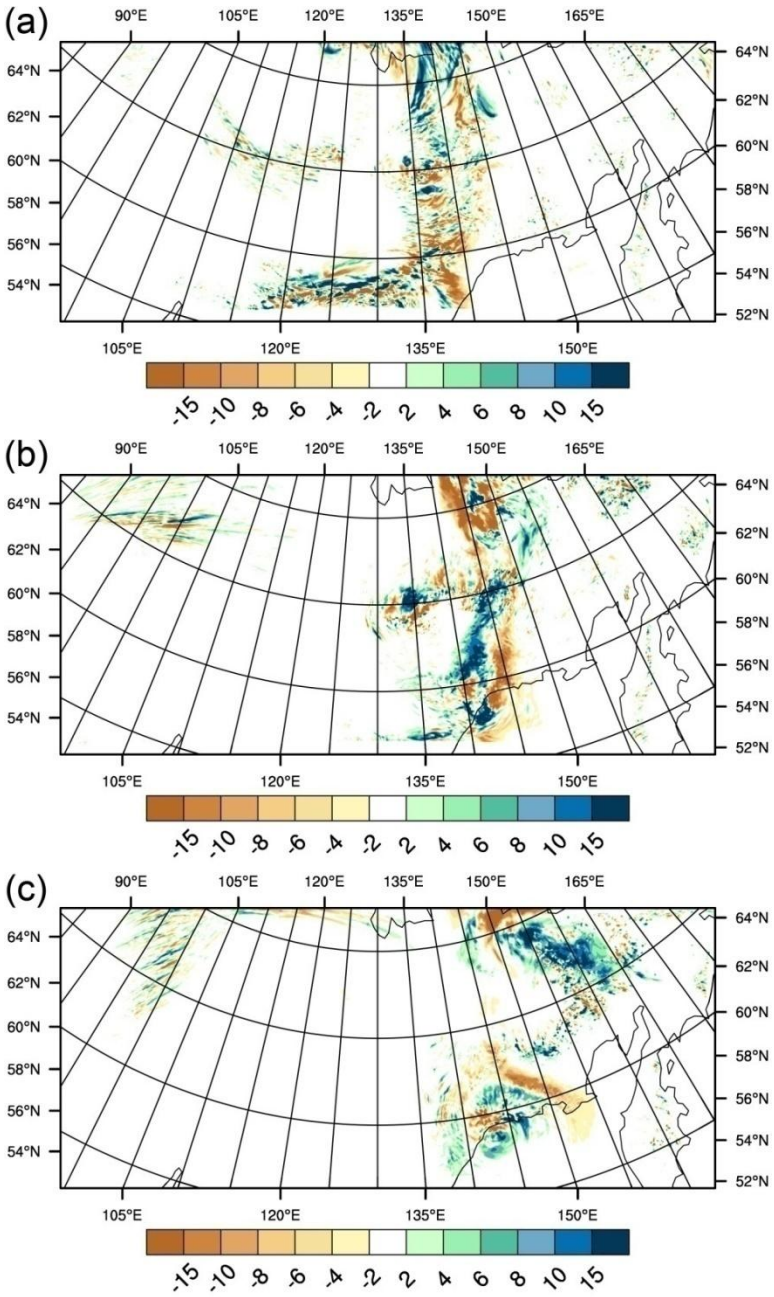

Figure 4.10: Differences in daily precipitation between SMOKE and CLEAN (mm/day): (a) for 10 August; (b) for 11 August; (c) for 12 August.

In the upper portion of FS1, the daily precipitation difference field exhibits a dipole feature near 65°N~70°N, 140°E~150°E on 10 August. This feature is actually

captured in the analyses of microphysical properties along the cross-sections as shown in Figures 4.8(c-h): the SMOKE case produces more precipitation downwind compared to the CLEAN case, because the cloud systems in SMOKE acquire longer cloud lifetimes. The largest positive and negative differences in daily precipitation between SMOKE and CLEAN in this region are 40 mm/day and -51 mm/day, respectively. Overall, the area-averaged daily precipitation associated with this dipole feature (65°N~70°N, 140°E~150°E) is slightly suppressed by -0.47 mm/day on 10 August. After 10 August, because of the noted significant smoke-induced changes in large-scale dynamics and microphysical properties, precipitation fields of the sub-polar vortex predicted by two cases show significant differences. Due to the weaker convective energy and less RWC and SWC formations in SMOKE, precipitation in the sub-polar vortex is strongly weakened, with a maximum negative difference of -63 mm/day on 11 August as shown in Figure 4.10(b). The difference in area-averaged daily precipitation for the sub-polar vortex (above 65°N, between 135°E~155°E) is -2.04 mm/day. As shown in Figure 4.10(c), precipitation in the SMOKE case is enhanced compared to the CLEAN case on 12 August, with a maximum positive difference of 56.6 mm/day. The difference in area-averaged daily precipitation for the sub-polar vortex (above 65°N, between 145°N~170°N) is 1.32 mm/day.

4.3.3 The Impact of Smoke on Clouds and Precipitation during Fire Regime 2

4.3.3.1 Spatiotemporal Distribution of Smoke during Fire Regime 2

During FR2, the fire activities in Yakutsk last much longer, emit much more smoke particles than FR1. The wildfires during FR2 are first ignited on 12 August when a new frontal system are coming from the west. Two days later on 14 August, the smoke

plumes originating from the fires ignited on 12 August locate around 120°E~130°E. As shown in the composite field of MODIS AOD and CTT on 14 August (Figure 4.11(a)), the major plume is transported to the north, and a large portion of the smoke plume is classified by MODIS as cloud with high CTT. The rest portion of the smoke plumes is retrieved as aerosols pixels with AOD values around 1-3. The model accurately reproduces both the spatial distribution and AOD values of this major smoke plume as shown in Figure 4.11(b). A smoke plume with smaller spatial scale can be seen along the frontal system, which is indicated by the light blue color in Figure 4.11(a). The model successfully reproduces the portion of this plume between 115°E~120°E with AOD around 0.5 but fails to reproduce the portion between 110°E~115°E with AOD around 1-3. Given by its location and magnitude, this small smoke plume may originate from some wildfires with short fire durations in the west of Yakutsk. The MODIS failed to detect these active fires, most likely due to the coarse temporal resolution of MODIS or due to cloud contamination.

As previously mentioned, the blocking high-pressure system with hot and dry air over the Yakutsk region causes more wildfires and extreme smoke emissions after 15 August. This system also blocks any efficient wet-removal process, such as precipitation associated with frontal systems. As a result, the smoke particles are suspended in the atmosphere for a long time. The smoke AOD field peaks around 19-20 August. When examining the observed and modeled smoke plumes on August 19 as shown in Figure 4.11(c) and (d), we find that 1) the major smoke plume is first transported northwest and then to the east, along the edge of the persisting high-pressure system, and 2) the model perfectly reproduces AOD values and spatial patterns of the smoke plumes. In the regions

where the model predicts the highest value of AOD around 2~6 (62°N-65°N, 115°E-130°E), MODIS classifies the pixels in the corresponding regions as clouds with high cloud top temperature. The MODIS AODs in the smoke plume around 67°N-70°N, 130°E-135°E are about 1-3, which agrees with the model simulations very well as shown in Figure 4.11(d).

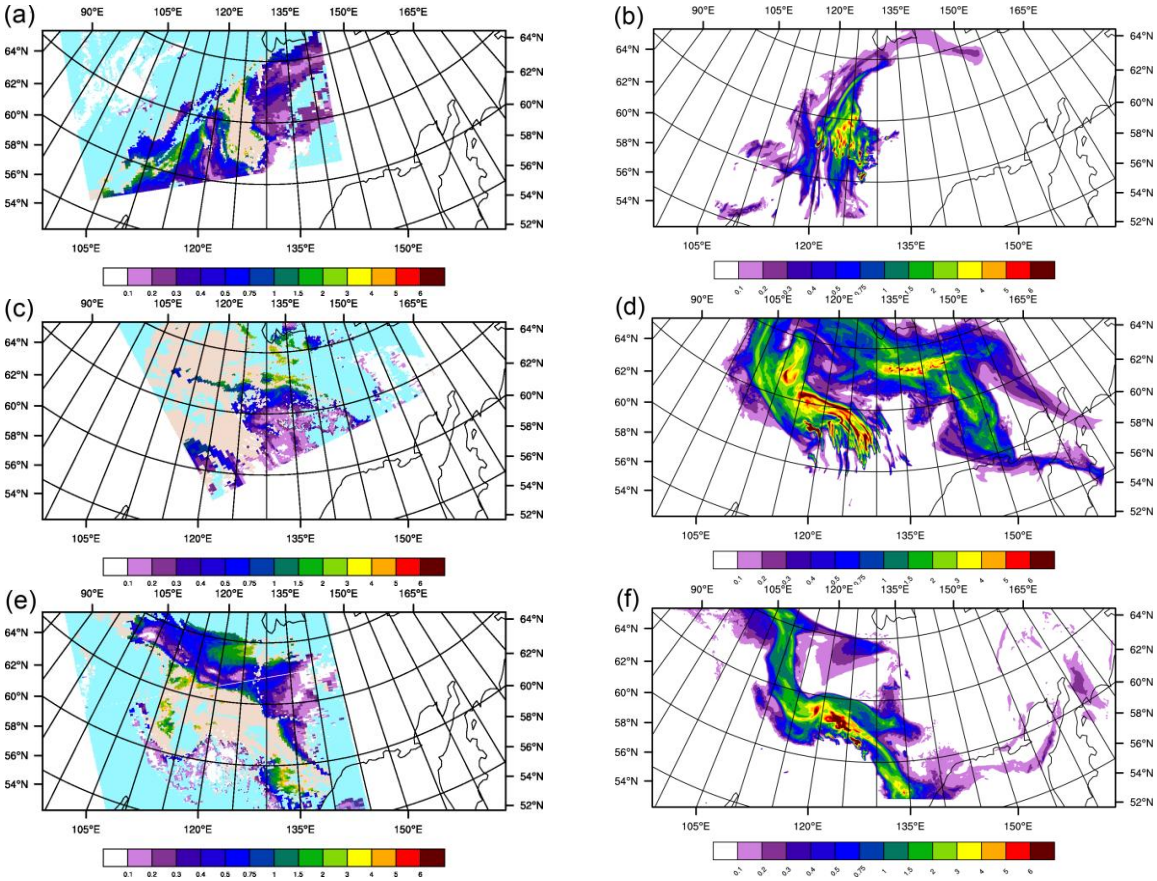

Figure 4.11: (a) MODIS AOD and cloud top temperature products for 0430UTC 14 August 2002; (b) modeled smoke AOD for 0400UTC 14 August 2002.(c) MODIS AOD and cloud top temperature products for 0310 UTC 19 August 2002; (d) modeled smoke AOD for 0400UTC 19 August 2002.(e) MODIS AOD and cloud top temperature products for 0420UTC 23 August 2002; (f) modeled smoke AOD for 0400UTC 23 August 2002.

On 22 August, the fire activities of FR2 suddenly weaken, and the domain-integrated emission amount decreases dramatically as shown in Figure 4.2. This is likely

caused by the breakdown of the blocking high-pressure system. After 22 August, a polar-frontal system at around 70°N and FS2 coming from the western edge of the domain begin to deplete smoke. As shown in the observed and modeled smoke plumes on 23 August (Figures 4.11(e) and (f)), the horizontal extent of smoke plume shrinks substantially compared to the previous days, while the portion of smoke plume to the east of 135°E is nearly depleted. Importantly and in contrast to FS1, the entire forward edge of FS2 between 68°N and 55°N is contaminated by smoke. Compared to the MODIS observations, the model performs reasonably well in simulating the spatial patterns of the smoke plumes, although the horizontal extent appears to be a little underestimated. MODIS retrieved AOD values in three regions (60°N-65°N, 110°E-115°E; 56°N-60°N, 130°E-135°E; 67°N-70°N, 117°E-127°W) are around 1-3. The model successfully captures the AOD values in the first two regions, and underestimates AOD values by a half in the third region.

4.3.3.2 CCN and IN Fields during Fire Regime 1

Figures 4.12(a-b) and 4.12(c-d) show the CDNC and IN fields activated from smoke on 24 and 25 August, respectively. Here we focus only on the CDNC and IN fields within FS2, which stretches from 70°N, 95°E to 58°N, 120°E on 24 August. At 0400UTC on 24 August, the maximum values of CDNC ($>8\times10^{11}$ no./m^2) and IN (1.5×10^{6} no./m^2) fields reside along the forward edge of FS2 as shown in Figure 4.12 (a-b). 24 hours later, more CDNC and IN are activated because the smoke plume is well mixed with the frontal system as shown in Figure 4.12 (c-d). The CDNC field in FS2 has a smaller horizontal extent, when compared with FS1, because of the weaker intensity of FS2. The maximum value of column-integrated IN in FS2 is lower than that in FS1;

however, the IN field in FS2 is more homogeneously distributed along the frontal system between 62°N~67°N. The IN concentration below 62°N is two orders of magnitude lower than the IN concentration around 62°N~67°N.

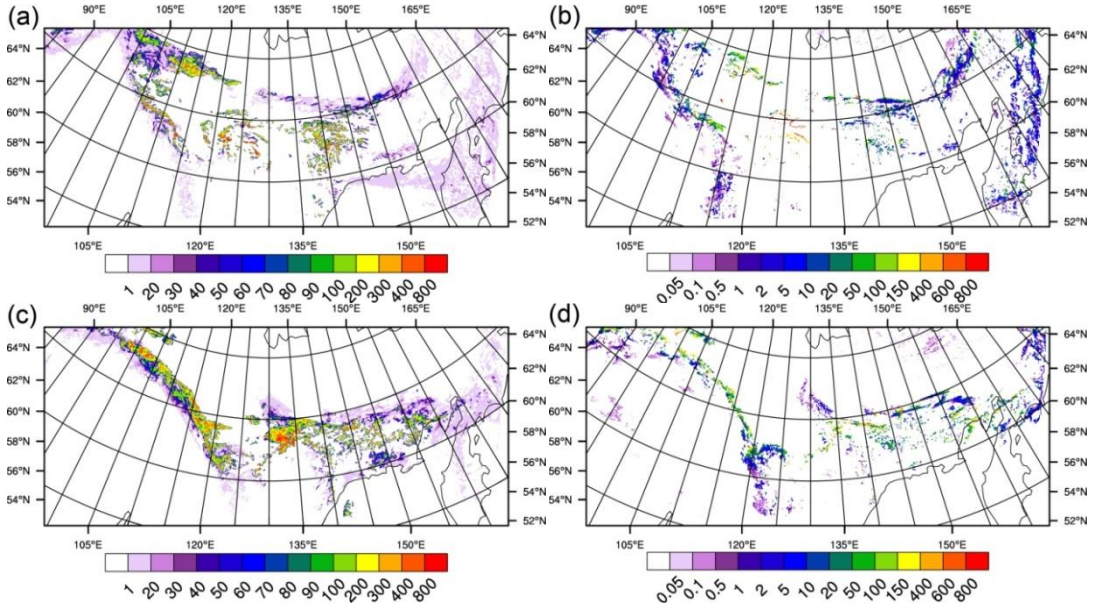

Figure 4.12: (a) and (b) Column-integrated activated CDNC (unit: 10^9#/m^2) IN (10^4#/m^2) for 0400UTC 24 August; (c) and (d) the same as (a) and (b), but for 0400UTC 25 August.

4.3.3.3 Analysis of Smoke Induced-Changes in Cloud Microphysical Properties and Precipitation during Fire Regime 2

In this section, we examine the development of FS2 and address the smoke-induced changes in the cloud microphysical properties and precipitation associated with FS2. As discussed above, the smoke-cloud interaction in FS2 differs from FS1 in two main ways. First, in FS2, a much larger quantity of smoke is emitted and suspended in the atmosphere. Second, FS2 is relatively weak in intensity. As a result, smoke particles are able to penetrate and mix well with the entire frontal system along its forward edge.

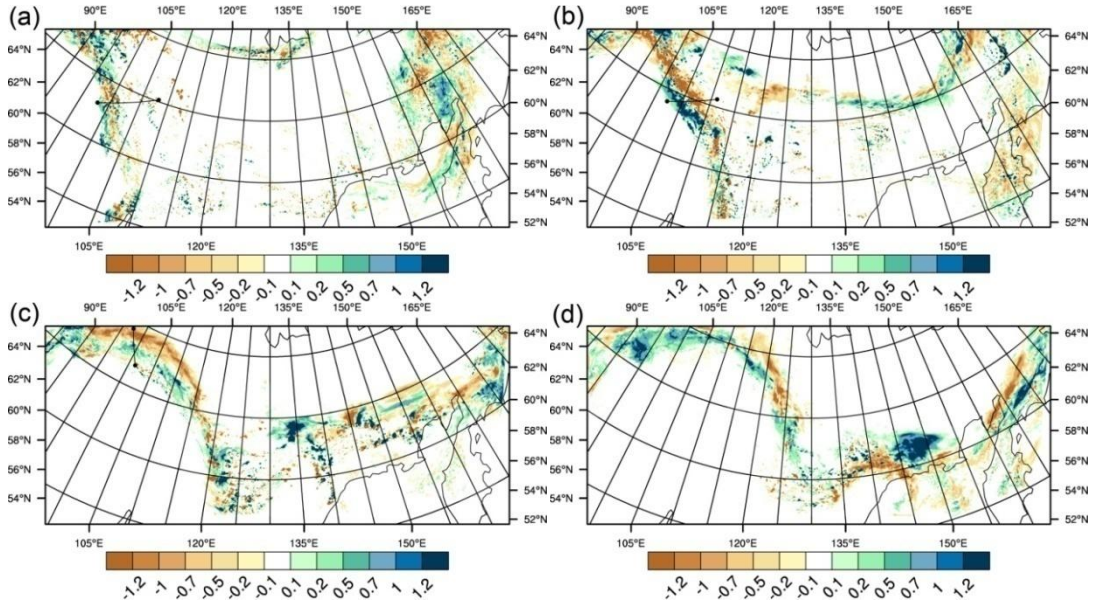

Figure 4.13: Differences in modeled total water path (TWP, kg/m^2) between SMOKE and CLEAN for (a) 23 Aug., (b)24 Aug.,(c) 25 Aug., and (d) 26 Aug. All snapshots are for 0400UTC

On 22 August, FS2 enters the study domain from the west, and starts to interact with smoke. Figure 4.13 shows the differences in TWP between SMOKE and CLEAN in the following days (23-26 August). After the smoke contamination, the TWP difference field associated with FS2 are composed of many small-size clusters with positive/negative differences on 23 August as shown in Figure 4.13(a). This pattern is similar in nature to the TWP difference field on 9 August as shown in Figure 4.6(a), except that the magnitude of TWP differences on August 23 is smaller (< 1 kg/m^2). On 24 August, FS2 grows significantly in terms of its vertical development. Large amounts of ice-phase hydrometeors are also formed within FS2. Meanwhile, the small-size clusters of TWP differences quickly organize into a dipole feature as shown in Figure 4.13(b): the location of the entire FS2 predicted by the two cases shifts in parallel to one another. FS2 in the CLEAN case appears further downwind compared to the one in

SMOKE. The distance between the forward edges of FS2 in two cases is about 100~150 km. In addition, the magnitudes of TWP differences increase compared to the previous day (> ±1.2 kg/m^2). In FS2 above 62°N, the parallel dipole pattern of TWP differences remains for the next two days as shown in Figure 4.13(c-d). However, the portion of FS2 below 62°N in the SMOKE case appears further downwind compared to the one in the CLEAN case. After 25 August, the amount of TWP in FS2 rapidly decreases, especially in the SMOKE case, because of a strong precipitation event occurred on 24 August (as discussed below). By 0400UTC 27 August (not shown), the entire frontal system completely dissipates and dies off.

By comparing the smoke-induced changes in TWP of FS1 (Section 4.3.2) and FS2 (Section 4.3.3), we are interested in answering this question: whether and how the smoke-induced changes in cloud microphysical properties in these two storm systems differ. An examination of the smoke-induced changes in CWC, RWC, IWC, and SWC along the cross-sections shown in Figure 4.14 provides some answers to the question. The locations of cross-sections are labeled in Figure 4.13.

Figures 4.14(a) and (b) show the differences in cloud microphysical properties along the cross-section for 0400UTC 23 August. FS2 is relatively weak at this time since it only has small amounts of ice-phase hydrometeors, as shown in Figure 4.14(b). Moreover, FS2 (either in SMOKE or in CLEAN) is consisted of a few convective cells with a horizontal spatial-scale of about 10~20 km. Several cloud cells in the SMOKE cases (at 40, 190, and 400 km along the X-axis) contains 14.4% less rain water by mass, and moves slightly slower than the corresponding ones in the CLEAN case (at 60, 200, 475 km along the X-axis). The slower movement in the SMOKE case is most likely due

to higher CDNC, which suppress the development of cloud cells. However, additional cloud cells with rainfall are produced in the SMOKE case, such as the one at 125 km along the X-axis shown in Figure 4.14(a). Along the cross-section, the SMOKE case produces slightly less rain water (4.3% by mass) than the CLEAN case.

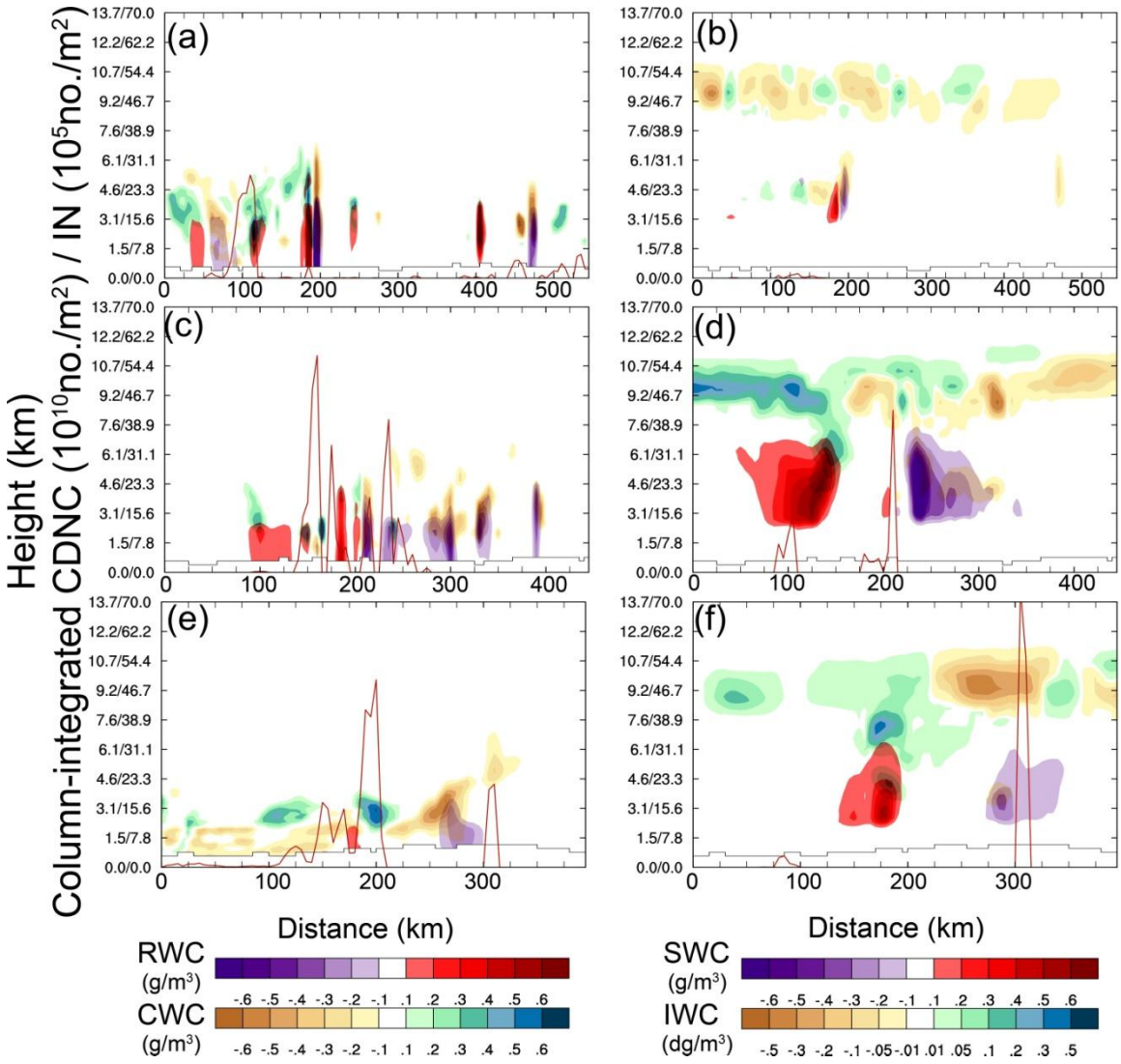

Figure 4.14: Same as Fig. 4.8, except (a) and (b) for 0400UTC 23 August, (c) and (d) for 0400UTC 24 August,(e) and (f) for 0400UTC 25 August.

As discussed before, FS2 strengthens by 0400UTC 24 August, as shown in Figures 4.14(c)and (d). Its strong vertical development also promotes the activation of

CDNC and IN. The maximum value of column-integrated IN in FS2 is around 4.5×10^6 no./m^2, much higher than that in the upper portion of FS1. Along the cross-section, the SMOKE case produces 48.4 % less rain water by mass compared to the CLEAN case. This is probably due to more CDNC activation, which suppresses the collision-coalescence process. In addition, cloud droplets in the SMOKE case do not reach altitudes as high as in the CLEAN case. In other words, the mixed-phase cloud region in SMOKE is shallower, which is most likely related to more IN activation, which quickly transfers liquid-phase hydrometeors into cloud ice and snow categories. As shown in Figure 4.14(d), the SMOKE case predicts a layer with a fairly large IWC (0.1~0.2 dg/m^3) under 7.6 km. Since the temperatures associated with this IWC layer are between -8°C ~ -30°C, we believe the ice crystals in this layer mainly originate from the heterogeneous ice nucleation. More ice crystals promote the formation of snow. Consequently, total mass of snow water in the SMOKE case is 4% higher than the CLEAN case along the cross-section. Because of the competing effects of CDNC and IN, the cloud lifetime and moving speed of FS2 are very likely less affected compared to the upper portion of FS. Therefore, two frontal systems in SMOKE and CLEAN move in parallel. Given the fact that the cloud cells in SMOKE move slower than those in CLEAN during the previous day as shown in Figures 4.14(a) and (b), the frontal systems in two cases locate in entirely different regions by 0400UTC 24 August, and the one in the CLEAN case locates further downwind as shown in Figures 4.14(c) and (d). This shift in location is in accord with the parallel dipole feature seen in the TWP differences in Figure 4.13(b).

Smoke-induced changes in the microphysical properties for 0400UTC 25 August are shown in Figures 4.14(e) and (f). For 0400UTC 25 August, snow water in the

SMOKE case is slightly reduced by 13% along the cross-section, while the other changes in microphysical properties are very similar to the previous day (56% less rain water by mass, shallower mixed-phase region, large amounts of ice crystals from heterogeneous IN).

Figure 4.15 shows daily precipitation differences between the SMOKE and CLEAN cases on 24-25 August. The daily precipitation difference field on 24 August exhibits a large-scale dipole feature, which is in agreement with the TWP difference field between SMOKE and CLEAN on the same day. The precipitation band in the CLEAN case locates further downwind compared to that in the SMOKE case. The difference in area-averaged daily precipitation for FS2 (<120°E, >60°N) is only -0.42 mm/day. However, when examining the model grids with only positive or negative changes, we find the area-averaged daily precipitation at large magnitudes of 4.77 mm/day and -5.23 mm/day, respectively. These modeling results imply that smoke has a small effect on the total daily precipitation amount in FS2, but a significant effect on the precipitation redistribution. Compared to the previous day, precipitation in the upper portion of FS2 (>62°N) significantly decreases on 25 August. The difference in area-averaged daily precipitation in the upper portion of FS2 on August 25 is -0.03 mm/day. In the lower portion of FS2 (<62°N), we find a dipole feature in the precipitation difference field: the SMOKE case predicts precipitation further downwind compared to the CLEAN case. This pattern is opposite to the one on 24 August, but similar to the pattern of precipitation difference in the upper portion of FS1 on 10 August as shown in Figure 4.10(a). Examining the CDNC and IN fields in lower portion of FS2, we find that they are also

very similar to those in the upper portion of FS1, for example, high CDNC and low IN concentrations.

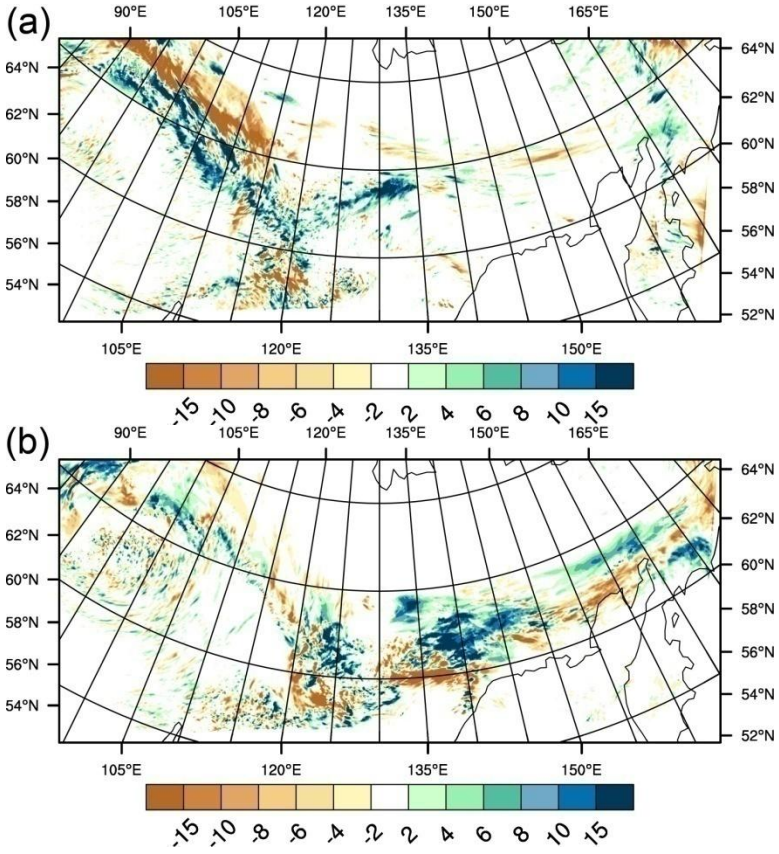

Figure 4.15: Differences in daily precipitation between SMOKE and CLEAN (mm/day): (a) 24 August, and (b) 25August

4.4 Assessment of the Impact of Smoke on Radiation

4.4.1 Comparison of Modeled Radiative Fluxes against SRB

Firstly, in Figure 4.16 we compare the SRB $SW_{TOA}\uparrow$ and $SW_{TOA}\uparrow$ modeled by the SMOKE case for the entire simulation period (30 days). Please note that here we use positive values to represent $SW_{TOA}\uparrow$. Since we output modeled variables every two hours in contrast to the 3-hour temporal resolution of the SRB dataset, for each day, we calculate the daily $SW_{TOA}\uparrow$ by averaging the $SW_{TOA}\uparrow$ at 0000, 0600, 1200, and

1800UTC. In addition, to accommodate the spatial resolutions of the model grid and SRB dataset, we average all the model grids within each 1° × 1° grid. In total, 44370 pairs of modeled daily $SW_{TOA}\uparrow$ and SRB daily $SW_{TOA}\uparrow$ are labeled in the scatter plot as shown in Figure 4.16. The black solid line shows the regression slope passing through (0,0) point. The regression between modeled the daily $SW_{TOA}\uparrow$ and SRB daily $SW_{TOA}\uparrow$ equals 0.76, which indicates that the model tends to underestimate $SW_{TOA}\uparrow$. The underestimation in $SW_{TOA}\uparrow$ is very likely due to "too few, too bright" clouds modeled by numerical models [*Nam et al*., 2012], as in WRF-Chem-SMOKE. For example, our result is very similar to the study conducted by *Wu et al*. [2011], which examines the radiative forcing of smoke in the Amazonia region using the WRF-Chem model. They find that modeled daily $SW_{SFC}\downarrow$ is 10% larger than SRB $SW_{SFC}\downarrow$, mainly due to optical thin clouds produced by the model. The underestimated daily $SW_{TOA}\uparrow$ (e.g. the points in the lower right portion of the scatter plot) in our study can be explained by the same reason.

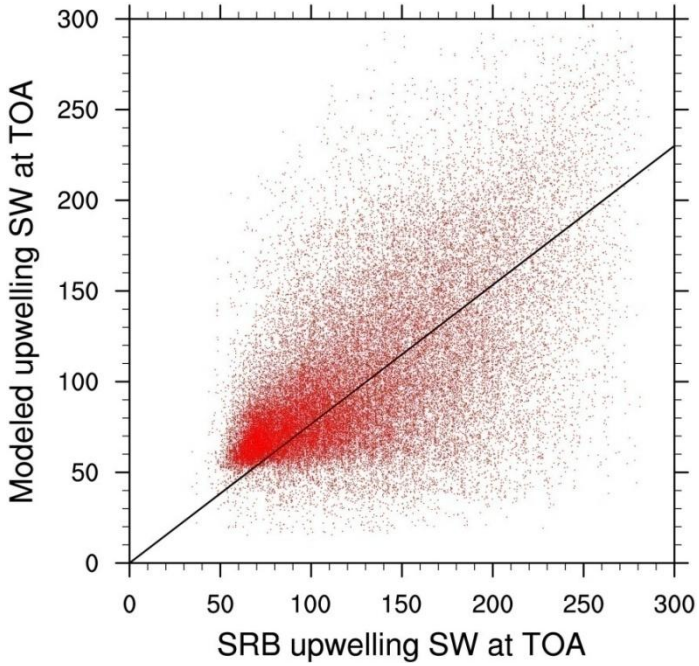

Figure 4.16: Scatter plot of modeled daily $SW_{TOA}\uparrow$ versus SRB daily $SW_{TOA}\uparrow$(unit: W/m^2).

Another possible explanation for the smaller magnitude of modeled daily $SW_{TOA}\uparrow$ compared to the SRB daily $SW_{TOA}\uparrow$ is due to the fact that SRB misclassifies the strong smoke plumes as cloud layers. Strictly speaking, the SRB dataset (v3.0) does not account for the real-time aerosol/smoke field, but only considers the standard aerosol profiles. Figure 4.17 shows the SRB cloud fraction field at 0600UTC on 19 August, 2002. The SRB cloud fractions are retrieved from ISCCP and used as inputs in the SRB dataset. Compared to the true color image shown in Figure 4.3(b), we find that the SRB dataset classifies many 1° × 1° grids as having cloud fraction higher than 0.95. However, the 1° × 1° grids in two regions (62°N~66°N,115°E~125°E and 67°N~73°N, 110°E~150°E) are actually covered by strong smoke plumes. Because of the higher reflectivity associated with cloud pixels as compared to smoke pixels, the SRB dataset tends to overestimate $SW_{TOA}\uparrow$.

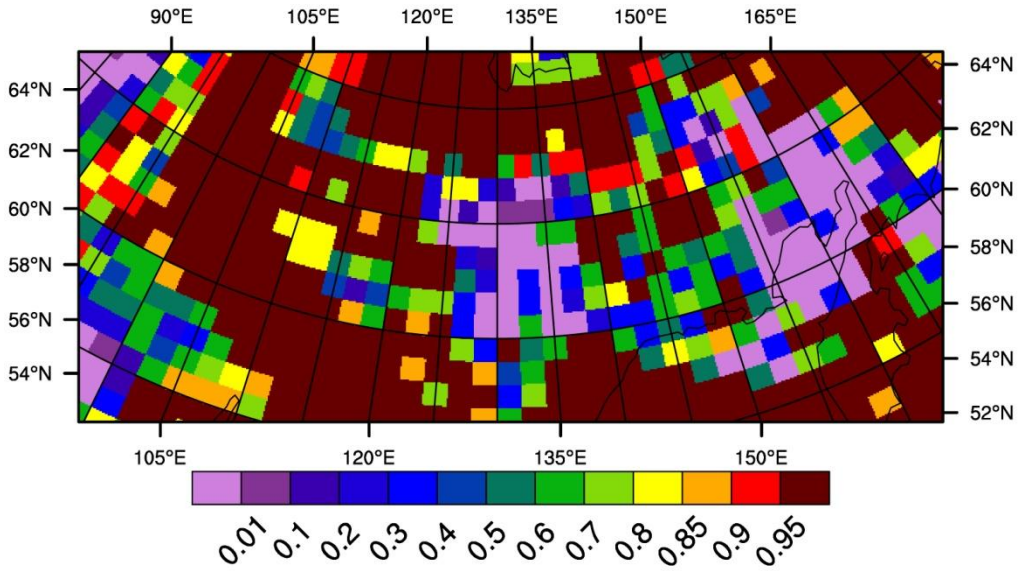

Figure 4.17: SRB cloud fraction used in the SRB dataset at 0600UTC on 19 August 2002.

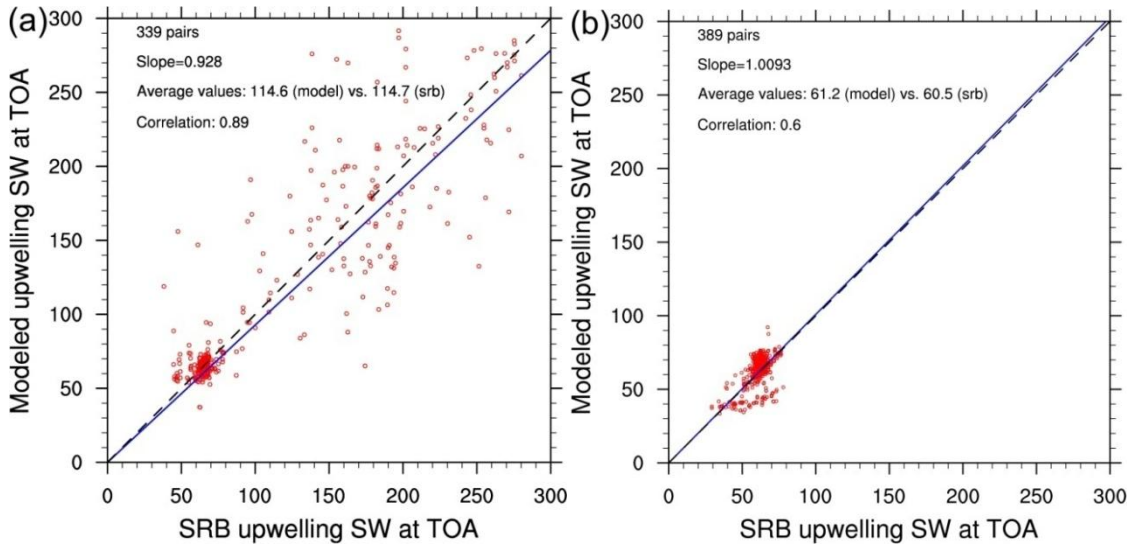

Figure 4.18: (a) scatter plot of modeled daily $SW_{TOA}\uparrow$ versus SRB daily $SW_{TOA}\uparrow$(unit: W/m^2) for the model grids with cloud fraction close to SRB cloud fraction (~±0.05); (b) scatter plot of modeled daily $SW_{TOA}\uparrow$ versus SRB daily clear-sky $SW_{TOA}\uparrow$(unit: W/m^2)

In order to prove our reasoning above, we further generate two more scatter plots, in which the SRB and modeled daily $SW_{TOA}\uparrow$ pairs are screened by different criteria. Firstly, we calculate the modeled cloud fractions, which are assumed as the ratios of the number of model grids with daily averaged TWP (only 0000, 0600,1200, and 1800UTC; four time steps) larger than 0.1 kg/m^2 to the total number of model grids in each 1° × 1° grid. In Figure 4.18(a), we label the SRB and modeled daily $SW_{TOA}\uparrow$ pairs if the absolute differences between SRB and modeled cloud fractions are smaller than 0.05. The regression and correlation analyses, as well as average values show that the modeled daily $SW_{TOA}\uparrow$ are reasonably modeled compared to SRB. In addition to all-sky radiative fluxes discussed above, the SRB dataset also provides clear-sky radiative fluxes, which are calculated by assuming the absence of cloud. Therefore, we select the modeled daily $SW_{TOA}\uparrow$ with daily averaged TWP and AOD in the 1° × 1° grid (only 0000, 0600,1200, and 1800UTC; four time steps) which are below 0.1 kg/m^2 and 0.01, respectively, and

compare the values against the clear-sky SRB daily $SW_{TOA}\uparrow$ in Figure 4.18(b). Again, the statistical analyses show a good agreement between model simulation and the SRB dataset. These results highlight the importance of reasonable representation of modeled cloud properties.

4.4.2 The Impact of Smoke on Radiative Fluxes during Fire Regime 1

Figure 4.19 shows SRB radiative fluxes in the first column and radiative fluxes modeled by SMOKE and CLEAN in the second and third columns at 0600UTC on 9, 10 and 12 August. On 9 August, smoke plumes are located around 60°N~65°N, 125°E~135°E. In this region, the values of $SW_{TOA}\uparrow$ in the SRB dataset are around 150~200 W/m^2 as shown in Figure 4.19(a), while $SW_{TOA}\uparrow$ produced by the SMOKE and CLEAN cases, as shown in Figures 4.19(b) and (c), are 175~250 W/m^2 and 50~100 W/m^2, the difference between which can be interpreted as due to smoke direct radiative forcing in this region. When examining the $SW_{TOA}\uparrow$ associated with the frontal system (FS1), we find that no significant difference exists between SMOKE and CLEAN, and both cases underestimate the magnitudes and the horizontal extents of $SW_{TOA}\uparrow$ compared to the SRB dataset.

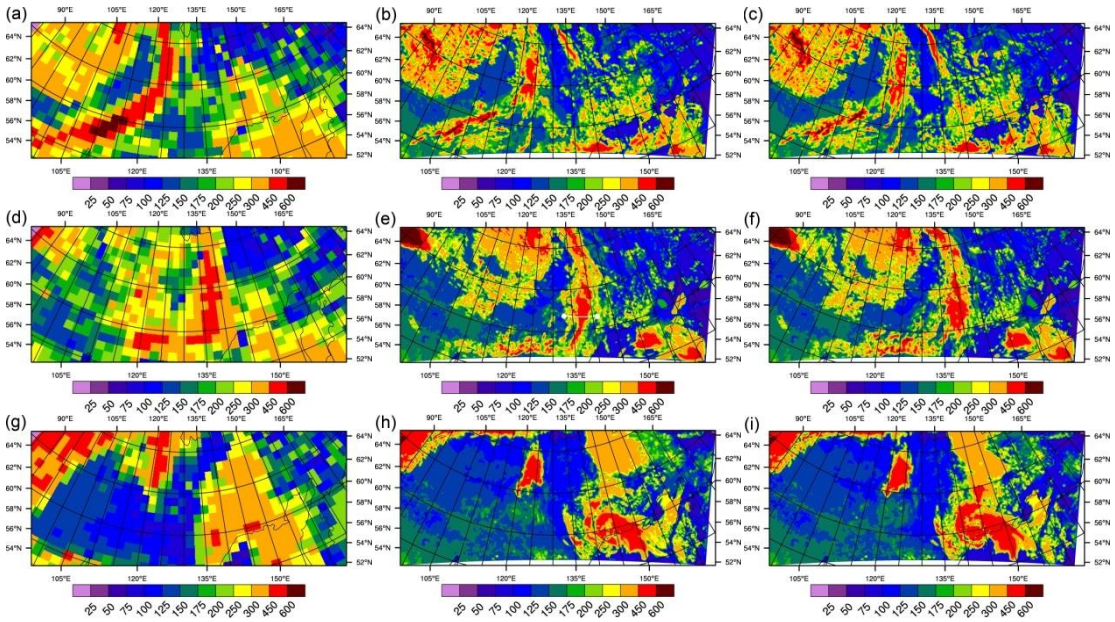

Figure 4.19: SRB $SW_{TOA}\uparrow$ (first column) and $SW_{TOA}\uparrow$ modeled by SMOKE (second column) and CLEAN (third column) during FR1 at 0600UTC on 9, 10, and 12 August 2002 (from top to bottom).

By 0600UTC 10 August, the smoke particles have almost been swirled in FS1. As the smoke particles being activated as CDNC and IN (shown in Figure 4.5), they strongly affect radiation fields via the indirect aerosol effect. The spatial distributions of $SW_{TOA}\uparrow$ modeled by SMOKE and CLEAN (shown in Figures 4.19(e) and (f), respectively) significantly differ from each other in the lower portion of FS1. In particular, the lower portion of FS1 in CLEAN has cloud coverage with larger horizontal extent and appears further downwind. Comparing against the SRB dataset, we find that the SMOKE case performs much better in terms of simulating the spatial distributions of $SW_{TOA}\uparrow$. In order to explain how smoke, via functioning as CCN and IN, induces such differences in cloud properties and resulting $SW_{TOA}\uparrow$, we examine the smoke-induced changes in cloud properties along the cross-section labeled in Figure 4.19(e).

Similar to Figures 4.8 and 4.14, Figure 4.20 shows smoke-induced changes in CWC, RWC, IWC, and SWC in color contours as well as column-integrated CDNC and IN in curve lines at 0600UTC on 10 August 2002. As shown in Figures 4.20(a) and (b), the CLEAN case produces a cloud cell with a large amount of RWC and SWC at 135 km along the X-axis, while the corresponding cloud cell in SMOKE, located around 145 km along the X-axis, contains a moderate amount of RWC but lacks strong vertical development and SWC. This is probably due to the high CDNC, which suppress the collision-coalescence and riming processes in this region. As shown in Figure 4.20(b), we find that relatively high IN number concentrations are activated at the forward edge of the lower portion of FS1. As a result, higher IN concentration promotes the formation of SWC and quickly depletes the water content in this region. In contrast, CLEAN produces a layer with a moderate amount of CWC. Therefore, the combined effects of CDNC and IN lead to the smoke-induced changes in cloud properties, which further cause differences in $SW_{TOA}\uparrow$ as shown in Figures 4.19(e) and (f).

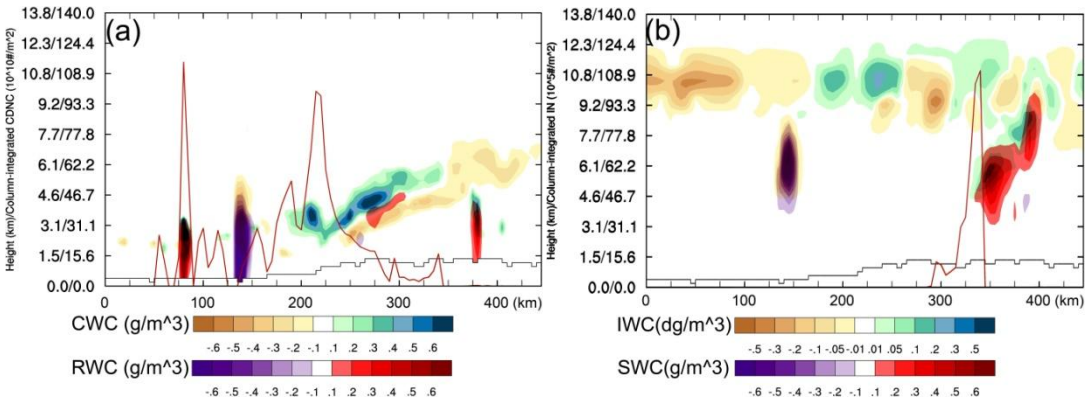

Figure 4.20: Similar to Figure 4.8, but for 0600UTC 10 August 2002.

On 10 August 2002, according to the SRB dataset, the values of $SW_{TOA}\uparrow$ behind (to the west of) FS1 are around 250~450 W/m^2. These fairly high values are due to the

presence of stratocumulus clouds behind the frontal system as shown in the MODIS true color image in Figure 4.21. However, both SMOKE and CLEAN fail to produce a considerable quantity of cloud coverage, which eventually causes underestimated $SW_{TOA}\uparrow$ behind FS1 on 10 August.

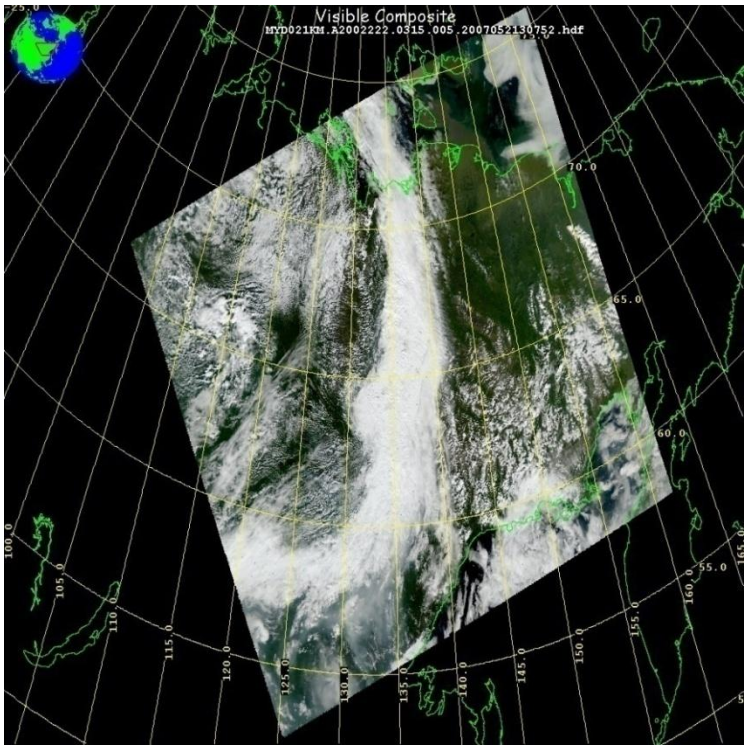

Figure 4.21: MODIS true color image at 0315UTC on 10 August 2002 (from http://ladsweb.nascom.nasa.gov/)

As discussed above, by the time of 0400~0600UTC 12 August 2002, the upper portion of FS1 has developed into a sub-polar vortex, while the lower portion of FS1 has become a mid-latitude cyclone system. As shown in Figure 4.19(g), the magnitudes of $SW_{TOA}\uparrow$ associated with the mid-latitude cyclone are around 300~450 W/m^2. (The values of $SW_{TOA}\uparrow$ in only a few 1° × 1° grids are higher than 450 W/m^2.) When examining the $SW_{TOA}\uparrow$ modeled by SMOKE and CLEAN in the same region, we find that the

magnitudes in both cases are higher than 450 W/m^2 but lower than 600 W/m^2 as shown in Figures 4.19(h) and (i). However, it should be noted that the performance by SMOKE exceeds that by CLEAN on 12 August, since SMOKE produces fewer model grids with $SW_{TOA}\uparrow$ higher than 450 W/m^2. This is probably due to the fact that IN activated from smoke particles keep depleting the cloud water within the cyclone.

4.4.3 The impact of smoke on radiative fluxes during fire regime 2

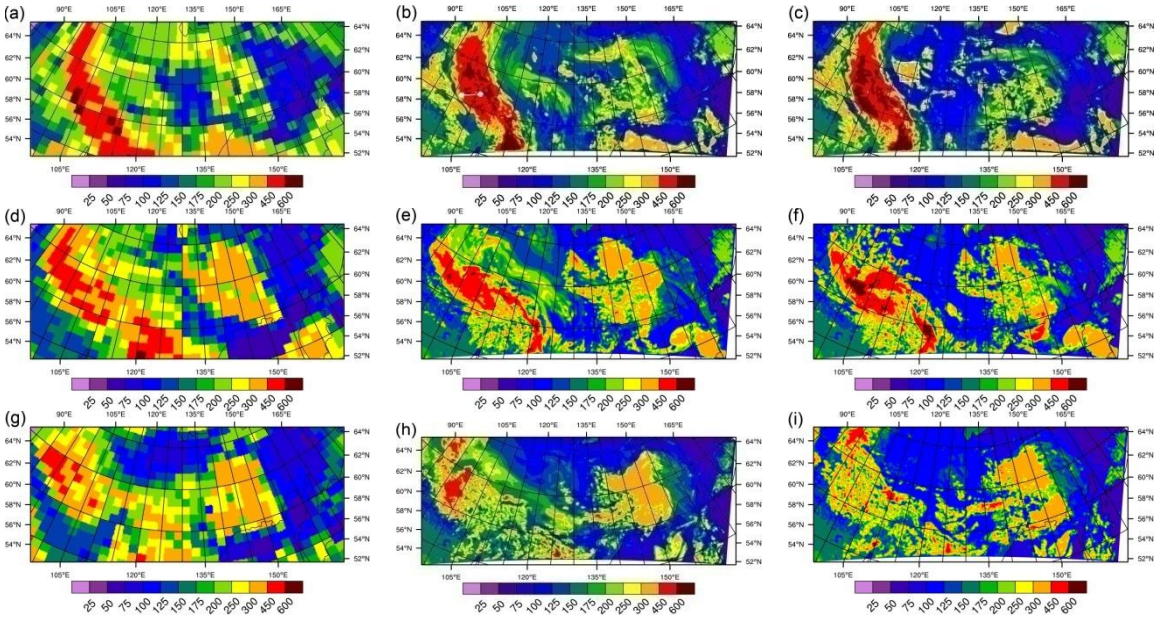

Figure 4.22: Similar to Figure 4.19, but for FR2 at 0600UTC on 19 , 20, and 21 August 2002 (from top to bottom)

During fire regime 2 (FR2), a large amount of smoke is emitted because of the presence of a persistent blocking high-pressure system as discussed in Section 4.3.1. On 19 August, dense smoke plumes cover a vast region and exert significant radiative forcing at TOA and the surface. Meanwhile, around the western and eastern edges of the blocking high-pressure system, where the pressure cap is relatively weak, two cloud decks (shallow convections) are located, which are contaminated by smoke particles. The

smoke-induced changes in radiative fluxes via the direct and indirect aerosol effects on 19 August and the following two days will be the focus of this section.

At 0600UTC on 19 August, the SRB $SW_{TOA}\uparrow$ associated with the smoke plumes are around 175~250 W/m^2, as shown in Figure 4.22(a). It should be noted that the SRB $SW_{TOA}\uparrow$ are calculated by assuming the smoke plumes as clouds. Comparing against the SRB dataset, we find that the SMOKE case successfully reproduces the magnitudes and the spatial distribution of the $SW_{TOA}\uparrow$ field below 67°N, between 110°E~130°E as shown in Figure 4.22(b); however, SMOKE significantly underestimates the magnitudes of $SW_{TOA}\uparrow$ above 67°N, between 110°E~125°E by about 100 W/m^2. The difference between SRB and modeled $SW_{TOA}\uparrow$ is probably due to the false assumption of cloud layers in the SRB dataset or underestimation in modeled smoke AODs in this region. Apparently, the CLEAN case does not reproduce the $SW_{TOA}\uparrow$ associated with the smoke plume.

As shown in Figure 4.22(b), around the eastern edge of the blocking high-pressure system, the liquid-phase cloud deck, which stretches from west (130°E) to east (150°E) along 68°N, is greatly affected by the smoke particles. As shown in Figure 4.23(a), high CDNC are activated from smoke particles within this cloud deck at 0600UTC on 19 August. Due to the first indirect aerosol effect, the cloud deck in the SMOKE case becomes more reflective than the one in the CLEAN case. As a result, the values of $SW_{TOA}\uparrow$ produced by SMOKE are around 250 W/m^2, which are much closer to the SRB $SW_{TOA}\uparrow$ as compared to CLEAN in this region.

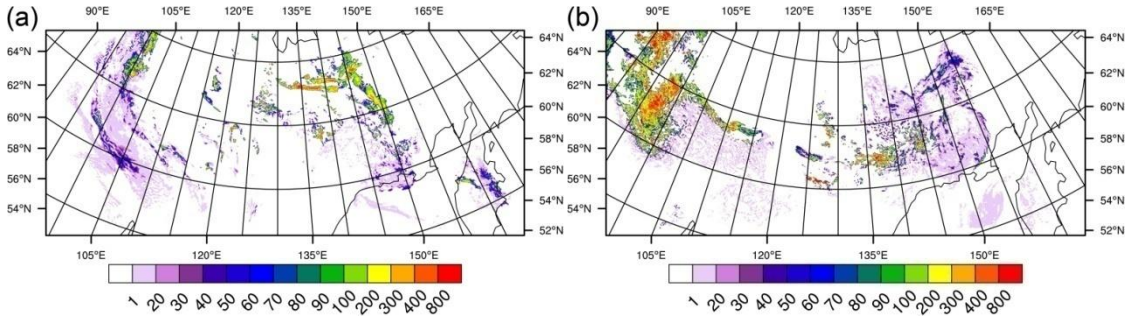

Figure 4.23: Column-integrated activated CDNC (unit: 10^9 no./m2) for (a) 0600UTC 19 August 2007 and (b) 0600UTC 21 August 2007

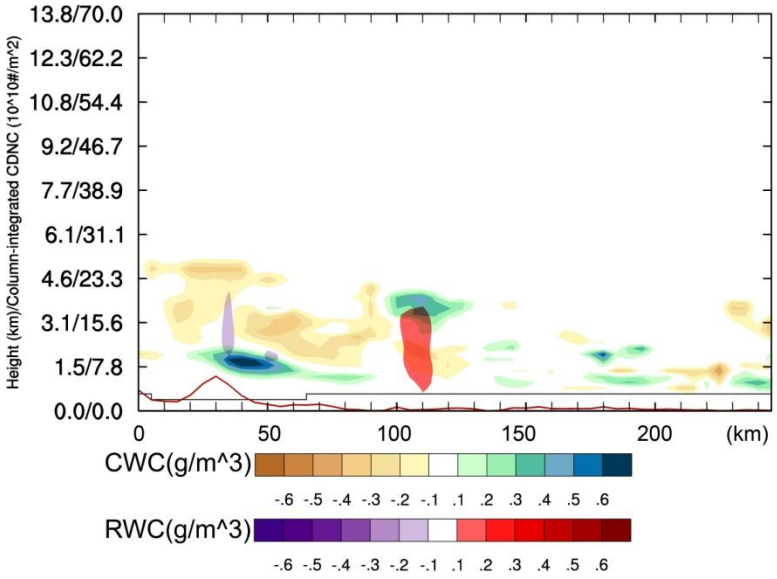

Figure 4.24: Column-integrated activated CDNC (unit: 10^9 no./m2) for (a) 0600UTC 19 August 2007 and (b) 0600UTC 21 August 2007

When examining the cloud deck around the western edge of the blocking high-pressure system (from 67°N, 100°E to 56°N 115°E), we find that this cloud deck, which is also in liquid phase, is contaminated by a relatively small amount of smoke. Consequently, column-integrated CDNC activated from smoke particles are relatively low in this area (~4×10^{10} no./m^2). The values of SRB $SW_{TOA}\uparrow$ associated with this cloud deck are generally within 450~600 W/m^2 as shown in Figure 4.22(a). Therefore, we find that the SMOKE case performs better than the CLEAN case in simulating $SW_{TOA}\uparrow$, since

the latter predicts too many model grids with $SW_{TOA}\uparrow$ higher than 600 W/m^2 as shown in Figure 4.22(c). In order to interpret smoke-induced changes in $SW_{TOA}\uparrow$, we examine smoke-induced changes in cloud properties (CWC, RWC, and column-integrated CDNC) along the cross-sections labeled in Figure 4.22(b) at 0600UTC on 19 August. As shown in Figure 4.24, relatively low CDNC in the SMOKE case actually promote rain formation, while more CWC is predicted by the CLEAN case in the cloud deck. Therefore, the cloud deck in the SMOKE case is optically thinner and less reflective than the one in CLEAN.

During the following two days (20 and 21 August), the direct aerosol effect of smoke remains significant. For example, the magnitudes of SRB $SW_{TOA}\uparrow$ associated with the smoke plumes are still around 175~250 W/m^2. The SMOKE case performs reasonably in predicting the magnitudes and the spatial distributions of radiative fluxes associated with the smoke plumes. The intensity of the cloud deck around the western edge of the blocking high-pressure system weakens on 20 and 21 August. For example, we find that the number of 1° × 1° grids with SRB $SW_{TOA}\uparrow$ higher than 450W/m^2 declines on 20 August compared to the previous day, and the shallow convective clouds degrade to stratocumulus clouds on 21 August. Comparing the $SW_{TOA}\uparrow$ modeled by SMOKE and CLEAN against the SRB dataset on 20 and 21 August, we find that the SMOKE case performs much better than the CLEAN case in simulating the $SW_{TOA}\uparrow$ associated with the cloud deck around the western edge of the blocking high-pressure system. Specifically, similar to the previous day on 19 August, the CLEAN case overestimates the number of model grids with $SW_{TOA}\uparrow$ higher than 600W/m^2 on 20 August as shown in Figure 4.22(f). On 21 August, however, the CLEAN case

underestimates the magnitudes of $SW_{TOA}\uparrow$ associated with the cloud deck between 90°E~100°E below 65°N by 100~200W/m^2 as shown in Figure 4.22(i). This is due to the fact that the stratocumulus clouds have been well mixed with the smoke plume by 21 August. High CDNC are activated from the smoke particles as shown in Figure 4.23(b). Due to the first indirect aerosol effect, the albedo of the cloud deck in the SMOKE is higher.

Although the microphysical effect of smoke is the focus of our study, we cannot rule out the importance of the semi-direct or radiative effect of smoke. Here we show one example of how the semi-direct effect of smoke completely suppresses the development of one short-lived shallow cloud deck. As shown in Figure 4.22(c), the white square highlights one liquid-phase shallow cloud deck, which is only predicted by the CLEAN case at 0600UTC on 19 August. The cloud deck has a cloud lifetime of less than 2 hours, since it does not appear in the CLEAN case at 0400UTC. In the same area, the SMOKE case predicts heavy smoke plumes for a few days already. Therefore, in order to interpret the semi-direct effect of smoke on this cloud deck, we examine the difference in area-averaged heating profiles at 0400UTC between SMOKE and CLEAN in Figure 4.25. Apparently, the strong smoke plumes in this area significantly heat the atmosphere. The difference in area-averaged heating profiles between the two cases peaks around 2 km above the terrain. As a result, very likely due to the stability of atmosphere being increased by the presence of smoke, the development of the cloud deck is completely suppressed in the SMOKE case.

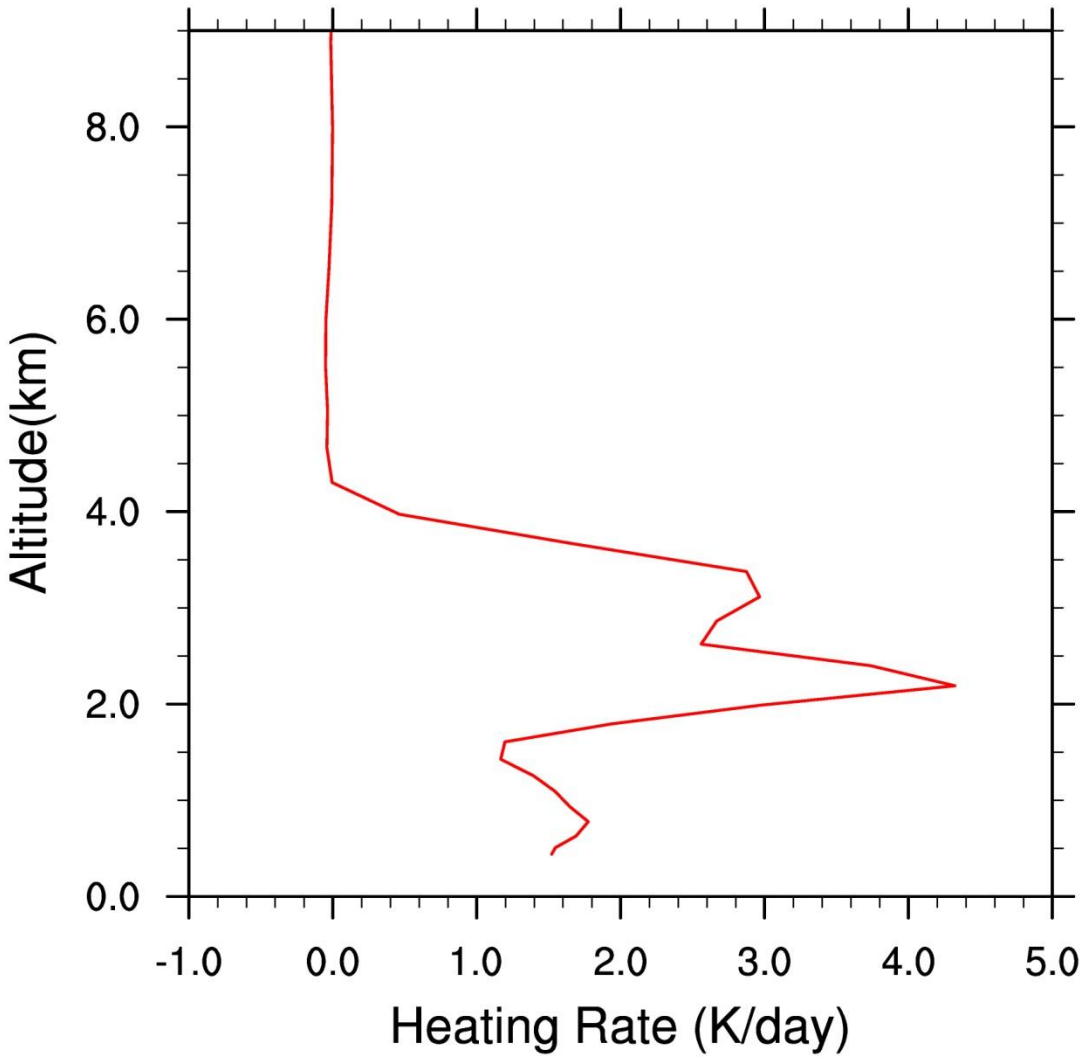

Figure 4.25: The difference in heating profiles between the SMOKE and CLEAN cases for 0400UTC 19 August. The heating profiles are averaged over a square area as shown in Figure 4.22(c)

4.5 Conclusions

In this study, we use the WRF-Chem-SMOKE model to simulate the 2002 Yakutsk fire season to investigate the extent to which smoke can alter the cloud microphysical properties, precipitation, and radiative fluxes under different fire regimes and meteorological conditions. The model treats size- and composition-resolved smoke

emission fluxes, which are computed using the MODIS fire radiative power product. Modeled 3D smoke fields are compared against the composite MODIS AOD and cloud top temperature fields. 3D fields of CDNC (prognostic) and IN (diagnostic) are explicitly derived from the 3D smoke fields, and coupled with the Morrison two-moment microphysics scheme. The fully coupling of 3D smoke-cloud-precipitation and smoke-radiation interactions in WRF-Chem-SMOKE enable us to examine the impact of smoke on cloud microphysical properties, precipitation and radiative fluxes.

By synergizing the model outputs and the MODIS observations, we are able to analyze some major features of smoke plume during FR1 (August 1-10) and FR2 (August 11-31). During FR1, a relatively small amount of smoke is emitted, and is transported northward to the upper portion of FS1 (>60°N). A large amount of smoke is emitted during the FR2 due to the presence of a blocking high-pressure system. After August 22, FS2 begins to interact and deplete a large amount of smoke emitted during FR2. Compared to the MODIS observations, both the AOD values and the spatial distributions of smoke plumes during FR1 and FR2 are reasonably reproduced by the model. However, the model does not capture the smoke plume originating from several small fires, most likely due to the low temporal resolution of MODIS coverage.

Our major findings are summarized below.

a). Smoke-induced changes in cloud microphysical properties under different meteorological conditions

Our modeling results demonstrate that the CDNC and the number concentration of IN activated from smoke particles vary significantly under different fire regimes and

meteorological conditions. A large amount of CDNC and a very small amount of IN are activated in the upper portion of FS1 (>65°N) as shown in Figure 4.5. After the smoke particles are depleted or consumed, activated CDNC become low. In contrast, both CDNC and IN concentrations are very high in FS2.

We examine the CDNC/IN concentrations and the corresponding smoke-induced changes in all hydrometeors along the cross-sections of the frontal systems. By comparing the SMOKE case to the CLEAN case, we find that under high CDNC/low IN condition:

– RWC is significantly reduced (e.g. the total amount is 47% less along the cross-section, 50-150 km as shown in Figure 4.8(a)), most likely due to the suppression in collision-coalescence process;

– SWC is also significantly reduced (e.g. the total amount is 29% less along the cross-section, 50-150 km as shown in Figure 4.8(b)), or its formation is almost shut down in the region with high CDNC concentrations (0-100 km as shown in Figure 4.8(d)), most likely due to the suppression in riming process. However, more SWC appears near the forward edge of FS1 (e.g. the total amount is 28.6% more along the cross-section, 150-225 km in Figure 4.8(b)), very likely due to relatively more heterogeneous ice nucleation and the longer lifetimes of cloud cells;

– CWC can be either increased or decreased, depending on the phase of cloud lifetime cycle. A dense layer of CWC can be formed if collision-

coalescence and riming processes are suppressed simultaneously (e.g. a layer of CWC has maximum value of 0.84 g/m^3 as shown in Figure 4.8(c));

– IWC originating from the heterogeneous ice nucleation slightly increases.

Under low CDNC/low IN conditions:

– Much more RWC is produced in the SMOKE case under low CDNC condition, probably because of invigorated collision-coalescence process (e.g. as shown in Figure 4.8(g)).

Under high CDNC/high IN conditions:

– Less RWC is produced in the SMOKE case (e.g. the total amount is 4.3% less in Figure 4.14(a) and 48.4% less in Figure 4.14(c)) due to suppressed collision-coalescence process. However, less RWC is distributed in more cloud cells (e.g. as shown in Figure 4.14(a));

– More IWC is produced along the forward edge of FS2 in the SMOKE case due to heterogeneous ice nucleation (e.g. as shown in Figures 4.14(d) and (f));

– More SWC is produced in the SMOKE case because of a significant glaciation effect (e.g. the total amount of SWC is 4% more even in the region with high CDNC, as shown in Figure 4.14(d)). In addition, a shallower mixed-phase region is produced in the SMOKE case.

Therefore, smoke can either suppress or invigorate the formation of RWC and SWC depending on the competing effects of CDNC(CCN) and IN.

b). Smoke-induced changes in spatial distribution of cloudiness under different meteorological conditions

We analyze the changes in both individual cloud cells along the cross-sections and total cloudiness (differences in TWP between the SMOKE and CLEAN cases). Under the high CDNC/low IN condition, cloud cells in the SMOKE case have a longer lifetime, and travel further downwind (similar to the mechanism proposed by *Andreae et al*. [2004] and *Rosenfeld et al*. [2008]). This leads to positive changes in TWP along the forward edge of the upper portion of FS1. Therefore, the cloudiness in the SMOKE case appears further downwind (e.g. Figure 4.7).

After CDNC are consumed, the large-scale atmospheric dynamics have been significantly modified (e.g. earlier release of convective energy in the SMOKE case as shown in Figure 4.9). As a result, the presence of cloudiness/large TWP and the onset of convective energy in the SMOKE case lag behind the CLEAN case. The differences in TWP between the SMOKE and CLEAN cases transform from a noisy pattern (Figure 4.6(b)) to organized patterns (Figures 4.6(c) and (d)).

In FS2, the high CDNC cause cloud cells to move slightly slower (e.g. Figure 4.14(a)). Finally, the SMOKE and CLEAN cases predict FS2 in two completely different regions (the forward edge of FS2 in SMOKE locates near the rear edge of FS2 in CLEAN). More IN activated from smoke cause a significant glaciation effect, which counteracts the effect of CDNC on cloud lifetime. As a result, the smoke-induced

changes in cloud lifetime between two cases are likely small. The TWP difference field develops from a noisy pattern (Figure 4.13(a)) to a parallel dipole pattern (Figures 4.13(b) and (c)). In contrast to the smoke-induced changes in TWP in the upper portion of FS1, the cloudiness of FS2 produced by the CLEAN case appears further downwind.

c). Smoke-induced changes in precipitation under different meteorological conditions

Daily precipitation difference fields are directly related to the TWP difference fields. Therefore, precipitation difference fields also evolve from a noisy pattern (Figure 4.10(a)) to organized patterns (Figures 4.10(b) and 4.15(a)). Under the high CDNC/low IN condition (the upper portion of FS1), the SMOKE case produces less precipitation upstream and more precipitation downstream because of longer cloud lifetime. This caused a slight decrease in the area-averaged daily precipitation difference (-0.47 mm/day for the upper portion of FS1). Under the high CDNC/high IN condition (FS2 and the lower portion of FS1), daily precipitation difference fields exhibited a symmetrical, parallel dipole feature (the precipitation band predicted in CLEAN appears further downwind than that in SMOKE). We find a slight decrease in the area-averaged daily precipitation difference in the SMOKE case (-0.42 mm/day). Smoke has a small, negative net effect on area-averaged daily precipitation probably because of high CDNC; however, the redistribution of precipitation is significant and sensitive to heterogeneous IN activation from smoke particles. This result is in agreement with *Seifert et al.* [2012] that aerosol has a small effect on precipitation when averaged over space and time.

The smoke-induced changes in the daily precipitation associated with the final stages of FS1 and FS2 are also quite different. The changes in large-scale atmospheric dynamics cause large negative changes in area-averaged daily precipitation on August 11

(-2.04 mm/day) and large positive changes on the following day (1.32 mm/day) as the upper portion of FS1 develops into a sub-polar vortex. The changes in area-averaged daily precipitation become very small (-0.03 mm/day) as FS2 begins to dissipate.

In summary, the microphysical effect of smoke can lead to the changes in large-scale dynamics. In this case, the precipitation can be significantly suppressed at first, and be invigorated during the next day in different locations (downwind direction). Otherwise, compared to CLEAN, precipitation in SMOKE occurs almost on the same day but different locations, and had relatively small decreases in area-averaged daily precipitation.

d). Smoke-induced changes in radiative fluxes under different meteorological conditions

We find that the relative importance of the direct and indirect aerosol effects of smoke varies under different fire regimes and meterological conditions. Moreover, the indirect aerosol effect can either offset or add to the direct aerosol effect, depending on the CDNC/IN regimes. Therefore, it is critical to determine the total effect of smoke on the radiation fields. In order to sum up our findings, we calculate the smoke-induced changes in domain-averaged $SW_{TOA}\uparrow$ at 0600UTC for four consecutive days for both FR1 and FR2 and define the values as total aerosol radiative effect (TARE). (It should be noted that we add a minus sign to the values so that the negative values correspond to the cooling effect.) In addition, we calculate the smoke-induced changes in domain-averaged $SW_{TOA}\uparrow$, but only for the model grids with a very small amount of cloudiness (TWP<0.01kg/m^2, in both CLEAN and SMOKE), and define the value as direct aerosol radiative effect (DARE). The time series of TARE (red lines) and DARE (blue lines) for

FR1 and FR2 are shown in Figures 4.26(a) and (b), respectively. During FR1 (from 9 to 12 August), the direct effect of smoke causes a slight cooling effect at TOA. By 11 August, nearly all smoke particles emitted during FR1 have been swirled into the frontal system completely; therefore, the DARE value is close to zero on this day. When examining TARE, we find that the value remains positive. This indicates that the indirect aerosol effect competes with and exceeds the direct aerosol effect of smoke. This is mainly due to the fact that the smoke as IN keeps depleting the cloud water at the forward edge of the lower portion of the frontal system (FS1). For FR2, we only consider the western portion of the domain (<130°E), since it is affected by the smoke for a shorter period than the eastern portion of the domain. DARE from 19 to 22 August causes a significant cooling effect at TOA, apparently due to the long-lasting smoke plumes in the domain. During 19~20 August, the values of TARE are close to zero, indicating that the indirect aerosol effect compensates for the direct aerosol effect of smoke. This is actually due to low CDNC, which promote rain formation in shallow convections and cause the cloud layers to be optically thinner. During 21~22 August, the values of TARE becomes negative. This is due to the fact that high CDNC decrease the size of cloud droplets and increase the albedo of the cloud layers of stratocumulus, which are well mixed with the smoke particles.

By comparing the model simulations against the SRB dataset, our study also demonstrates that the inclusion of the radiative and microphysical properties of smoke in meso-scale modeling can improve the simulation of radiation fields. More specifically, realistically modeled radiation fields require accurate predictions of the amount of smoke in terrestrial state, the amount of smoke swirled in cloud layers, and the CCN/IN

activations of smoke. Apparently, only a meso-scale model such as WRF-Chem-SMOKE is able to achieve this goal.

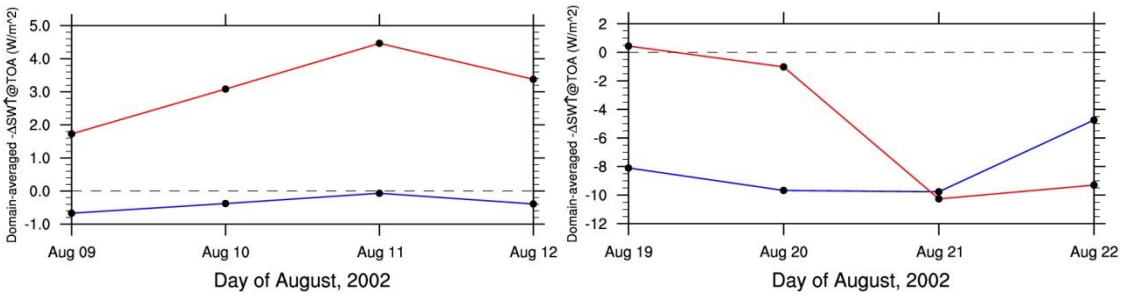

Figure 4.26: The time series of the total aerosol radiative effect (TARE, red lines) and the direct aerosol radiative effect (DARE, blue lines) for FR1 and FR2.

e). Concluding comments

The impact of smoke on the frontal system clouds is more complex than other cloud types (like cumulus in Amazon, *Wu et al*. [2011], or a cluster of cloud cells, *Grell et* al. [2011]). This is because the dynamics of frontal systems keeps evolving, and the multiple convective cloud cells within the frontal system originate, grow, and decay under different CDNC/IN conditions. As discussed above, the impacts of smoke on cloud, precipitation and radiative fluxes can be different or even opposite under different fire regimes and meteorological conditions. These opposite effects can only be unraveled by tracking the development of frontal systems, and examining smoke-induced changes in the microphysical properties of individual cloud cells.

The realistic representations of meteorology fields and smoke emissions are critical for our study. The fact that meso-scale modeling with different re-analysis data can produce quite different meteorological conditions is well known (*Bromwich et al*. submitted to JGR). Although a perfect reproduction of meteorology is not realistic, the goal of diminishing the uncertainties will require further studies involving ensemble

simulations with different re-analysis data. The central challenge is determining how to account for the effects of aerosols in an ensemble study, since these factors can in turn affect the meteorology.

Great uncertainty exists in the estimate of smoke emissions. Usually, a multiplying factor is required for the models to match the observations (O'Neil et al., [2006], *Wu et al*., [2011], *Lu and Sokolik*, [2013b]). However, in our study smoke emissions based on the FRP technique performs very reasonably, which may not be surprising since the FRP technique is tuned to MODIS AOD. More important to the study of smoke-cloud interaction is the actual amount of smoke particles, not AOD values, which greatly depend on the assumptions employed regarding smoke optical properties. In the future, we plan to improve the FRP technique in our study (e.g. including vegetation dependent particulate matter emission coefficient [*Kaiser et al*., 2012]), and systematically validate the modeled smoke plume by comparing against different sources of observations.

CHAPTER 5

CONCLUSIONS

5.1 Dissertation Summary

In this thesis, we develop a fully coupled meso-scale WRF-Chem-SMOKE model with a selection of smoke emission models and improved representations of smoke-cloud interactions in the microphysics scheme. Using WRF-Chem-SMOKE in conjunction with remote sensing data, we investigate to what extent and how smoke released from boreal wildfires affects local cloud properties, precipitation, and radiative fluxes. We accomplish this through in-depth case studies of the 2007 central and eastern Canada wildfires and the 2002 central Siberia wildfires.

In Chapter 2, we thoroughly describe the development of a fully coupled meso-scale model WRF-Chem-SMOKE, which is a modified version of the public WRF-Chem model. WRF-Chem-SMOKE is initiated by meteorological fields from reanalysis data and smoke emissions derived from satellite products. In WRF-Chem-SMOKE, smoke is treated as an internal mixture of OM, BC, and residual particulate matter and injected into the atmosphere following a plumerise model. In addition, the smoke particles can function as SW absorbers, CCN, and IN; therefore, the smoke-radiation and smoke-cloud interactions can be explicitly simulated in the model.

Two major new capabilities coupled in WRF-Chem-SMOKE are: 1) a suite of smoke emission datasets derived from different techniques and satellite products and 2) improved representations of aerosol-cloud interactions, especially ice-phase

microphysical processes. In this thesis, we construct three original smoke emission datasets based on the burned area (BA) technique and the WF_ABBA or the MCD45A1 products or the fire radiative power (PRF) technique and the MCD14ML product. In order to maximize the benefits of each product, we also develop an algorithm that integrates the three original smoke emissions together. The chemical composition of smoke emissions depends on the vegetation type of biomass fuel, which is determined by projecting the active fire or burned area to the vegetation maps such as GLCC v2.0 or MODIS IGBP.

In the public version of WRF-Chem (version 3.1.1), the *Abdul-Razzak and Ghan* scheme [2000] is used to calculate the CCN activation, which is further coupled with the Lin one-moment microphysics scheme for calculating the collision-coalescence process. In WRF-Chem-SMOKE version 3.1.1, we couple the *Abdul-Razzak and Ghan* scheme with the Morrison two-moment microphysics scheme, in which the ice nucleation of the contact and immersion modes also implicitly depends on the CCN activation. In WRF-Chem-SMOKE version 3.3.1, we replace the temperature-dependent ice nucleation schemes with the *Phillips* scheme [2008], which explicitly depends on the chemical composition and size of smoke particles. Moreover, in order to better calculate the riming growth of snow, we replace the fixed riming collection efficiency with a hydrometeor size-dependent collection efficiency.

In Chapter 3, we evaluate the realism of different smoke emission datasets and examine the effect of varying amounts of smoke emission on cloud properties and precipitation through an in-depth analysis of the 2007 central and eastern Canada wildfire event. Firstly, we find that the smoke emission dataset based on the WF_ABBA product

significantly underestimates the smoke loading by a factor of 10. Based on our and other past studies, we conclude that the underestimation of smoke emissions is very likely due to the combined effects of the low emission factors used and underestimation of burned areas by the WF_ABBA product for extreme wildfire events over high latitudes. We compare the spatiotemporal distributions of the ABBA dataset (10 times the smoke emissions derived from the WF_ABBA product + the BA technique), the MCD45 dataset (from the MCD45A1 product + the BA technique), and the FRP dataset (from the MCD14ML product + the FRP technique) in several major fire clusters. We find that the manner in which these three smoke emission datasets differ from each other varies from one fire cluster to another, and the manner is directly related to the fire characteristics. For example, fires in the flaming phase (pyro-convections) release dense smoke plumes, which can block active fire detection by the MCD14ML product; however, a burned scar type of product such MCD45A1 is less affected. For predicting the smoke emissions associated with fast-propagating fire fronts, the ABBA dataset performs much better than the FRP dataset, since the former has finer temporal resolution.

We compare the smoke AOD fields simulated by different modeling cases incorporated with different smoke emission datasets against the MODIS AOD observations. The results show that the differences in smoke emission datasets, even in one fire cluster, could lead to significant discrepancies in modeled AODs. The statistical analyses show that no modeling case always yields the best performance, in terms of magnitude and spatial distribution, through the simulation period; however, the modeling case with the integrated smoke emission dataset produces the highest three-day total Taylor skill scores.

We conduct modeling experiments with varying amounts of smoke emissions of one, five, and ten times as high as the original load derived from the WF_ABBA product (SMOKE1, SMOKE5, and SMOKE10 cases, respectively). The results reveal that the SMOKE10 case (the reference case) reasonably reproduces the cloud pattern associated with the frontal systems observed by MODIS; however, the ice-phase water path is over predicted compared to the MODIS water path product. Compared to smoke-free conditions, low smoke load favors the collision-coalescence process at a certain stage, leading to either positive or negative changes in the cloud water path (CWP). High smoke emissions, on the other hand, cause positive changes as large as 0.5 kg/m^2 in CWP. We find that smoke-induced changes in the domain-integrated CWP are proportional to smoke loading. While the smoke-induced changes in the domain-integrated RWP are mainly negative, those in SWP vary from negative to positive under a high smoke load. The domain-integrated precipitation in SMOKE1, SMOKE5, and SMOKE10 is delayed by ~6, 12~18, and 18~24 hours, respectively. The precipitation in SMOKE10 is firstly significantly delayed due to smoke-induced reduction of the collision-coalescence and riming processes, but ultimately the precipitation is invigorated.

In Chapter 4, we examine the extent to which smoke can alter cloud properties, precipitation, and radiative fluxes under varying fire regimes and meteorological conditions through an in-depth analysis of the 2002 central Siberia (Yakutsk) wildfire season. The fire season lasted for the entirety of August of 2002, which can be further characterized by two fire regimes. During the first fire regime (FR1), a relatively small amount of smoke was emitted and interacted with a relatively strong frontal system (denoted as FS1). During the second fire regime (FR2), the domain was first under the

influence of a blocking high pressure system; therefore, a large amount of smoke was emitted during this period due to dry biomass fuel. By the end of FR2, a relatively weak frontal system (denoted as FS2), coming from the west, began to deplete the smoke particles. In order to simulate the smoke-cloud and smoke-radiation interactions under different meteorological conditions, we adopt the WRF-Chem-SMOKE model version 3.3.1 with the smoke emission dataset derived from the MCD14ML product and the FRP technique. Compared to the MODIS observations, both AOD values and spatial distributions of the smoke plumes during FR1 and FR2 are reasonably reproduced by the model.

During FR1, a relatively small amount of smoke is swirled within FS1 and transported to its upper portion. Consequently, high CDNC and very low IN number concentrations are activated in the upper portion of FS1 (>65°N). Modeled rain water content (RWC) and snow water content (SWC) are strongly reduced by about 25~50% in the region with high CDNC, because collision-coalescence and riming processes are both suppressed by smoke. The cloud cells in the SMOKE case acquire a longer lifetime, travel further downwind, and form more SWC at the forward edge of FS1. As the upper portion of FS1 develops into a polar vortex, the smoke particles substantially alter its total cloudiness and dynamics (e.g. relative humidity and CAPE). As a result, the onset of precipitation is delayed by one day and the area-averaged daily precipitation is significantly affected (-2.04 mm/day on 11 August and 1.32 mm/day on 12 August).

During the final stage of FR2, a large amount of smoke has been well mixed with FS2; therefore, high CDNC and IN number concentration are activated in FS2. Modeled RWC is reduced by smoke due to more CDNC, while modeled SWC is actually increased

by 4% due to the glaciation indirect effect. Because of the competing effects of CDNC and IN, the smoke-induced changes in cloud lifetime are likely very small. However, since the moving speeds of cloud cells are slightly reduced by smoke, the entire FS2 modeled by the smoke-free case appears further downwind compared to the one modeled by the SMOKE case, which leads to a parallel dipole feature in the total cloudiness. The area-averaged daily precipitation associated with FS2 is only slightly reduced by smoke (-0.42 mm/day on 24 August and -0.03 mm/day on 25 August); however, the spatial distribution of precipitation is significantly affected (also a dipole feature).

By comparing $SW_{TOA}\uparrow$ modeled by the SMOKE and smoke-free cases against the NASA SRB dataset, our study demonstrates that the inclusion of the radiative and microphysical properties of smoke in a meso-scale modeling study can improve the simulation of radiation fields, in terms of spatial distribution and magnitude. By examining the smoke-induced changes in $SW_{TOA}\uparrow$, we find that the manner in which smoke affects the radiative fluxes also varies under different meteorological conditions and fire regimes. During FR1, a relatively small amount of smoke is emitted and quickly swirled into the frontal system (FS1); therefore, the direct aerosol effect of smoke causes a slight cooling effect at TOA (~ -1 W/m^2, instantaneous radiative fluxes at 0600UTC). At the forward edge of the lower portion of FS1, high IN number concentrations are activated from smoke and keep depleting the cloud water. As a result, the indirect aerosol effect of smoke reduces the cloud cover and causes a considerable warming effect at TOA. The area-averaged total aerosol radiative effect (TARE, defined in Section 4.5) remains positive (~3 W/m^2) during FR1.

During the early stage of FR2, a large amount of smoke is emitted under the influence of the blocking high pressure system and causes a long-lasting cooling effect at TOA (~ -7 W/m^2). The cloud decks around the edge of the high pressure evolve from shallow convections to stratocumulus clouds. In the shallow convections, relatively low CDNC promote rain formation and cause the cloud layers to become optically thinner. In the stratocumulus clouds, however, higher CDNC are activated since smoke is well mixed with the cloud layers. Consequently, the sizes of cloud droplets are decreased and the cloud albedo is increased. During the early stage of FR2, the indirect aerosol effect of smoke evolves from a warming effect to a cooling effect; therefore, the values of TARE change from near zero to large negative values (~ -10 W/m^2).

5.2 Recommendations for Future Work

In Chapter 3, we identified that the modeled cloud properties and precipitation are very sensitive to the smoke loading. Therefore, in order to delineate the effects of smoke and meteorological factors on cloud properties and precipitation, the representations of 3D smoke fields must be as accurate as possible in the WRF-Chem-SMOKE model. However, the biases in modeled smoke emissions (such as unreasonable fire duration or underestimated fire spreading rate), even in one fire cluster, could lead to significant biases in modeled AODs. Although the algorithm that integrates different smoke emission datasets (Figure 2.1) successfully improves the prediction of smoke AODs, the fact that the fire characteristics vary from one fire cluster to another indicates that one universal algorithm for integrating the smoke emissions may be inadequate. Therefore,

we propose to develop a fire characteristics-orientated integration methodology in the future. For each major fire cluster, we will first evaluate the fire characteristics, such as fire duration, fire burning phases, fire spreading rate, etc. Afterwards, a corresponding algorithm suitable for the fire characteristics in each fire cluster can be automatically selected. For example, in order to determine the smoke emissions associated with fast-propagating fire fronts in the flaming phase, we will primarily rely on a geostationary satellite product such as WF_ABBA and assume a shorter fire duration or faster fire spreading rate.

In Chapter 3, we also thoroughly examined the horizontal distribution of smoke plumes and its impact on cloud properties and precipitation; however, to what extent the vertical distribution of smoke plumes affects the smoke-radiation and smoke-cloud interactions remains quite uncertain. As shown in the study by *Sessions et al*. [2011], modeled vertical distribution of smoke plumes in WRF-Chem strongly depends on the assumptions in the plumerise model. Therefore, in our future study, we propose to improve the plumerise model by adding more options to it. In the current version of the plumerise model in WRF-Chem, the heat flux associated with temperate/boreal forest is actually based on the value for tropical forest due to the lack of data. We will conduct a suite of modeling cases in which we vary the values of heat flux and validate the vertical distribution of smoke plumes against retrievals from CALIPSO and MISR. We also propose to replace vegetation-dependent heat fluxes with more realistic values derived from satellite observations of fire radiative power [*Val Martin et al.,* 2012].

As pointed out in Chapter 4, the impacts of smoke on clouds and precipitation vary under different meteorological conditions and fire regimes. To a large extent, this is

because the micro- and macro-physical properties of clouds are extremely sensitive to varying IN concentrations in different frontal systems with different intensities or even in different portions of one frontal system contaminated by different amounts of smoke. This result highlights the need for accurate prediction of IN; however, our current knowledge of IN activation, especially from smoke particles, remains highly uncertain. Observational/experimental studies have shown different or even contradicting results on the IN behavior of smoke particles [*Hoose and Möhler*, 2012; *Bond et al*., 2013]. The modeling studies have shown a wide spread in the performance of different IN activation parameterizations [*Eidhammer et al*., 2009; *Curry and Khvorostyanov*, 2012]. We are very interested in answering the following question in our future study: What level of accuracy in IN activation is required for meso-scale modeling studies? We propose to run the same case but with a five- or ten-fold increase of IN concentrations as predicted by the Phillips scheme and examine the changes in cloud properties and precipitation fields. We also propose to incorporate other IN activation parameterizations in the WRF-Chem-SMOKE model, such as the D10 scheme [*DeMott et al*., 2010] and the DW04 scheme [*Diehl and Wurzler*, 2004], and compare IN concentrations as well as cloud properties and precipitation modeled by the different cases.

References

Abdul-Razzak, H., and S. J. Ghan (2000), A parameterization of aerosol activation: 2. Multiple aerosol types, *J. Geophys. Res*., *105*(D5), 6837–6844, doi:10.1029/1999JD901161.

Ackerman, A. S., O. B. Toon, D. E. Stevens, A. J. Heymsfield, V. Ramanathan, and E. J. Welton (2000), Reduction of tropical cloudiness by soot, *Science*, 288, 1042–1047.

Akagi, S. K., R. J. Yokelson, C. Wiedinmyer, M. J. Alvarado, J. S. Reid, T. Karl, J. D. Crounse, and P. O. Wennberg (2011), Emission factors for open and domestic biomass burning for use in atmospheric models, *Atmos. Chem. Phys., 11*, 4039–4072, doi:10.5194/acp-11-4039-2011.

Albrecht, B. A. (1989), Aerosols, cloud microphysics, and fractional cloudiness, *Science*, *245*, 1227–1230.

Alexeyev, V. A., and R. A. Birdsey (1998), Carbon storage in forests and peatlands of Russia, *Gen. Tech. Rep. NE 244*, USDA For. Serv. Northeastern Res. Station, Radnor, Pa.

Alvarado, M. J., and R. G. Prinn (2009), Formation of ozone and growth of aerosols in young smoke plumes from biomass burning: 1. Lagrangian parcel studies, *J. Geophys. Res*., *114*, D09306, doi:10.1029/2008JD011144.

Andreae, M. O. and P. Merlet (2001), Emission of trace gases and aerosols from biomass burning, *Glob. Biogeochem. Cycles*, *15*, 955–966.

Andreae, M., D. Rosenfeld, P. Artaxa, A. Costa, G. Frank, K. Longo, and M. Silva Dias (2004), Smoking rain clouds over the Amazon, *Science*, *303*, 1337–1342, doi:10.1126/science.1092779.

Bigg, E. K. (1953), The formation of atmospheric ice crystals by the freezing of droplets, *Q. J. Roy. Meteor. Soc*., *79*, 510–519.

Bond, T. C., et al. (2013), Bounding the role of black carbon in the climate system: A scientific assessment, *J. Geophys. Res. Atmos.*, 118,1–173, doi:10.1002/jgrd.50171.

Borys, R. D., D. H. Lowenthal, S. A. Cohn, and W. O. J. Brown (2003), Mountaintop and radar measurements of anthropogenic aerosol effects on snow growth and snowfall rate, *Geophys. Res. Lett.*, 30(10), 1538, doi:10.1029/2002GL016855.

Bowman, D.M.J.S., *et al.* (2009) Fire in the earth system. *Science*, 324, 481–484.

Carrico, C. M., M. D. Petters, S. M. Kreidenweis, G. R. McMeeking, E. J. T. Levin, W. C. Malm, J. Jeffrey, and L. Collett (2010), Water uptake and chemical composition of fresh aerosols generated in open burning of biomass, *Atmos. Chem. Phys.*, *10*, 5165–5178, doi:10.5194/acp-10-5165-2010.

Chapman, E. G., W. I. Gustafson Jr., R. C. Easter, J. C. Barnard, S. J. Ghan, M. S. Pekour, and J. D. Fast (2009), Coupling aerosol-cloud-radiative processes in the WRF-Chem model: Investigating the radiative impact of elevated point sources, *Atmos. Chem. Phys*., *9*, 945–964, doi:10.5194/acp-9-945-2009.

Chou, M. D., M. J. Suarez, C. H. Ho, M. M. H. Yan, and K. T. Lee (1998), Parameterizations for cloud overlapping and shortwave single-scattering properties for use in general circulation and cloud ensemble models, *J. Clim.*, 11, 202– 214.

Cooper, W. A.(1986), Ice initiation in natural clouds. *Precipitation Enhancement—A Scientific Challenge*, *Meteor. Monogr.*, No.43, *Amer. Meteor. Soc*., 29–32.

Cozic, J., S. Mertes, B. Verheggen, D. J. Cziczo, S. J. Gallavardin, S. Walter, U. Baltensperger, and E. Weingartner (2008), Black carbon enrichment in atmospheric ice particle residuals observed in lower tropospheric mixed phase clouds, *J. Geophys. Res.*,113, D15209, doi:10.1029/2007JD009266.

Curry, J. A., and V. I. Khvorostyanov (2012), Assessment of some parameterizations of heterogeneous ice nucleation in cloud and climate models, *Atmos. Chem. Phys.*, 12(2), 1151–1172, doi:10.5194/acp-12-1151-2012.

DeMott, P. J., A. J. Prenni, X. Liu, S.M.Kreidenweis, M.D. Petters, C.H. Twohy, M. S. Richardson, T. Eidhammer, and D. C. Rogers (2010), Predicting global atmospheric ice nuclei distributions and their impact on climate, *P. Natl. Acad. Sci. USA*, 107, 11217–11222, doi:10.1073/pnas.0910818107.

Diehl, K., M. Simmel, and S. Wurzler (2006), Numerical sensitivity studies on the impact of aerosol properties and drop freezing modes on the glaciation, microphysics, and dynamics of clouds, *J. Geophys. Res.*, 111, D07202, doi:10.1029/2005JD005884.

Dozier, J., (1981), A method for satellite identification of surface temperature fields of subpixel resolution, *Remote Sens. Environ.*, 11,221–229.

Easter, R. C., S. J. Ghan, Y. Zhang, R. D. Saylor, E. G. Chapman, N. S. Laulainen, H. Abdul-Razzak, L. R. Leung, X. Bian, and R. A. Zaveri (2004), MIRAGE: Model description and evaluation of aerosols and trace gases, *J. Geophys. Res.*, *109*, D20210, doi:10.1029/2004JD004571

Eidhammer, T., P. J. DeMott, and S. M. Kreidenweis (2009), A comparison of heterogeneous ice nucleation parameterizations using a parcel model framework, *J. Geophys. Res.*, 114, D06202, doi:10.1029/2008JD011095.

Eidhammer, T., et al. (2010), Ice initiation by aerosol particles: Measured and predicted ice nuclei concentrations versus measured ice crystal concentrations in an orographic wave cloud, *J. Atmos. Sci.*, 67, 2417–2436.

Ellicott, E., E. Vermote, L. Giglio, and G. Roberts (2009), Estimating biomass consumed from fire using MODIS FRE, *Geophys. Res. Lett*., 36, L13401, doi:10.1029/2009GL038581.

Fan, J., et al. (2009), Dominant role by vertical wind shear in regulating aerosol effects on deep convective clouds, *J. Geophys. Res.*, 114, D22206, doi:10.1029/2009JD012352.

Fast, J. D., W. I. Gustafson Jr., R. C. Easter, R. A. Zaveri, J. C. Barnard, E. G. Chapman, G. A. Grell, and S. E. Peckham (2006), Evolution of ozone, particulates, and aerosol direct radiative forcing in the vicinity of Houston using a fully coupled meteorology-chemistry-aerosol model, *J. Geophys. Res.*, 111, D21305, doi:10.1029/2005JD006721.

Feingold, G., H. Jiang, and J. Y. Harrington (2005), On smoke suppression of clouds in Amazonia, *Geophys. Res. Lett*., 32, L02804, doi:10.1029/2004GL021369.

Flannigan, M. D. & J. B. Harrington (1988), A study of the relation of meteorological variables to monthly provincial area burned by wildfire in Canada (1953–1980),

J. Appl. Meteorol. 27, 441–452. (doi:10.1175/1520-0450(1988)027 !0441:ASOTROO2.0.CO;2).

Fountoukis, C., and A. Nenes (2005), Continued development of a cloud droplet formation parameterization for global climate models, *J. Geophys. Res*., 110, D11212, doi: 10.1029/2004JD005591.

Freeborn, P. H., M. J. Wooster, and G. Roberts (2011), Addressing the spatiotemporal sampling design of MODIS to provide estimates of the fire radiative energy emitted from Africa, *Remote Sens. Environ.*, 115, 475–489, doi:10.1016/j.rse.2010.09.017.

Freitas, S. R., K. M. Longo, R. Chatfield, D. Latham, M. A. F. Silva Dias, M. O. Andreae, E. Prins, J. C. Santos, R. Gielow, and J. A. Carvalho Jr. (2007), Including the sub-grid scale plume rise of vegetation fires in low resolution atmospheric transport models, *Atmos. Chem. Phys., 7*, 3385–3398, doi:10.5194/acp-7-3385-2007.

Freitas, S. R., K. M. Longo, M. A. F. Silva Dias, R. Chatfield , P.Silva Dias, P.Artaxo, M. O. Andreae, G. Grell, L. F. Rodrigues, A. Fazenda, and J. Panetta (2009), The Coupled Aerosol and Tracer Transport model to the Brazilian developments on the Regional Atmospheric Modeling System (CATT-BRAMS) – Part 1: Model description and evaluation, *Atmos. Chem. Phys*., 9, 2843-2861, doi:10.5194/acp-9-2843-2009.

Fridlind, A. M., A. S. Ackerman, G. McFarquhar, G. Zhang, M. R. Poellot, P. J. DeMott, A. J. Prenni, and A. J. Heymsfield (2007), Ice properties of single-layer stratocumulus during the Mixed-Phase Arctic Cloud Experiment (M-PACE): 2. Model results, *J. Geophys. Res*., 112, D24202, doi:10.1029/2007JD008646.

Fu, Q., K.-N. Liou, M. C. Cribb, T. P. Charlock, and A. Grossman (1997), Multiple scattering parameterization in thermal infrared radiative transfer, *J. Atmos. Sci.*, 54, 2799–2812.

Ge, C., J. Wang, and J. S. Reid (2014) Mesoscale modeling of smoke transport over the Southeast Asian Maritime Continent: coupling of smoke direct radiative effect below and above the low-level clouds, *Atmos. Chem. Phys*., 14, 159-174, doi:10.5194/acp-14-159-2014.

Ghan, S., N. Laulainen, R. Easter, R. Wagener, S. Nemesure, E. Chapman, Y. Zhang, and R. Leung (2001), Evaluation of aerosol direct radiative forcing in MIRAGE, *J. Geophys. Res.*, 106, 5295– 5316.

Ghan, S. J., H. Abdul-Razzak, A. Nenes, Y. Ming, X. Liu, M. Ovchinnikov, B. Shipway, N. Meskhidze, J. Xu, and X. Shi (2011), Droplet nucleation: Physically based parameterization and comparative evaluation, *J. Adv. Model. Earth Syst., 3*, M10001, doi:10.1029/2011MS000074.

Gibbs, H. K. (2006), Olson's major world ecosystem complexes ranked by carbon in live vegetation: An updated database using the GLC2000 Land Cover Product. NDP-017b. Available at [http://cdiac.ornl.gov/epubs/ndp/ndp017/ndp017b.html] from the Carbon Dioxide Information Center, Oak Ridge National Laboratory, Oak Ridge, Tennessee, USA.

Giglio, L., J. Descloitres, C. O. Justice, and Y. Kaufman (2003), An enhanced contextual fire detection algorithm for MODIS, *Remote Sens. Environ.*, 87, 273– 282.

Giglio, L., T. Loboda, D. P. Roy, B. Quayle, and C. O. Justice (2009), An active-fire based burned area mapping algorithm for the MODIS sensor, *Remote Sens. Environ.*, 113(2), 408–420, doi:10.1016/j.rse.2008.10.006.

Giglio, L., J. T. Randerson, G. R. van der Werf, P. S. Kasibhatla, G. J. Collatz, D. C. Morton, and R. S. DeFries (2010), Assessing variability and long-term trends in burned area by merging multiple satellite fire products, *Biogeosciences*, 7(3), 1171–1186, doi:10.5194/bg-7-1171-2010.

Givati, A., and D. Rosenfeld (2004), Quantifying precipitation suppression due to air pollution, *J. Appl. Meteorol.*, 43, 1038–1056.

Graf, H.-F., J. Yang, and T. M. Wagner (2009), Aerosol effects on clouds and precipitation during the 1997 smoke episode in Indonesia, *Atmos. Chem. Phys.*, *9*, 743-756, doi:10.5194/acp-9-743-2009.

Grell, G. A., S. E. Peckham, R. Schmitz, S. A. McKeen, G. Frost, W. C. Skamarock, and B. Eder (2005), Fully coupled ‘‘online’’ chemistry within the WRF model, *Atmos. Environ., 39*, 6957– 6975.

Grell, G., S. R. Freitas, M. Stuefer, and J. Fast (2011), Inclusion of biomass burning in WRF-Chem: Impact of wildfires on weather forecasts, *Atmos. Chem. Phys.*, *11*,

5829–5303, doi:10.5194/acp-11-5289-2010.

Gupta, S. K., D. P. Kratz, P. W. Stackhouse Jr., and A. C. Wilber (2001), The Langley parameterized shortwave algorithm (LPSA) for surface radiation budget studies, version 1.0, *Rep. NASA/TP-2001–211272*, 26 pp., NASA, Langley Research Center, Hampton, Va.

Gustafson, W. I., et al. (2007), Impact on modeled cloud characteristics due to simplified treatment of uniform cloud condensation nuclei during NEAQS 2004, *Geophys. Res. Lett.*, 34, L19809, doi:10.1029/2007GL030021.

Hobbs, P. V., and L. F. Radke (1969), Cloud condensation nuclei from a simulated forest fire, *Science, 163*, 279– 280.

Hobbs, P. V. (1978), Organization and structure of clouds and precipitation on the mesoscale and microscale in cyclonic storms, *Rev. Geophys.*, 16, 741–755.

Hobbs, P. V., J. S. Reid, R. A. Kotchenruther, R. J. Ferek, R. Weiss (1997), Direct radiative forcing by smoke from biomass burning, *Science*,275, 1776–1778.

Hoose, C., and O. Möhler (2012), Heterogeneous ice nucleation on atmospheric aerosols: a review of results from laboratory experiments, *Atmos. Chem. Phys*., *12*, 9817–9854, doi:10.5194/acp-12-9817-2012.

Ichoku, C., and Y. J. Kaufman (2005), A method to derive smoke emission rates from MODIS fire radiative energy measurements. *IEEE Trans. Geosci. Remote Sens.*, 43(11), 2636−2649.

Ichoku, C., R. Kahn, and M. Chin (2012), Satellite contributions to the quantitative characterization of biomass burning for climate modeling, *Atmos. Res., 111*, 1-28, doi:10.1016/j.atmosres.2012.03.007.

Igel, A. L., S. C. van den Heever, C. M. Naud, S. M. Saleeby, and D. J. Posselt (2013), Sensitivity of warm-frontal processes to cloud-nucleating aerosol concentrations, *J. Atmos. Sci.*, 70(6), 1768–1783.

IPCC (2013), *Climate Change 2013: The Physical Science Basis. Contribution of Working Group I to the Fifth Assessment Report of the Intergovernmental Panel on Climate Change*, 1535 pp., Cambridge University Press, Cambridge, United Kingdom and New York, NY, USA.

Jankov, I., W. A. Gallus, M. Segal, B. Shaw, and S. E. Koch (2005), The Impact of Different WRF Model Physical Parameterizations and Their Interactions on Warm Season MCS Rainfall, *Wea. Forecasting.*, *20*, 1048–1060.

Kahn, R. A., Y. Chen, D. L. Nelson, F.-Y. Leung, Q. Li, D. J. Diner, and J. A. Logan (2008), Wildfire smoke injection heights: Two perspectives from space, *Geophys. Res. Lett*., 35, L04809, doi:10.1029/2007GL032165.

Kaiser, J. W., et al. (2012), Biomass burning emissions estimated with a global fire assimilation system based on observations of fire radiative power, *Biogeosciences*, 9, 527–554, doi:10.5194/bg-9-527-2012.

Kaufman, Y. J., C. O. Justice, L. P. Flynn, J. D. Kendall, E. M. Prins, L. Giglio, D. E. Ward, W. P. Menzel, and A. W. Setzer (1998), Potential global fire monitoring from EOS-MODIS, *J. Geophys. Res.*, 103(D24), 32,215–32,238, doi:10.1029/98JD01644.

Khain, A., D. Roseenfeld, and A. Pokrovsky (2005), Aerosol impact on the dynamics and microphysics of deep convective clouds, *Q. J. R. Meteorol. Soc.*, 131, 2639–2663, doi:10.1256/qj.04.62.

Khain, A., N. BenMoshe, and A. Pokrovsky (2008), Factors determining the impact of aerosols on surface precipitation from clouds: An attempt at classification, *J. Atmos. Sci.*, 65, 1721–1748, doi:10.1175/2007JAS2515.1.

Khvorostyanov, V. I., and J. A. Curry (2004), The theory of ice nucleation by heterogeneous freezing of deliquescent mixed CCN. part I: Critical radius, energy, and nucleation rate, *J. Atmos. Sci*., 61(22), 2676– 2691.

Kloster, S., N. M. Mahowald, J. T. Randerson, P. E. Thornton, F. M. Hoffman, S. Levis, P. J. Lawrence, J. J. Feddema, K. W. Oleson, and D. M. Lawrence (2010), Fire dynamics during the 20th century simulated by the Community Land Model, *Biogeosciences Discuss*., 7, 565–630, doi:10.5194/bgd-7-565-2010.

Kondo, Y., et al. (2011), Emissions of black carbon, organic, and inorganic aerosols from biomass burning in North America and Asia in 2008, *J. Geophys. Res.*, *116*, D08204, doi:10.1029/2010JD015152.

Koren, I., Y. J. Kaufman, L. A. Remer, and J. V. Martins (2004), Measurement of the effect of Amazon smoke on inhibition of cloud formation, *Science*, *303*, 1342–1344, 10.1126/science.1089424.

Lance, S., et al. (2011), Cloud condensation nuclei as a modulator of ice processes in Arctic mixed-phase clouds, *Atmos. Chem. Phys.*, 11(15), 8003–8015, doi:10.5194/acp-11-8003-2011.

Langenfelds, R. L., R. J. Francey, B. C. Pak, L. P. Steele, J. Lloyd, C. M. Trudinger, and C. E. Allison (2002), Interannual growth rate variations of atmospheric CO_2 and its ^{13}C, H_2, CH_4, and CO between 1992 and 1999 linked to biomass burning, *Global Biogeochem. Cycles*, 16(3), 1048, doi:10.1029/2001GB001466.

Langmann, B. (2007), A model study of smoke-haze influence on clouds and warm precipitation formation in Indonesia 1997/1998, *Atmos. Environ.*, *41*, doi:10.1016/j.atmosenv.2007.04.050.

Langmann, B., B. Duncan, C. Textor, J. Trentmannd, and G. R. van der Werf (2009), Vegetation fire emissions and their impact on air pollution and climate, *Atmos. Environ.*, 43, 107–116, doi:10.1016/j.atmosenv.2008.09.047.

Lathem, T. L., et al. (2013), Analysis of CCN activity of Arctic aerosol and Canadian biomass burning during summer 2008, *Atmos. Chem. Phys.*, *13*, 2735–2756, doi:10.5194/acp-13-2735-2013.

Lee, S. S. (2011), Dependence of aerosol-precipitation interactions on humidity in a multiple-cloud system, *Atmos. Chem. Phys.*, 11,2179–2196, doi:10.5194/acp-11-2179-2011.

Levin, Z., and W. Cotton (Eds.) (2008), *Aerosol Pollution Impact on Precipitation: A Scientific Review*, Springer, New York.

Liu, S. C., et al. (1996), Model study of tropospheric trace species distributions during PEM-West A, *J. Geophys. Res.*, *101*(D1), 2073–2085, doi:10.1029/95JD02277.

Lohmann, U. (2002), A glaciation indirect effect caused by soot aerosols. *Geophys. Res. Lett.*, *29*(4), 1052, doi:10.1029/2001GL014357.

Lohmann, U., and J. Feichter (2005), Global indirect aerosol effects: A review, *Atmos. Chem. Phys.*, 5, 715–737.

Lohmann, U., and K. Diehl (2006), Sensitivity studies of the importance of dust ice nuclei for the indirect aerosol effect on stratiform mixed-phase clouds, *J. Atmos. Sci*., 63(3), 968–982.

Lu, Z., and I.N. Sokolik (2013a), Examining the cloud buffering under smoke-laden conditions: A case study of the 2002 Yakutsk wildfire season. In: Nucleation and Atmospheric Aerosols. DeMott, P. (Ed.), American Institute of Physics.

Lu, Z., and I.N. Sokolik (2013b), The effect of smoke emission amount on changes in cloud properties and precipitation: A case study of Canadian boreal wildfires of 2007, J. *Geophys. Res. Atmos*., 118, doi:10.1002/2013JD019860.

Lucht, W., I. C. Prentice, R. B. Myneni, S. Sitch, P. Friedlingstein, W. Cramer, P. Bousquet, W. Buermann, and B. Smith (2002), Climatic control of the high-latitude vegetation greening trend and Pinatubo effect, *Science*, 296(5573), 1687–1689.

Nam, C., S. Bony, J.-L. Dufresne, and H. Chepfer (2012), The 'too few, too bright' tropical low-cloud problem in CMIP5 models, *Geophys. Res. Lett.*, 39, L21801, doi:10.1029/2012GL053421.

Nelson, D., C. Lawshe, D. Mazzoni, D. Diner, and R. Kahn (2008), MISR plume height climatology project: Quality statement and error and bias analysis, report, Jet Propulsion Lab., NASA, La Cañada Flintridge, Calif. [Available at http://www-misr.jpl.nasa.gov/getData/accessData/MisrMinxPlumes/qualityStatement/.]

Martins, J. A., M. A. F. Silva Dias, and F. L. T. Gonçalves (2009), Impact of biomass burning aerosols on precipitation in the Amazon: A modeling case study, *J. Geophys. Res*., *114*, D02207, doi:10.1029/2007JD009587.

McKenzie, D., C. L. Raymond, L.-K. B. Kellogg, R. A. Norheim, A. G. Andreu, A. C. Bayard, K. E. Kopper, and E. Elman (2007), Mapping fuels at multiple scales: landscape application of the Fuel Characteristic Classification System, Can. J. Forest Res., 37, 2421–2437, doi:10.1139/X07-056.

Meyers, M. P., P. J. DeMott, and W. R. Cotton (1992), New primary ice nucleation parameterization in an explicit model. *J. Appl. Meteor*., *31*, 708–721.

Moorthi, S., H.-L. Pan, and P. Caplan (2001), Changes to the 2001 NCEP operational MRF/AVN Global Analysis/Forecast System, *Tech. Procedures Bull*., *484*, 14

pp., [Available online at http://www.nws.noaa.gov/om/tpb/484.htm].

Morrison, H., J.A. Curry and V.I. Khvorostyanov (2005), A new double-moment microphysics scheme for application in cloud and climate models. Part I: Description, *J. Atmos. Sci.*, *62*, 1665-1677.

Morrison, H., J. O. Pinto, J. A. Curry, and G. M. McFarquhar (2008), Sensitivity of arctic mixed-phase stratocumulus to cloud condensation and ice nuclei over regionally varying surface conditions, *J. Geophys. Res.*, *113*, D05203, doi:10.1029/2007JD008729.

Myhre G, et al. (2013), Radiative forcing of the direct aerosol effect from AeroCom Phase II simulations, *Atmos. Chem. Phys.* 13: 1853–1877.

Nash, C. H. and E. A. Johnson (1996), Synoptic climate of lightning caused forest fires in the subalpine and boreal forests, *Can. J. For. Res*. 26, 1859–1874.

O'Neill, N. T., et al. (2006), Evaluation of the GEM–AQ air quality model during the Québec smoke event of 2002: Analysis of extensive and intensive optical disparities, *Atmos. Environ*., *40*(20), 3737–3749, doi:10.1016/j.atmosenv.2006.03.006.

Péré, J. C., et al. (2014), Direct radiative effect of the Russian wildfires and its impact on air temperature and atmospheric dynamics during August 2010, *Atmos. Chem. Phys*., 14, 1999-2013, doi:10.5194/acp-14-1999-2014.

Petrenko, M., R. Kahn, M. Chin, A. Soja, T. Kucsera, and Harshvardhan (2012), The use of satellite-measured aerosol optical depth to constrain biomass burning emissions source strength in the global model GOCART, *J. Geophys. Res.*, *117*, D18212, doi:10.1029/2012JD017870.

Petters, M. D., C. M. Carrico, S. M. Kreidenweis, A. J. Prenni, P. J. DeMott, J. L. Collett Jr., and H. Moosmüller (2009a), Cloud condensation nucleation activity of biomass burning aerosol, *J. Geophys. Res.*, 114, D22205, doi:10.1029/2009JD012353.

Petters, M. D., et al. (2009b), Ice nuclei emissions from biomass burning, *J. Geophys. Res*., 114, D07209, doi:10.1029/2008JD011532.

Pfister, G. G., P. G. Hess, L. K. Emmons, P. J. Rasch, and F. M. Vitt (2008), Impact of the summer 2004 Alaska fires on top of the atmosphere clear-sky radiation fluxes, *J. Geophys. Res.*, 113, D02204, doi:10.1029/2007JD008797.

Phillips, V. T. J., P. J. DeMott, and C. Andronache (2008), An empirical parameterization of heterogeneous ice nucleation for multiple chemical species of aerosol, *J. Atmos. Sci.*, 65(9), 2757–2783.

Pinker, R. T., and I. Laszlo (1992), Modelling surface solar irradiance for satellite applications on a global scale, *J. Appl. Meteorol.*, 31,194–211, doi:10.1175/1520-0450(1992)031<0194:MSSIFS>2.0.CO;2.

Pratt, K. A., et al. (2011), Flight-based chemical characterization of biomass burning aerosols within two prescribed burn smoke plumes, *Atmos. Chem. Phys*., *11*, 12,549–12,565, doi:10.5194/acp-11-12549-2011.

Prenni, A. J., P. J. DeMott, A. P. Sullivan, R. C. Sullivan, S. M. Kreidenweis, and D. C. Rogers (2012), Biomass burning as a potential source for atmospheric ice nuclei: Western wildfires and prescribed burns, *Geophys. Res. Lett*., 39, L11805, doi:10.1029/2012GL051915.

Prins, E. M., and W. P. Menzel (1992), Geostationary satellite detection of biomass burning in South America, *Int. J. Remote Sens.*, 13, 2783– 2799.

Prins, E. M., J. M. Felts, W. P. Menzel, and D. E. Ward (1998), An overview of GOES-8 diurnal fire and smoke results for SCAR-B and 1995 fire season in South America, *J. Geophys. Res*., *103*, 31,821–31,835.

Pruppacher, H. R., and J. D. Klett (1997), Microphysics of Clouds and Precipitation, 954 pp., Kluwer Academic Publishers, Dordrecht, The Netherlands.

Randerson, J. T., et al. (2006), The impact of boreal forest fire on climate warming, *Science*, *314*, 130– 132.

Randerson, J. T., Y. Chen, G. R. van der Werf, B. M. Rogers, and D. C. Morton (2012), Global burned area and biomass burning emissions from small fires, *J. Geophys. Res*., 117, G04012, doi:10.1029/2012JG002128.

Reid, J. S., P. V. Hobbs, R. J. Ferek, D. R. Blake, J. V. Martins, M. R. Dunlap, and C. Liousse (1998), Physical, chemical and optical properties of regional hazes

dominated by smoke in Brazil, *J. Geophys. Res*., *103*, 32,059– 32,080.

Reid, J. S., R. Koppmann, T. F. Eck, and D. P. Eleuterio (2005), A review of biomass burning emissions part II: Intensive physical properties of biomass burning particles, *Atmos. Chem. Phys.*, *5*, 799– 825.

Reid, J. S., et al. (2009), Global monitoring and forecasting of biomass burning smoke: Description of and lessons from the Fire Locating and Modeling of Burning Emissions (Flambe) program, *IEEE J Selected Topics Appl. Earth Observ. Remote Sens.*, *2*(3), 144–162.

Reid, J. S., et al. (2013), Observing and understanding the Southeast Asian aerosol system by remote sensing: An initial review and analysis for the Seven Southeast Asian Studies (7SEAS) program, *Atmos. Res.*, 122, 403–468, doi:10.1016/j.atmosres.2012.06.005.

Reisner, J., R. M. Rasmussen, and R. T. Bruintjes (1998), Explicit forecasting of supercooled liquid water in winter storms using the MM5 mesoscale model. *Q. J. Roy. Meteor. Soc*., *124*, 1071–1107.

Roberts, G., M. Wooster, P. H. Freeborn, and W. Xu (2011), Integration of geostationary FRP and polar-orbiter burned area datasets for an enhanced biomass burning inventory, *Remote Sens. Environ.*, 115(8), 2047–2061, doi:10.1016/j.rse.2011.04.006.

Rosenfeld, D. (1999), TRMM observed first direct evidence of smoke from forest fires inhibiting rainfall, *Geophys. Res. Lett.*, *26*, 3105–3108, doi:10.1029/1999GL006066.

Rosenfeld, D., U. Lohmann, G. B. Raga, C. D. O'Dowd, M. Kulmala, S. Fuzzi, A. Reissell, and M. O. Andreae (2008), Flood or drought: How do aerosols affect precipitation? *Science*, 321, 1309–1313, doi:10.1126/science.1160606.

Roy D.P., Y. Jin, P.E. Lewis, C.O. Justice (2005), Prototyping a global algorithm for systematic fire-affected area mapping using MODIS time series data. *Remote Sensing of Environment*, 97, 137–162.

Saleeby, S. M., W. R. Cotton, D. Lowenthal, R. D. Borys, and M. A. Wetzel (2009), Influence of cloud condensation nuclei on orographic snowfall, *J. Appl. Meteorol. Clim.*, *48*, 694–703, doi:10.1175/2008JAMC1989.1.

Sassen, K., and V. I. Khvorostyanov (2008), Cloud effects from boreal forest fire smoke: Evidence for ice nucleation from polarization lidar data and cloud model simulations, *Environ. Res. Lett.*, *3*(2), 025006,doi:10.1088/1748-9326/3/2/025006.

Seifert, A., and K. D. Beheng (2006), A two-moment cloud microphysics parameterization for mixed-phase clouds: Part 2. Maritime vs. continental deep convective storms, *Meteorol. Atmos. Phys.*, 92, 67–82, doi:10.1007/s00703-005-0113-3.

Seifert, A., C. Köhler, and K. D. Beheng (2012), Aerosol-cloud-precipitation effects over germany as simulated by a convective-scale numerical weather prediction model, *Atmos. Chem. Phys.*, 12(2), 709–725, doi:10.5194/acp-12-709-2012.

Seiler, W., and P. J. Crutzen (1980), Estimates of gross and net fluxes of carbon between the biosphere and the atmosphere from biomass burning, *Clim. Change*, 2, 207–247.

Sessions, W. R., H. E. Fuelberg, R. A. Kahn, and D. M. Winker (2011), An investigation of methods for injecting emissions from boreal wildfires using WRF-Chem during ARCTAS, *Atmos. Chem. Phys.*, *11*, 5719-5744, doi:10.5194/acp-11-5719-2011.

Soja, A. J., N. M. Tchebakova, N. H. F. French, M. D. Flannigan, H. H. Shugart, B. J. Stocks, A. I. Sukhinin, E. I. Parfenova, F. S. Chapin III, and P. W. Stackhouse Jr. (2007), Climate-induced boreal forest change: Predictions versus current observations, *Global Planet. Change*, 56, 274–296.

Soja, A. J., et al. (2009), Assessing satellite-based fire data for use in the National Emissions Inventory, *J. Appl. Remote Sens.*, 3, 031504, doi:10.1117/1.3148859.

Stevens, B., and G. Feingold (2009), Untangling aerosol effects on clouds and precipitation in a buffered system, *Nature*, 461, 607–613, doi:10.1038/nature08281.

Stocks, B. J., et al. (1998), Climate change and forest fire potential in Russian and Canadian boreal forests, *Clim. Change*, *38*, 1–13, doi:10.1023/A:1005306001055.

Stone, R. S., G. P. Anderson, E. P. Shettle, E. Andrews, K. Loukachine, E. G. Dutton, C. Schaaf, and M. O. Roman III (2008), Radiative impact of boreal smoke in the

Arctic: Observed and modeled, *J. Geophys. Res.*, 113, D14S16, doi:10.1029/2007JD009657.

Taylor, K. E. (2001), Summarizing multiple aspects of model performance in a single diagram, *J. Geophys. Res.*, 106, 7183–7192.

Ten Hoeve, J. E., M. Z. Jacobson, and L. A. Remer (2012), Comparing results from a physical model with satellite and in situ observations to determine whether biomass burning aerosols over the Amazon brighten or burn off clouds, *J. Geophys. Res*., 117, D08203, doi:10.1029/2011JD016856.

Thompson, G., R. M. Rasmussen, and K. Manning (2004), Explicit forecasts of winter precipitation using an improved bulk microphysics scheme. Part I: Description and sensitivity analysis, *Mon. Weather Rev*.,*132*, 519– 542.

Tosca, M. G., J. T. Randerson, C. S. Zender, M. G. Flanner, and P. J. Rasch (2010), Do biomass burning aerosols intensify drought in equatorial Asia during El Niño?, *Atmos. Chem. Phys*., *10*, 3515–3528, doi:10.5194/acp-952-3515-2010.

Tosca, M. G., J. T., Randerson, and C. S. Zender (2013), Global impact of smoke aerosols from landscape fires on climate and the Hadley circulation, *Atmos. Chem. Phys*., 13, 5227-5241, doi:10.5194/acp-13-5227-2013.

Twomey, S. (1974), Pollution and the planetary albedo, *Atmos. Environ.*, 8, 1251–1256.

Val Martin, M., R. A. Kahn, J. A. Logan, R. Paugam, M. Wooster, and C. Ichoku (2012), Space-based observational constraints for 1-D fire smoke plume-rise models, *J. Geophys. Res*., 117, D22204, doi:10.1029/2012JD018370.

van den Heever, S. C., G. Carrio, W. R. Cotton, P. J. DeMott, and A. J. Prenni (2006), Impacts of nucleating aerosol on Florida convection: Part I. Mesoscale simulations, *J. Atmos. Sci.*, 63, 1752–1775, doi:10.1175/JAS3713.1.

van den Heever, S. C., and W. R. Cotton (2007), Urban aerosol impacts on downwind convective storms, *J. Appl. Meteorol. Climatol.*, 46,828–850, doi:10.1175/JAM2492.1.

van den Heever, S. C., G. L. Stephens, and N. B. Wood (2011), Aerosol indirect effects on tropical convection characteristics under conditions of radiative-convective equilibrium, *J. Atmos. Sci.*, 68, 699–718, doi:10.1175/2010JAS3603.1.

van der Werf, G. R., et al. (2010), Global fire emissions and the contribution of deforestation, savanna, forest, agricultural, and peat fires (1997–2009), *Atmos. Chem. Phys*., *10*, 11,707–11,735, doi:10.5194/acp-10-11707-2010.

Verlinde, J., et al. (2007), The mixed-phase Arctic cloud experiment. *Bull. Am. Meteorol. Soc.* 88, 205–221.

Wang, J., S. A. Christopher, U. S. Nair, J. S. Reid, E. M. Prins, J. Szykman, and J. L. Hand (2006), Mesoscale modeling of Central American smoke transport to the United States: 1. "Top-down" assessment of emission strength and diurnal variation impacts, *J. Geophys. Res.*, *111*, D05S17, doi:10.1029/2005JD006416.

Wiedinmyer, C., S. K. Akagi, R. J. Yokelson, L. K. Emmons, J. A. Al-Saadi, J. J. Orlando, and A. J. Soja (2011), The Fire INventory from NCAR (FINN): A high resolution global model to estimate the emissions from open burning, *Geosci. Model Dev*., *4*, 625–641, doi:10.5194/gmd-4-625-2011.

Wu, L., H. Su, and J. H. Jiang (2011), Regional simulations of deep convection and biomass burning over South America: 2. Biomass burning aerosol effects on clouds and precipitation, *J. Geophys. Res*., *116*, D17209, doi:10.1029/2011JD016106.

Xu, L., et al. (2013), Temperature and vegetation seasonality diminishment over northern lands, *Nature CC*, 3, 581–586.

Yang, Q., W. I. Gustafson Jr., J. D. Fast, H. Wang, R. C. Easter Jr., H.Morrison, Y. N. Lee, E. G. Chapman, S. N. Spak, and M. A. Mena-Carrasco (2011), Assessing regional scale predictions of aerosols, marine stratocumulus, and their interactions during VOCALS-REx using WRFChem, *Atmos. Chem. Phys*., *11*, 11,951_11,975, doi:10.5194/acp-11-11951-2011.

Zaveri, R. A., R. C. Easter, J. D. Fast, and L. K. Peters (2008), Model for Simulating Aerosol Interactions and Chemistry (MOSAIC), *J. Geophys. Res*., *113*, D13204, doi:10.1029/2007JD008782.

Zhang, X., S. Kondragunta, and B. Quayle (2011), Estimation of biomass burned areas using multiple-satellite-observed active fires, *IEEE Trans. Geosci. Remote Sens.*, 49, 4469–4482, doi:10.1109/TGRS.2011.2149535.

VITA

Zheng Lu was born in 1985 in Chifeng, Nei Mongol, China. He receive a B.S. in Atmospheric Science from Nanjing University, China in 2007. His enthusiasm for research in atmospheric science led to his pursuing a Ph.D in the School of Earth and Atmospheric Sciences at the Georgia Institute of Technology in Atlanta, GA in 2007.